

## Supporting Information

### Determining the Key Vibrations for Spin Relaxation in Ruffled Cu(II) Porphyrins via Resonance Raman Spectroscopy

Nathanael P. Kazmierczak, Nathan E. Lopez, Kaitlin M. Luedecke, and Ryan G. Hadt\*

Division of Chemistry and Chemical Engineering, Arthur Amos Noyes Laboratory of Chemical Physics, California Institute of Technology, Pasadena, California 91125, United States

\*Corresponding author: rghadt@caltech.edu

## Table of Contents

<b>1. General Considerations</b> .....	3
<b>A. Materials and Synthesis</b> .....	3
<b>i. Free Base Porphyrin</b> .....	3
<b>ii. Metalated Porphyrins</b> .....	3
<b>B. Solid State Dilutions for EPR Analysis</b> .....	4
<b>i. 1% CuOEP in ZnOEP</b> .....	4
<b>ii. 1% CuTPP in NiTPP</b> .....	4
<b>iii. 1% CuTiPP in NiTiPP</b> .....	4
<b>iv. 0.1% CuOEP in ZnOEP</b> .....	5
<b>v. 0.1% CuTPP in NiTPP</b> .....	5
<b>2. Experimental Methods</b> .....	5
<b>A. Ultraviolet-Visible Absorption Spectroscopy</b> .....	5
<b>B. Powder X-Ray Diffraction</b> .....	10
<b>C. Single Crystal X-Ray Structure Determination</b> .....	16
<b>D. Resonance Raman Spectroscopy</b> .....	18
<b>E. Continuous Wave Electron Paramagnetic Resonance Spectroscopy</b> .....	22
<b>F. Pulse Electron Paramagnetic Resonance Spectroscopy</b> .....	25
<b>3. Computational Methods</b> .....	35
<b>A. Computational Parameters</b> .....	35
<b>B. Spin-Phonon Coupling</b> .....	35
<b>C. Raman Spectra Calculations</b> .....	51

<b>D. Analysis of Excited State Transition Energies .....</b>	<b>69</b>
<b>E. Excited State Transition Energies and Principal g values of Idealized CuP .....</b>	<b>70</b>
<b>4. Supplemental Discussion .....</b>	<b>71</b>
<b>A. Quantification of Macrocycle Distortion.....</b>	<b>71</b>
<b>B. Implications of CuTiPP Crystal Phases for Distortion Quantification.....</b>	<b>71</b>
<b>C. Transformation of Vibrational Mode Symmetries from <math>D_{4h}</math> to <math>D_{2d}</math> .....</b>	<b>72</b>
<b>5. References.....</b>	<b>74</b>

## 1. General Considerations

### A. Materials and Synthesis

Air-free syntheses were conducted using Schlenk technique under dinitrogen atmosphere. Diethyl ether (Et<sub>2</sub>O), toluene, hexanes, and tetrahydrofuran (THF) were dried using a Pure Process Technology solvent purification system and stored over activated 3 Å molecular sieves for at least 1 night prior to use. Dichloromethane (CH<sub>2</sub>Cl<sub>2</sub>, Aldrich, ≥ 98%) was refluxed over calcium hydride at 40 °C for 2 hours and distilled prior to use. Copper(II) Octaethylporphine (CuOEP, Frontier Specialty Chemicals, > 95%), Zinc(II) Octaethylporphine (ZnOEP, Frontier Specialty Chemicals, >95%), 5, 10, 15, 20-Tetraphenyl-21H, 23H-porphine nickel(II) (NiTPP, Aldrich, ≥ 95%), 5, 10, 15, 20-Tetraphenyl-21H, 23H-porphine copper(II) (CuTPP, Aldrich), Pyrrole (Aldrich, 97%), Isobutyryl Aldehyde (Tokyo Chemical Institute, >98%), 2,3-dichloro-5,6-dicyano-1,4-benzoquinone (DDQ, Combi Blocks, 96%), Boron Trifluoride Diethyl Etherate (BF<sub>3</sub>•OEt<sub>2</sub>, Tokyo Chemical Institute, >98%), Nickel(II) Acetate hydrate (Ni(OAc)<sub>2</sub>•xH<sub>2</sub>O, Alfa Aesar, >99%), and Copper(II) Acetate monohydrate (Cu(OAc)<sub>2</sub>•H<sub>2</sub>O, Thermo Scientific, >99%), were used without further purification. For non-air-free syntheses/workups, the solvents used were either ACS or reagent grade. Grade III Alumina for column chromatography was prepared by adding 7% deionized water by weight to Brockman Grade I Neutral Aluminum Oxide (Aldrich). Alumina and silica gel (Alfa Aesar) were used for column chromatography.

#### i. Free Base Porphyrin

*5, 10, 15, 20-Tetraisopropylporphyrin (H<sub>2</sub>TiPP)*: H<sub>2</sub>TiPP was synthesized according to a literature procedure using modified Lindsey conditions.<sup>1,2</sup> Briefly, to a 2 L, two-neck round bottom equipped with a stir-bar, 1 L dry CH<sub>2</sub>Cl<sub>2</sub> was added along with isobutyryl aldehyde (150 mmol, 13.7 mL) and pyrrole (150 mmol, 10.5 mL). After degassing the solution for 30 mins with N<sub>2</sub>, boron trifluoride etherate (28 mmol, 3.5 mL) was added and the reaction flask was shielded from ambient light. After stirring for 14 hours, DDQ (110 mmol, 25 g) was added, and the solution refluxed for 2 hours. The solution was concentrated to 200 mL and three column chromatography experiments followed. First, the crude material was flushed through a neutral grade III alumina column with CH<sub>2</sub>Cl<sub>2</sub> as eluent, all the eluted material was collected. Next, the material was flushed through silica with 1:1 CH<sub>2</sub>Cl<sub>2</sub>/hexanes (v:v) as eluent, and all eluted material was collected. Finally, the material was flushed through another neutral grade III alumina column with CH<sub>2</sub>Cl<sub>2</sub> as eluent, and the deep purple band was isolated. After evaporating, a purple powder was yielded, and this was used in metalation experiments without further purification. λ nm (log ε): 420 (5.58), 522 (4.05), 559 (3.78), 602 (3.55), 658 (3.61).

#### ii. Metalated Porphyrins

*{5, 10, 15, 20-Tetraisopropylporphyrinato}nickel(II) (NiTiPP)*: Nickel insertion into the free base H<sub>2</sub>TiPP was accomplished following an established literature procedure using a modified acetate method.<sup>2,3</sup> Briefly, to a 500 mL, two-neck round bottom flask, H<sub>2</sub>TiPP (120 mg) was added along with 200 mL dry CH<sub>2</sub>Cl<sub>2</sub>. After degassing for 15 mins with N<sub>2</sub>, a saturated solution of nickel acetate in methanol was added and the reaction mixture was refluxed for 3 hours. The solution was concentrated to 75 mL, washed exhaustively with water (5x50 mL), and dried with magnesium sulfate. After filtering, the crude material was subjected to a neutral grade III alumina column with CH<sub>2</sub>Cl<sub>2</sub> as eluent. The desired product eluted as a single red band and was isolated by evaporation, yielding purple crystalline material.  $\lambda$  nm (log  $\epsilon$ ): 423 (5.33), 547 (4.19), 586 (3.52).

*{5, 10, 15, 20-Tetraisopropylporphyrinato}copper(II) (CuTiPP)*: Copper insertion into the free base H<sub>2</sub>TiPP was accomplished following an established literature procedure using a modified acetate method.<sup>2,3</sup> Briefly, to a 500 mL, two-neck round bottom flask, H<sub>2</sub>TiPP (120 mg) was added along with 200 mL dry CH<sub>2</sub>Cl<sub>2</sub>. After degassing for 15 mins with N<sub>2</sub>, a saturated solution of copper acetate in methanol was added and the reaction mixture refluxed for 3 hours. The solution was concentrated to 75 mL and washed exhaustively with water (5x50 mL) and dried with magnesium sulfate. After filtering, the crude material was subjected to a neutral grade III alumina column with CH<sub>2</sub>Cl<sub>2</sub> as eluent. The product eluted as a single red band and was isolated by evaporation, yielding purple crystals.  $\lambda$  nm (log  $\epsilon$ ): 420 (5.62), 554 (4.16), 591 (3.60).

## **B. Solid State Dilutions for EPR Analysis**

### **i. 1% CuOEP in ZnOEP**

To a 100 mL volumetric flask, ZnOEP (100 mg) was added and diluted with CH<sub>2</sub>Cl<sub>2</sub>. To a separate 25 mL volumetric flask, CuOEP (10 mg) was added and diluted with CH<sub>2</sub>Cl<sub>2</sub>. The solution of ZnOEP was transferred to a 250 mL round bottom flask and to this solution, 2.5 mL of the CuOEP solution was added. This mixture was briefly stirred and evaporated to yield a 1% CuOEP in ZnOEP sample by weight.

### **ii. 1% CuTPP in NiTPP**

To a 100 mL volumetric flask, NiTPP (100 mg) was added and diluted with CH<sub>2</sub>Cl<sub>2</sub>. To a separate 25 mL volumetric flask, CuTPP (10 mg) was added and diluted with CH<sub>2</sub>Cl<sub>2</sub>. The solution of NiTPP was transferred to a 250 mL round bottom flask and to this solution, 2.5 mL of the CuTPP solution was added. This mixture was briefly stirred and evaporated to yield a 1% CuTPP in NiTPP sample by weight.

### **iii. 1% CuTiPP in NiTiPP**

To a 100 mL volumetric flask, NiTiPP (50 mg) was added and diluted with CH<sub>2</sub>Cl<sub>2</sub>. To a separate 25 mL volumetric flask, CuTiPP (10 mg) was added and diluted with CH<sub>2</sub>Cl<sub>2</sub>. The solution of NiTiPP was transferred to a 250 mL round bottom flask and to this solution, 1.25 mL of the CuTiPP solution was added. This mixture was briefly stirred and evaporated to yield a 1% CuTiPP in NiTiPP sample by weight.

#### iv. 0.1% CuOEP in ZnOEP

A round bottom flask was charged with 50 mg ZnOEP and 0.05 mg CuOEP (diluted) in  $\text{CH}_2\text{Cl}_2$ . This mixture was briefly stirred and evaporated to yield a 0.1% CuOEP in ZnOEP sample by weight.

#### v. 0.1% CuTPP in NiTPP

A round bottom flask was charged with 100 mg NiTPP and 0.1 mg CuTPP (diluted) in  $\text{CH}_2\text{Cl}_2$ . This mixture was briefly stirred and evaporated to yield a 0.1% CuTPP in NiTPP sample by weight.

## 2. Experimental Methods

### A. Ultraviolet-Visible Absorption Spectroscopy

UV-vis-NIR absorption spectra were obtained on a Varian Cary 500 spectrophotometer using 6Q quartz 10mm path length cuvettes.

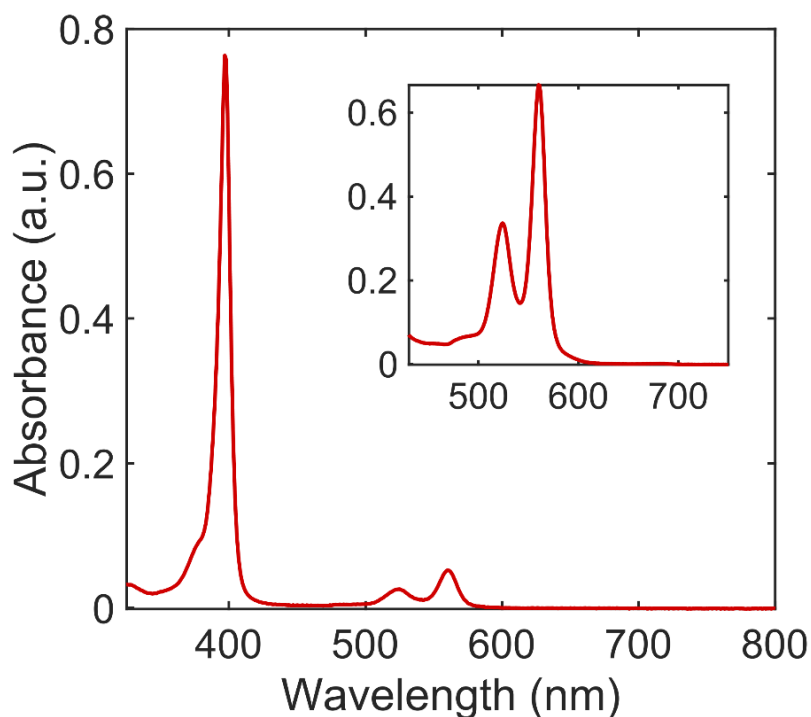


**Figure S1.** UV-vis spectrum of 1  $\mu\text{M}$  CuOEP in  $\text{CH}_2\text{Cl}_2$ . *Inset:* UV-vis of the Q-band region of 19  $\mu\text{M}$  CuOEP in  $\text{CH}_2\text{Cl}_2$ .  $\lambda$  ( $\lg \epsilon$ ): 397 (5.77), 525 (4.25), 560 (4.55).

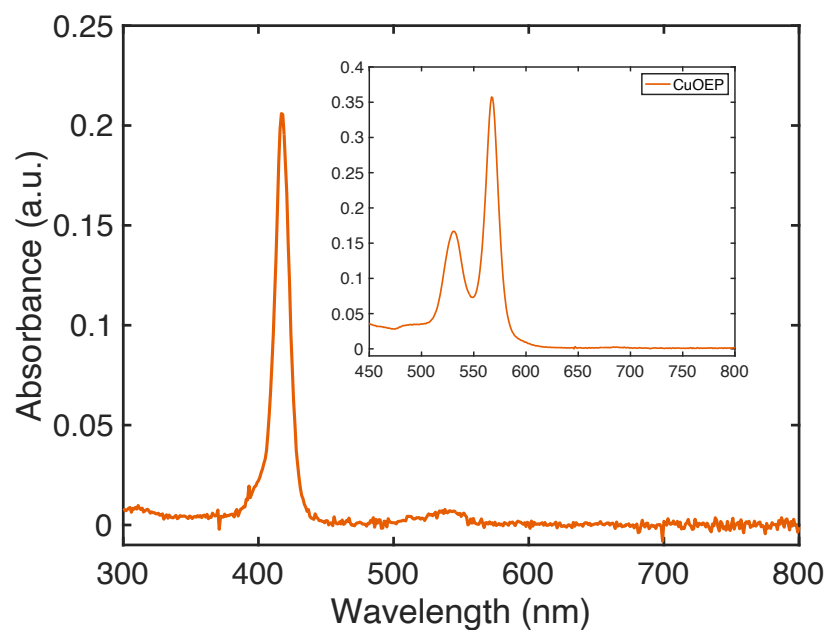


**Figure S2.** UV-vis spectrum of 1  $\mu\text{M}$  CuOEP in  $\text{CS}_2$ . *Inset:* UV-vis of the Q-band region of 11  $\mu\text{M}$  CuOEP in  $\text{CS}_2$ .

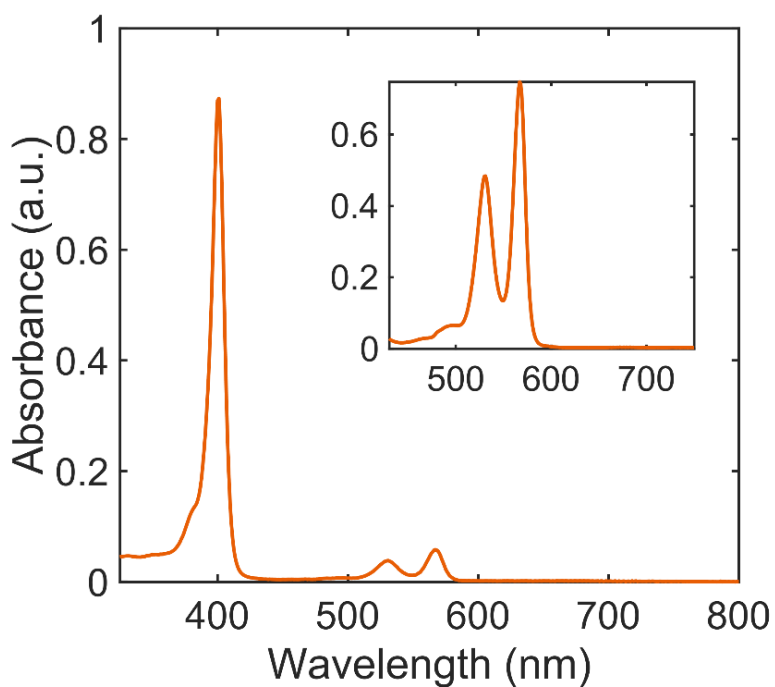


**Figure S3.** UV-vis spectrum of 1  $\mu\text{M}$  ZnOEP in  $\text{CH}_2\text{Cl}_2$ . *Inset:* UV-vis of the Q-band region of 18  $\mu\text{M}$  ZnOEP in  $\text{CH}_2\text{Cl}_2$ .  $\lambda$  ( $\lg \epsilon$ ): 401 (5.86), 530 (4.43), 567 (4.62).

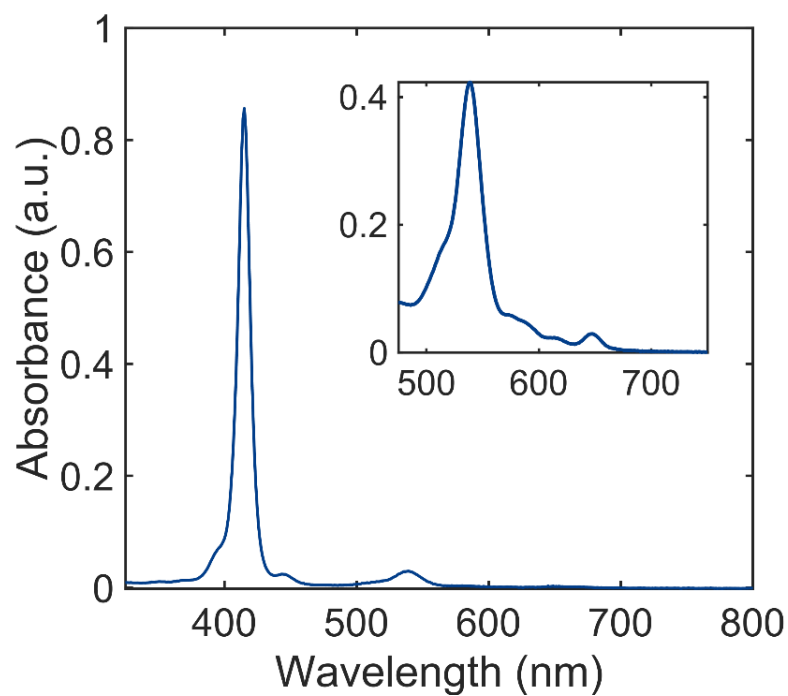


**Figure S4.** UV-vis spectrum of 1  $\mu\text{M}$  CuTPP in  $\text{CH}_2\text{Cl}_2$ . *Inset:* UV-vis of the Q-band region of 19  $\mu\text{M}$  CuTPP in  $\text{CH}_2\text{Cl}_2$ .  $\lambda$  ( $\lg \epsilon$ ): 415 (5.82), 538 (4.35), 647 (3.18).

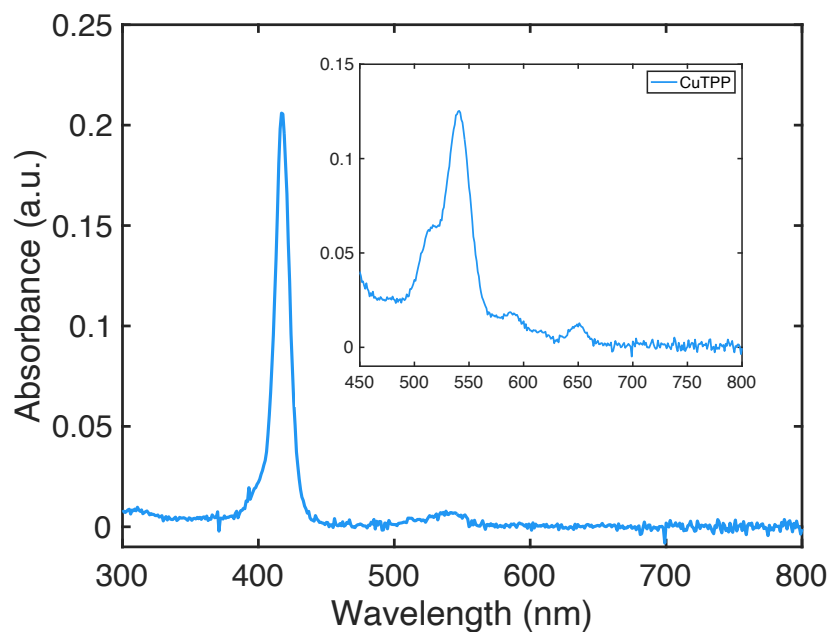


**Figure S5.** UV-vis spectrum of 1  $\mu\text{M}$  CuTPP in  $\text{C}_6\text{H}_6$ . *Inset:* UV-vis of the Q-band region of 11  $\mu\text{M}$  CuTPP in  $\text{C}_6\text{H}_6$ .

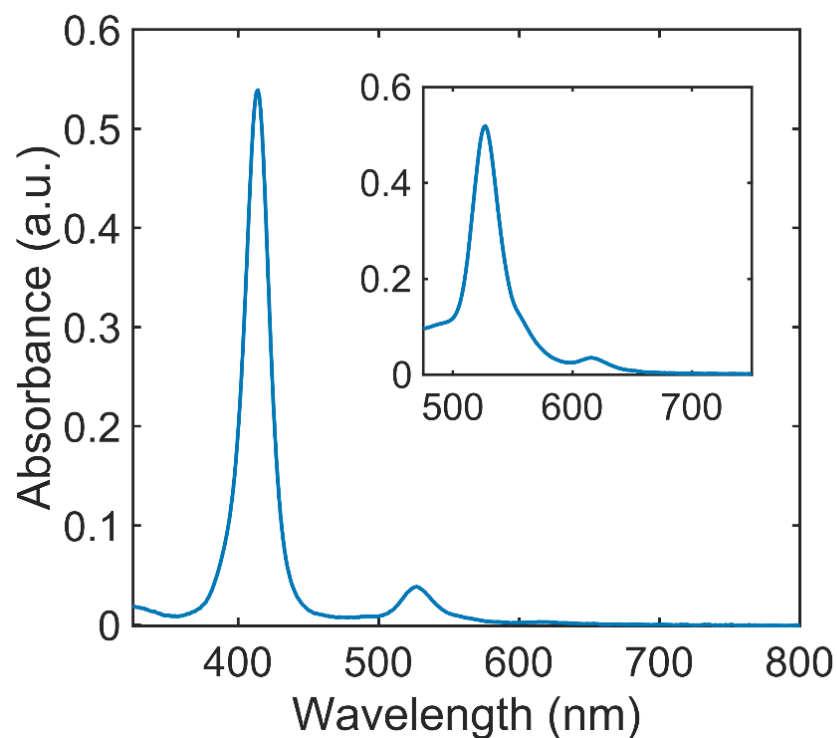


**Figure S6.** UV-vis spectrum of 1  $\mu\text{M}$  NiTPP in  $\text{CH}_2\text{Cl}_2$ . *Inset:* UV-vis of the Q-band region of 20  $\mu\text{M}$  NiTPP in  $\text{CH}_2\text{Cl}_2$ .  $\lambda$  ( $\lg \epsilon$ ): 413 (5.62), 526 (4.41), 617 (3.25).

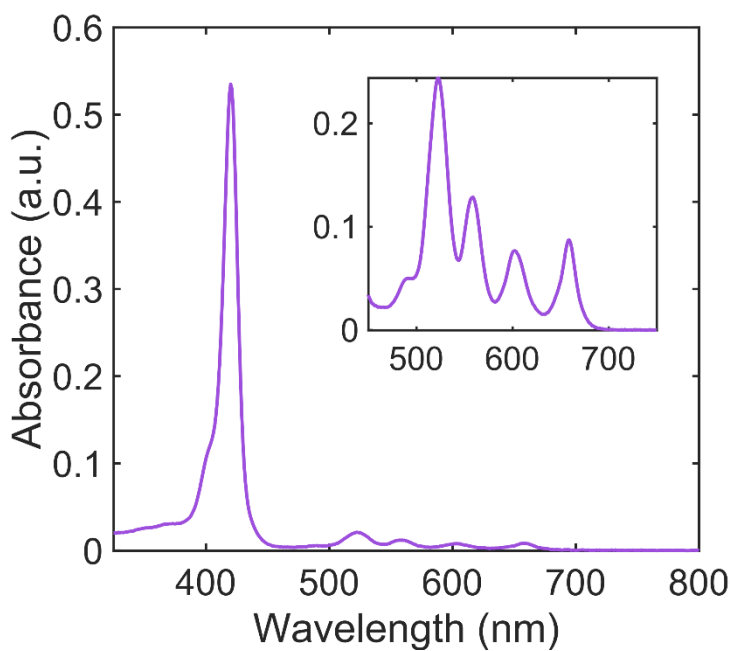


**Figure S7.** UV-vis spectrum of 1  $\mu\text{M}$   $\text{H}_2\text{TiPP}$  in  $\text{CH}_2\text{Cl}_2$ . *Inset:* UV-vis of the Q-band region of 22  $\mu\text{M}$   $\text{H}_2\text{TiPP}$  in  $\text{CH}_2\text{Cl}_2$ .  $\lambda$  ( $\lg \epsilon$ ): 420 (5.58), 522 (4.05), 559 (3.78), 602 (3.55), 658 (3.61).

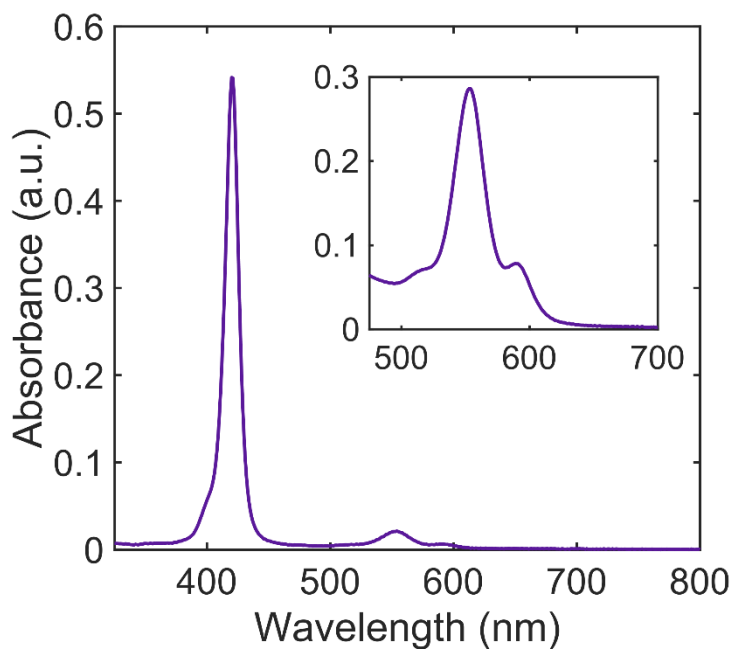


**Figure S8.** UV-vis spectrum of 1  $\mu\text{M}$  CuTiPP in  $\text{CH}_2\text{Cl}_2$ . *Inset:* UV-vis of the Q-band region of 20  $\mu\text{M}$  CuTiPP in  $\text{CH}_2\text{Cl}_2$ .  $\lambda$  ( $\lg \epsilon$ ): 420 (5.62), 554 (4.16), 591 (3.60).

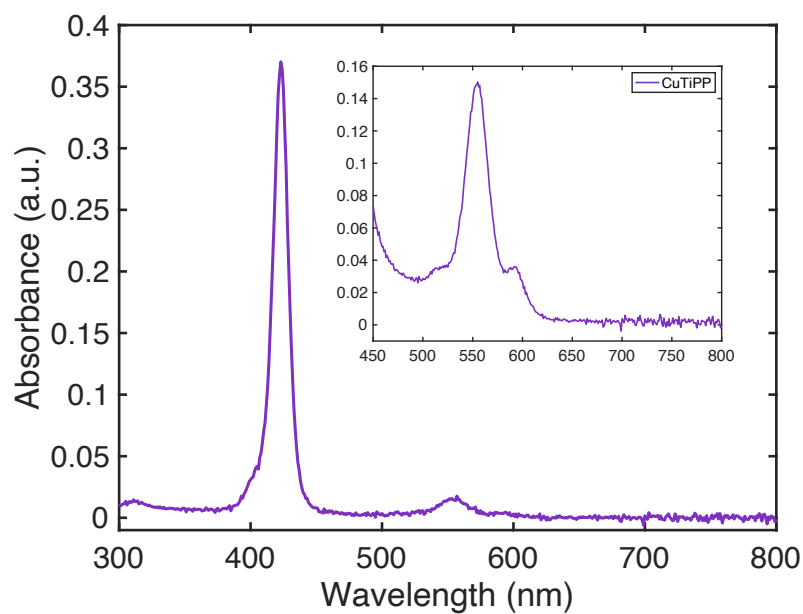


**Figure S9.** UV-vis spectrum of 1  $\mu\text{M}$  CuTiPP in  $\text{C}_6\text{H}_6$ . *Inset:* UV-vis of the Q-band region of 11  $\mu\text{M}$  CuTiPP in  $\text{C}_6\text{H}_6$ .

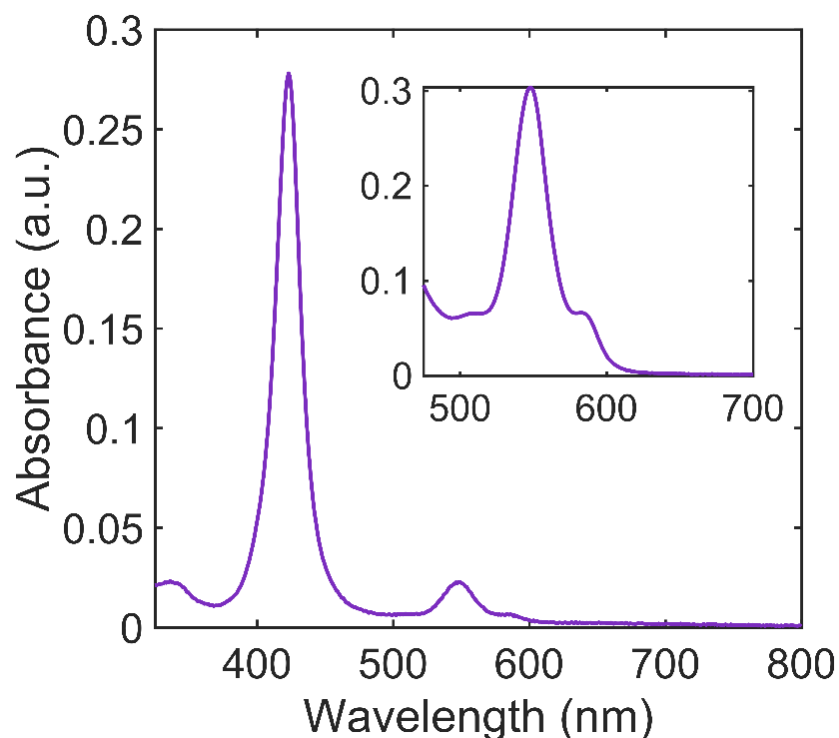


**Figure S10.** UV-vis spectrum of 1  $\mu\text{M}$  NiTiPP in  $\text{CH}_2\text{Cl}_2$  for main spectrum. *Inset:* UV-vis of the Q-band region of 20  $\mu\text{M}$  NiTiPP in  $\text{CH}_2\text{Cl}_2$ .  $\lambda$  ( $\lg \epsilon$ ): 423 (5.33), 547 (4.19), 586 (3.52).

## B. Powder X-Ray Diffraction

Lab powder X-ray diffraction (PXRD) was collected on samples in air using a Rigaku SmartLab diffractometer. The diffraction patterns were fit with the Rietveld method using the General Structure Analysis System II (GSAS-II),<sup>4,5</sup> and visualization of the crystal structures was aided by VESTA.<sup>6</sup> Line broadening was accounted for by domain size, and orientation selection was accounted for by spherical harmonic preferred orientation model. Sample displacement was used to account for spectrum shifts.

Neat powders of CuTPP,<sup>7</sup> NiTPP,<sup>8</sup> CuOEP,<sup>9</sup> ZnOEP,<sup>10</sup> and NiTiPP<sup>11</sup> refined well to the corresponding literature crystal structures indicated in the above references. EPR dilutions of 1:100 CuTPP:NiTPP, 1:100 CuOEP:ZnOEP, and 1:100 CuTiPP:NiTiPP likewise each refined well to the pure diamagnetic host crystal structures (NiTPP, ZnOEP, and NiTiPP, respectively). However, the PXRD for CuTiPP as synthesized did not refine to the pure literature crystal structure<sup>2</sup> (space group  $Fdd2$ ). Therefore, we acquired single-crystal XRD of the as-synthesized CuTiPP (see **Supporting Information Section 2C, Figure S20**). The refined structure revealed a previously unreported solvate phase of CuTiPP, containing two porphyrin molecules and one dichloromethane molecule in the unit cell (space group  $I4_1$ ). The CuTiPP PXRD could then be fit very well to a combination of both the unsolvated  $Fdd2$  structure and the solvated  $I4_1$  structure (**Figure S17**). Note that  $\text{CH}_2\text{Cl}_2$  was used as a recrystallization solvent in this work instead of the  $\text{CHCl}_3$  previously reported.<sup>2</sup> It appears likely that this solvent change is responsible for accessing the new phase. For a discussion of the implications of these crystal phases for the molecular geometry probed in the EPR experiments, see **Supporting Information Section 4B**.

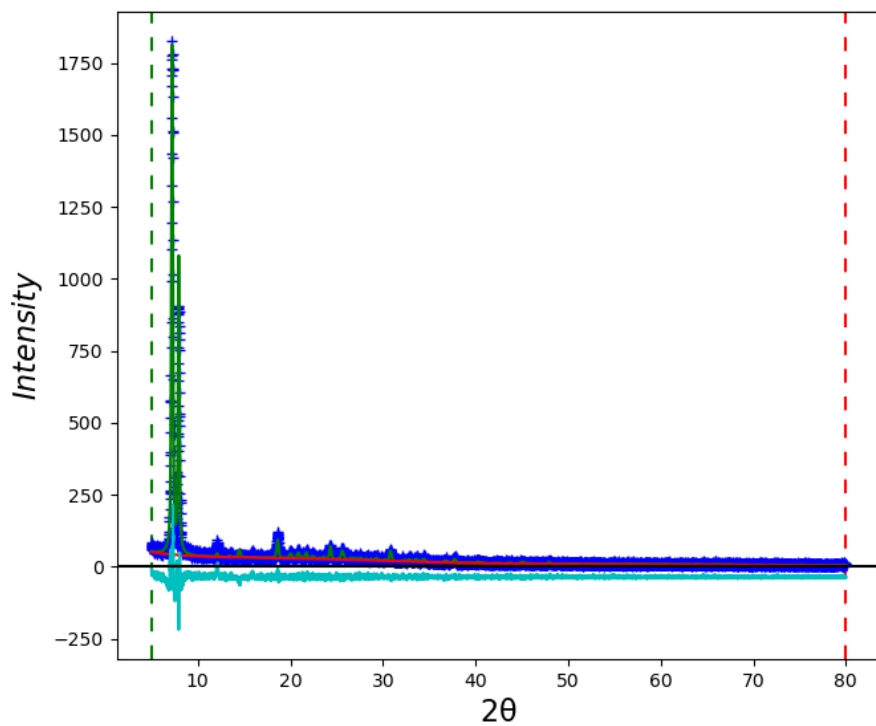


**Figure S11.** Powder XRD and Rietveld refinement of CuOEP. Dark blue = experimental data, green = simulation, teal = residuals, and red = baseline.

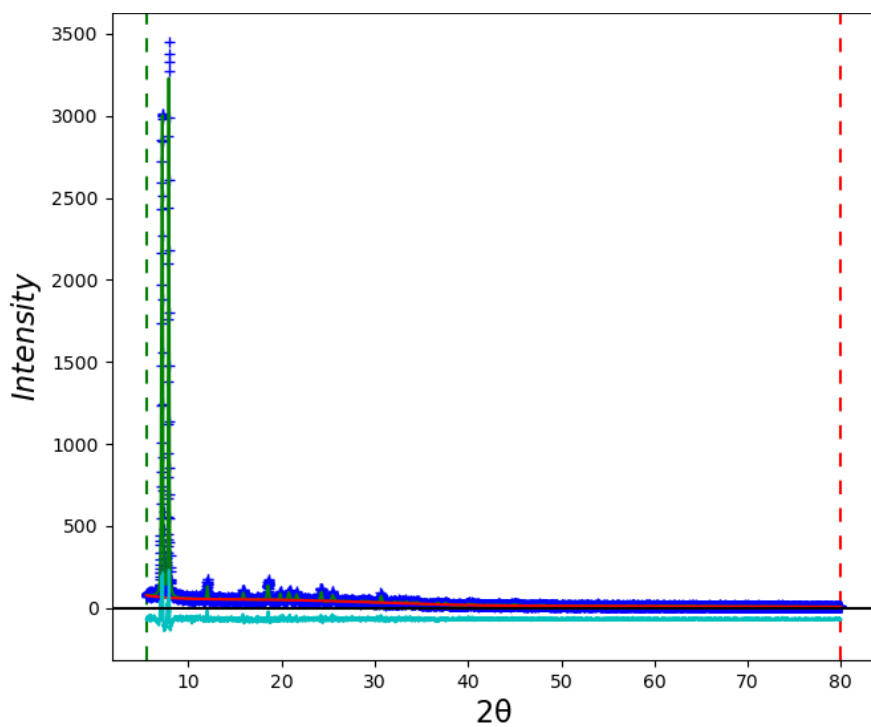


**Figure S12.** Powder XRD and Rietveld refinement of ZnOEP. Dark blue = experimental data, green = simulation, teal = residuals, and red = baseline.

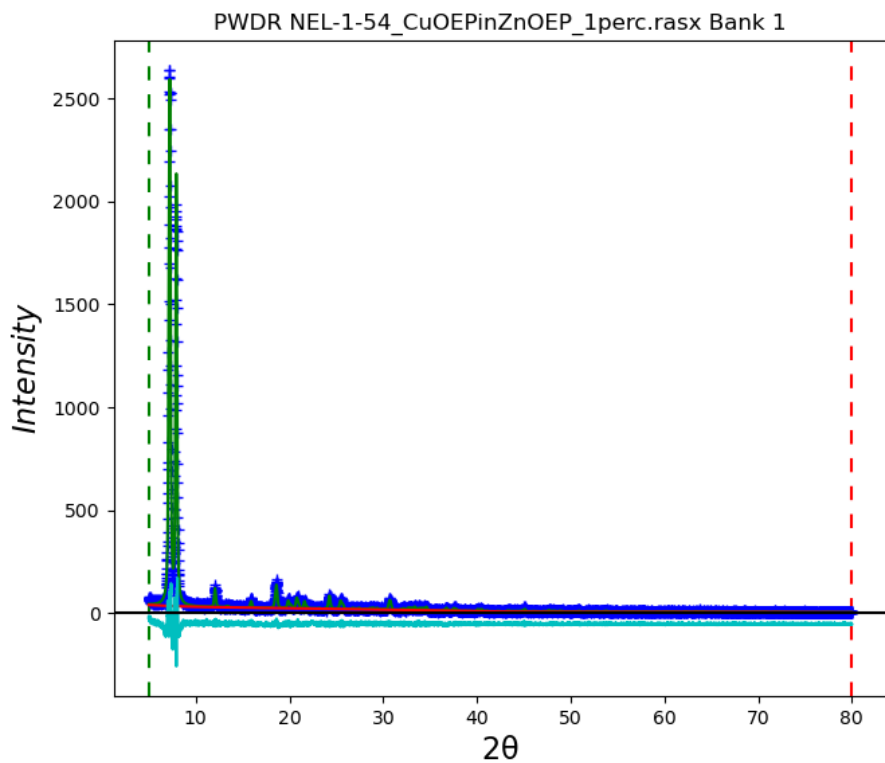


**Figure S13.** Powder XRD and Rietveld refinement of 1:100 CuOEP:ZnOEP used for EPR spectroscopy. Dark blue = experimental data, green = simulation, teal = residuals, and red = baseline.

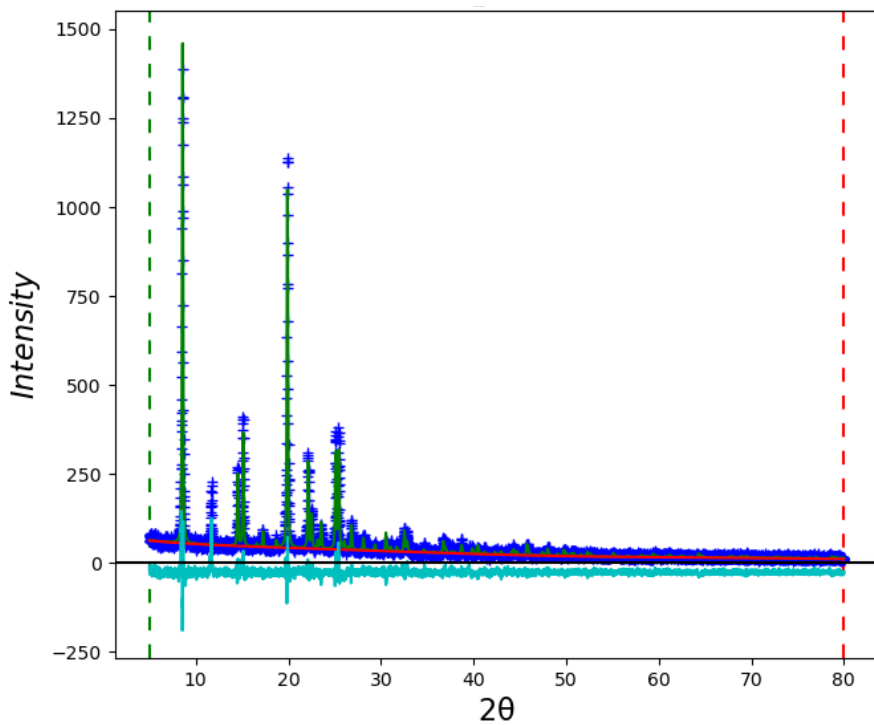


**Figure S14.** Powder XRD and Rietveld refinement of CuTPP. Dark blue = experimental data, green = simulation, teal = residuals, and red = baseline.

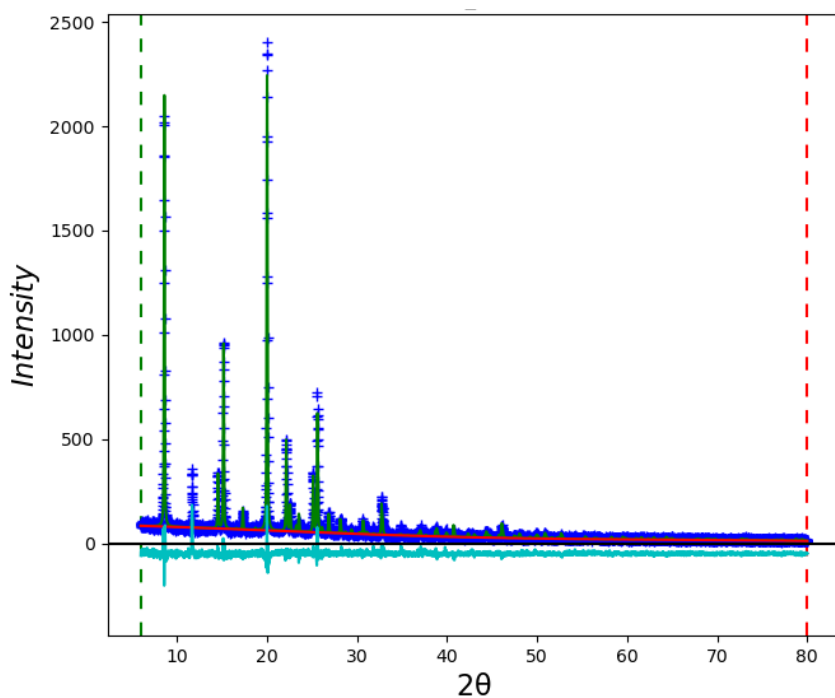


**Figure S15.** Powder XRD and Rietveld refinement of NiTPP. Dark blue = experimental data, green = simulation, teal = residuals, and red = baseline.

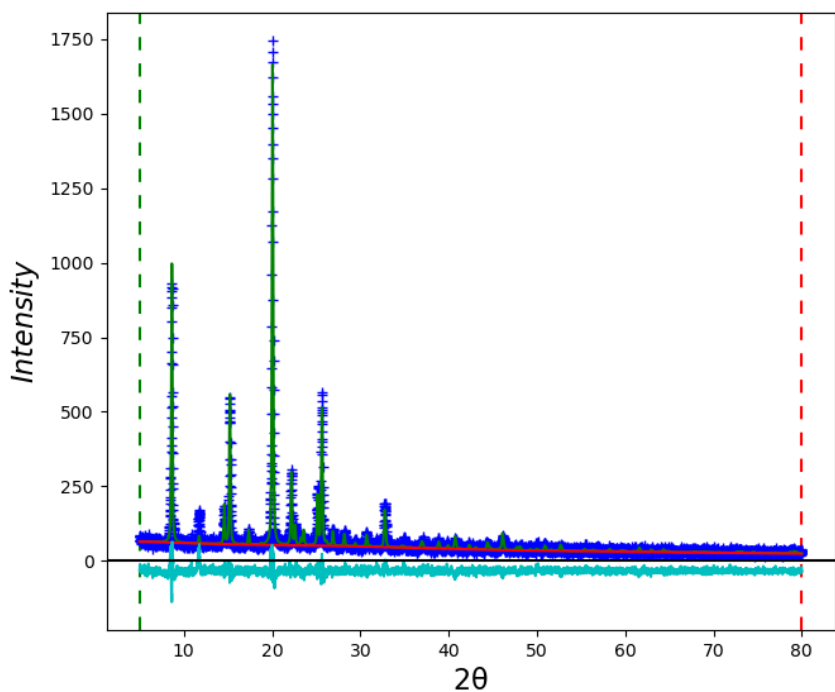


**Figure S16.** Powder XRD and Rietveld refinement of 1:100 CuTPP:NiTPP used for EPR spectroscopy. Dark blue = experimental data, green = simulation, teal = residuals, and red = baseline.

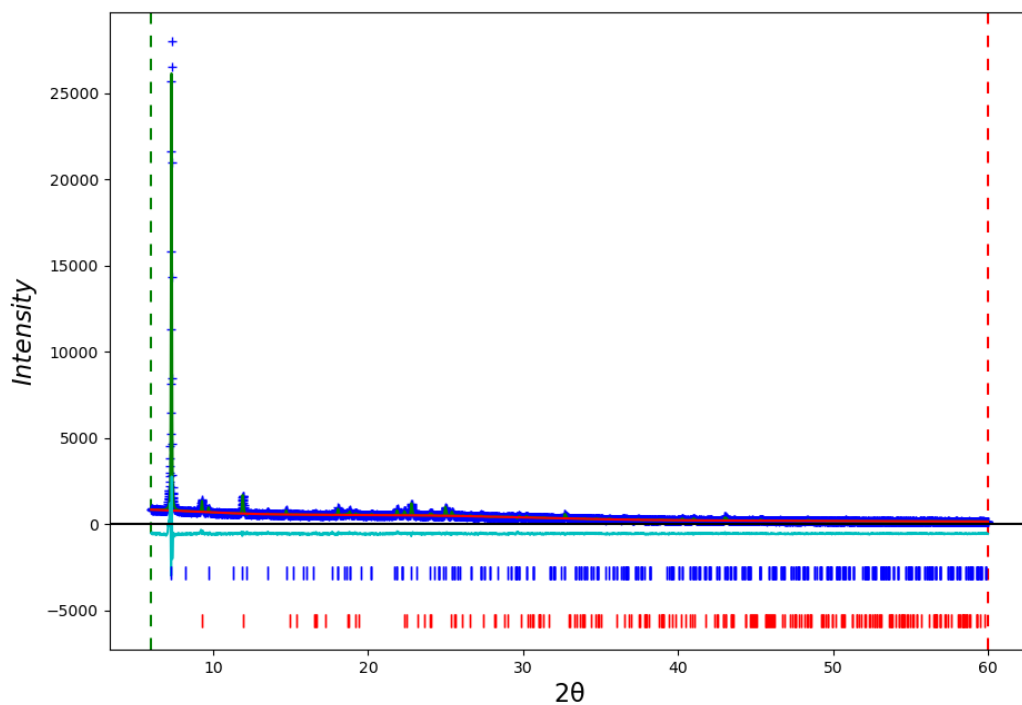


**Figure S17.** Powder XRD and Rietveld refinement of CuTiPP. Dark blue = experimental data, green = simulation, teal = residuals, and red = baseline. Blue ticks:  $I4_1$  crystal phase reflections. Red ticks:  $Fdd2$  crystal phase reflections. Note particularly the region from 9-10°, where both phases are required to fit prominent reflections.

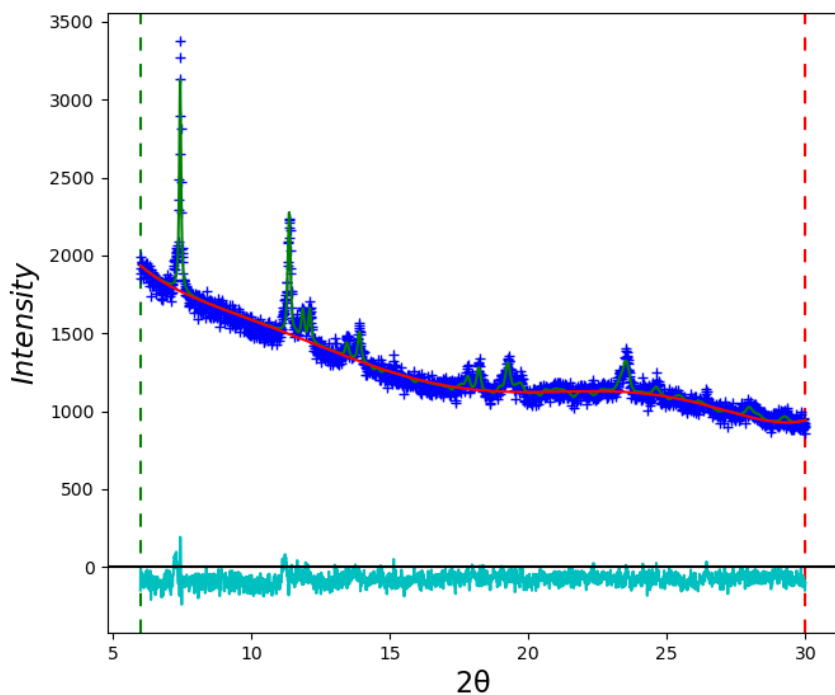


**Figure S18.** Powder XRD and Rietveld refinement of NiTiPP. Dark blue = experimental data, green = simulation, teal = residuals, and red = baseline.

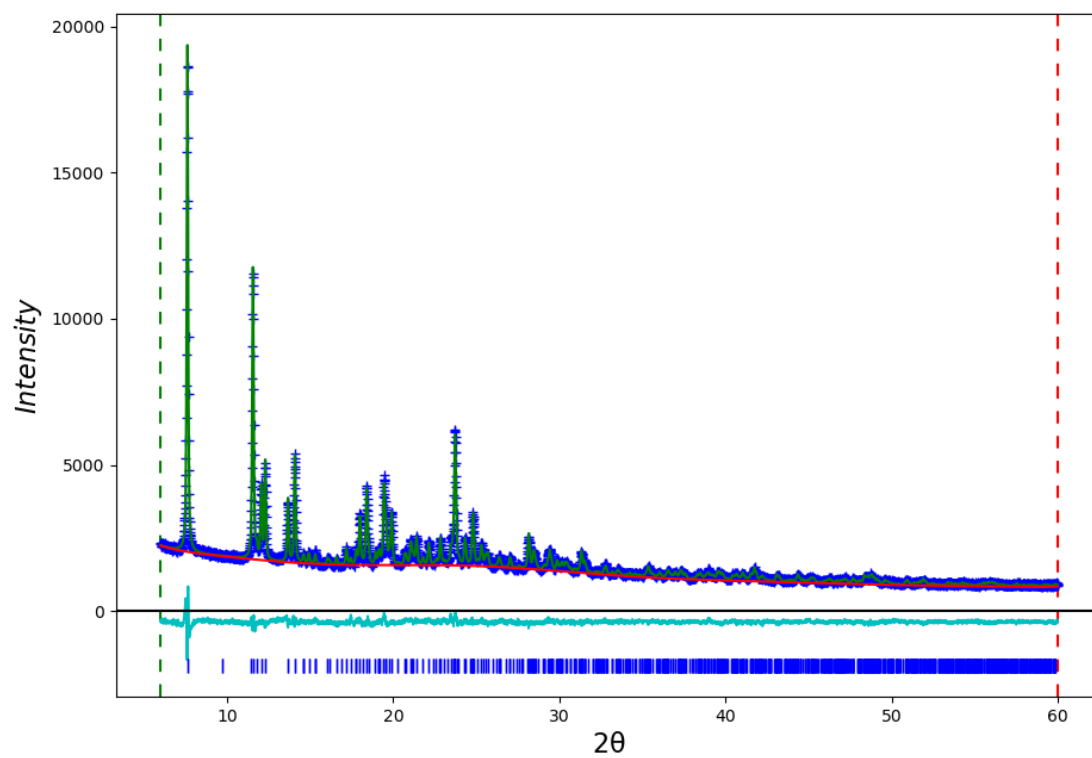


**Figure S19.** Powder XRD and Rietveld refinement of 1:100 CuTiPP:NiTiPP. Dark blue = experimental data, green = simulation, teal = residuals, and red = baseline.

**Table S1.** Starting and optimized parameters from Rietveld refinement. Blank cells are constrained by space group symmetry.

Compound	Space group		a (Å)	b (Å)	c (Å)	$\alpha$ (°)	$\beta$ (°)	$\gamma$ (°)	wR (%)
CuOEP	P-1	initial	13.31	13.39	4.81	92.42	93.38	113.08	20.7
		refined	13.29	13.39	4.81	92.26	93.68	113.17	
ZnOEP	P-1	initial	4.69	13.19	13.29	113.94	91.17	92.16	16.5
		refined	4.70	13.24	13.39	113.20	91.27	91.68	
1:100 CuOEP:ZnOEP	P-1	initial	4.69	13.19	13.29	113.94	91.18	92.16	19.6
		refined	4.67	13.25	13.43	113.17	91.43	92.04	
CuTPP	I-42d	initial	15.03		13.99				18.0
		refined	15.08		13.97				
NiTPP	I-42d	initial	15.06		13.86				15.5
		refined	15.08		13.89				
1:100 CuTPP:NiTPP	I-42d	initial	15.06		13.86				16.2
		refined	15.09		13.89				
CuTiPP	I4 <sub>1</sub>	initial	10.88		47.54				8.5
		refined	10.99		47.92				
	Fdd2	initial	20.29	21.10	12.28				
		refined	20.44	21.24	12.35				
NiTiPP	P2 <sub>1</sub> /c	initial	22.93	9.71	12.09		92.86		3.1
		refined	23.12	9.83	12.13		93.15		
1:100 CuTiPP:NiTiPP	P2 <sub>1</sub> /c	initial	22.93	9.71	12.09		92.86		3.4
		refined	23.09	9.83	12.09		92.94		

### C. Single Crystal X-Ray Structure Determination

Low-temperature diffraction data ( $\phi$ - and  $\omega$ -scans) were collected on a Bruker AXS D8 VENTURE KAPPA diffractometer coupled to a PHOTON II CPAD detector with  $K\alpha$  radiation ( $\lambda = 1.54178$  Å) from an I $\mu$ S micro-source for the structure of compound V23325. The structure was solved by direct methods using SHELXS<sup>12</sup> and refined against  $F^2$  on all data by full-matrix least squares with SHELXL-2019<sup>13</sup> using established refinement techniques.<sup>14</sup> All non-hydrogen atoms were refined anisotropically. All hydrogen atoms were included into the model at geometrically calculated positions and refined using a riding model. The isotropic displacement parameters of all hydrogen atoms were fixed to 1.2 times the  $U$  value of the atoms they are linked to (1.5 times for methyl groups). All disordered atoms were refined with the help of similarity restraints on the 1,2- and

1,3-distances and displacement parameters as well as enhanced rigid bond restraints for anisotropic displacement parameters.

Compound CuTiPP (**Figure S20**) crystallizes in the tetragonal space group  $I4_1$  with two half molecules in the asymmetric unit along with half a molecule of dichloromethane. The crystal was refined as a twin  $(-1\ 0\ 0\ 0\ 1\ 0\ 0\ 0\ -1)$ . The two copper molecules and the dichloromethane were located near a crystallographic 2-fold rotation. Most of the atoms in the molecules did not strictly obey the rotation and were disordered appropriately.

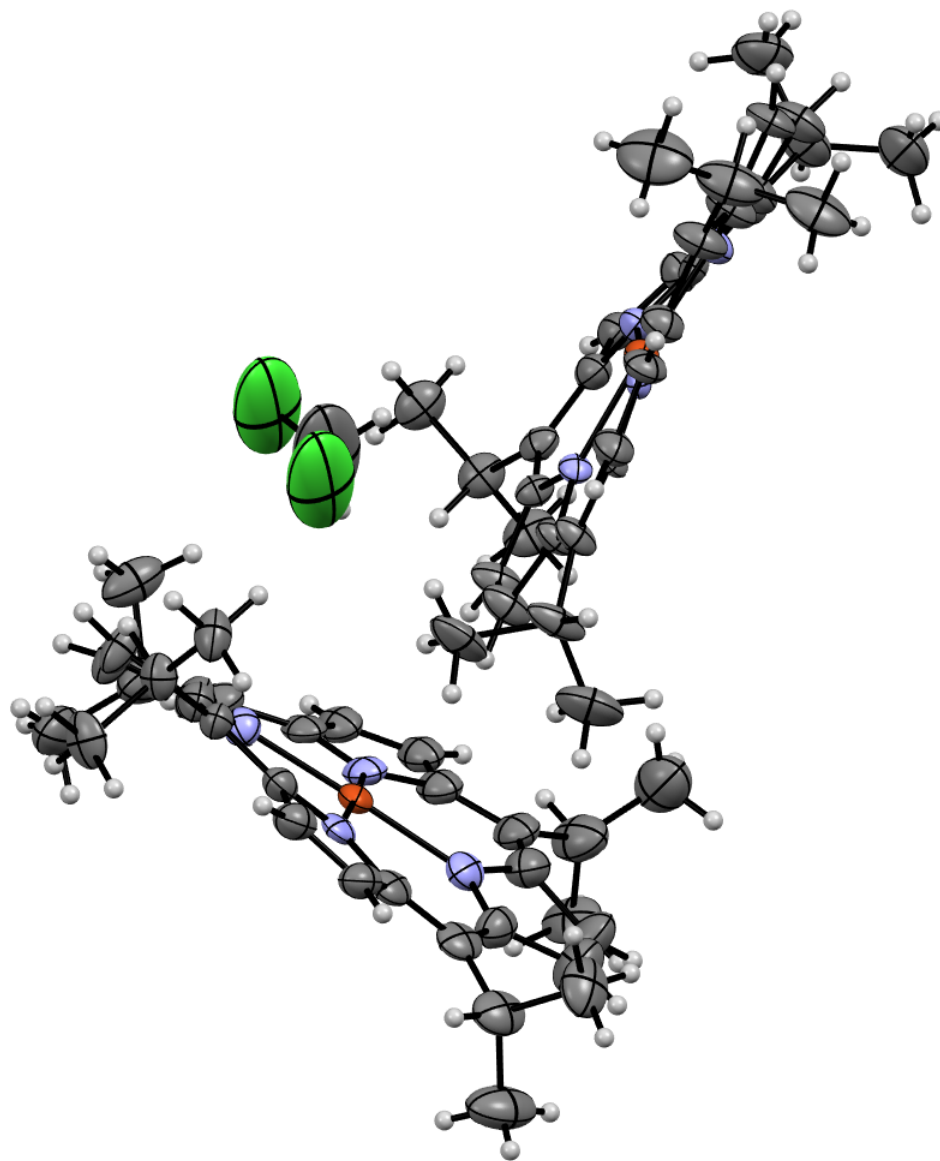


**Figure S20.**  $I4_1$  X-ray diffraction structure of CuTiPP with dichloromethane solvent molecule. Asymmetric unit cell displayed.

## D. Resonance Raman Spectroscopy

Liquid and solid samples for Raman spectroscopy were confined in glass capillary tubes or NMR tubes. All spectra were measured at room temperature. Samples were irradiated at a  $65^\circ$  angle of incidence with the 457.9 nm line from an Ar-ion laser (Coherent INNOVA 70). Radiation scattered around  $0^\circ$  was collected ( $f/2$ ) using a 100 mm Cannon macro camera lens, passed through a depolarizer, and filtered with a 457.9 nm sharp edge longpass filter (Iridian Spectral Technologies), focused onto the entrance slit of a Spex 0.75 m spectrograph, and detected using a thermoelectrically cooled CCD camera (Horiba Synapse). A polarizer was inserted between the lens and the depolarizer to acquire the polarized Raman spectra. Parallel and perpendicular polarized spectra were acquired under identical acquisition parameters for direct intensity comparison, and the depolarization ratio of the instrument was verified with  $\text{CCl}_4$ . Data acquisition, controlled by HoribaSynerJY software, involved averaging multiple exposures between 0.5 and 5 seconds to achieve acceptable signal-to-noise levels. The power was controlled to ensure no bleaching over time was visible in the individual exposures, and was no greater than 40 mW for any spectrum. Background Raman spectra of the capillary tubes were collected on samples of carbon black and subtracted from the data as necessary. Raman spectra were baselined using a polynomial fit to an asymmetric least squares penalty function; an example is given in **Figure S21**. For solution-phase Raman spectra, the monochromator positions were internally calibrated to the solvent peaks of  $\text{C}_6\text{H}_6$  and  $\text{CS}_2$ . For solid-phase Raman spectra, the monochromator was externally calibrated to either pure  $\text{C}_6\text{H}_6$  solvent or citric acid powder. The x-axis position of Raman peaks is accurate to within  $\pm 5 \text{ cm}^{-1}$ .

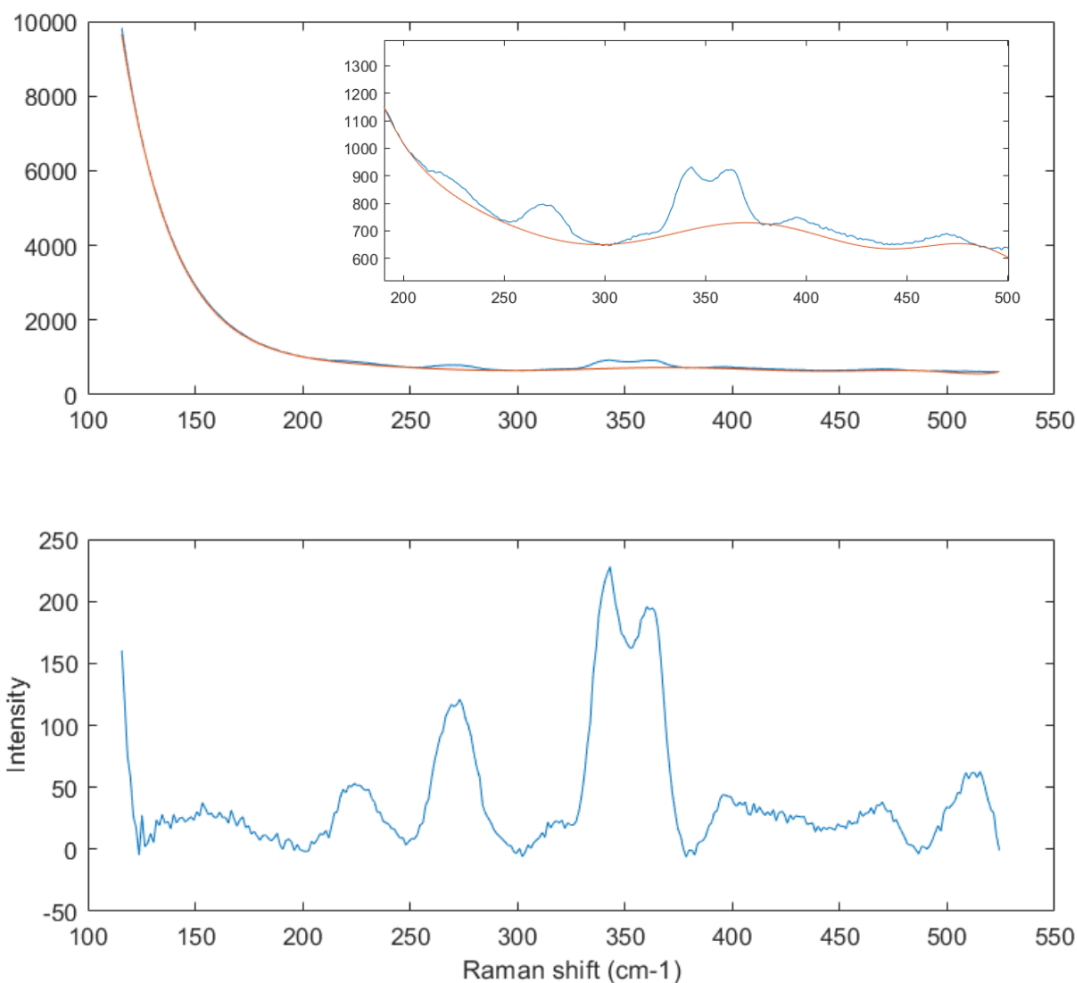


**Figure S21.** Raman spectra of 2 mM CuOEP in CS<sub>2</sub> demonstrating representative baselining procedure. Top: raw data after carbon black subtraction and fitted baseline. Bottom: Baseline-subtracted Raman spectrum. The rise at 150 cm<sup>-1</sup> arises from imperfect baseline subtraction of the Rayleigh scattering rather than a Raman peak from CuOEP.

**Figures S22 – S24** display the polarized Raman spectra for CuOEP in CS<sub>2</sub> and CuTPP and CuTiPP in C<sub>6</sub>H<sub>6</sub>. Note that CuOEP samples were insufficiently soluble in C<sub>6</sub>H<sub>6</sub> to obtain acceptable spectra at 457.9 nm excitation, while CuTPP appeared to form a secondary species or decompose in CS<sub>2</sub>, leading to a very large increase in the number of Raman peaks.

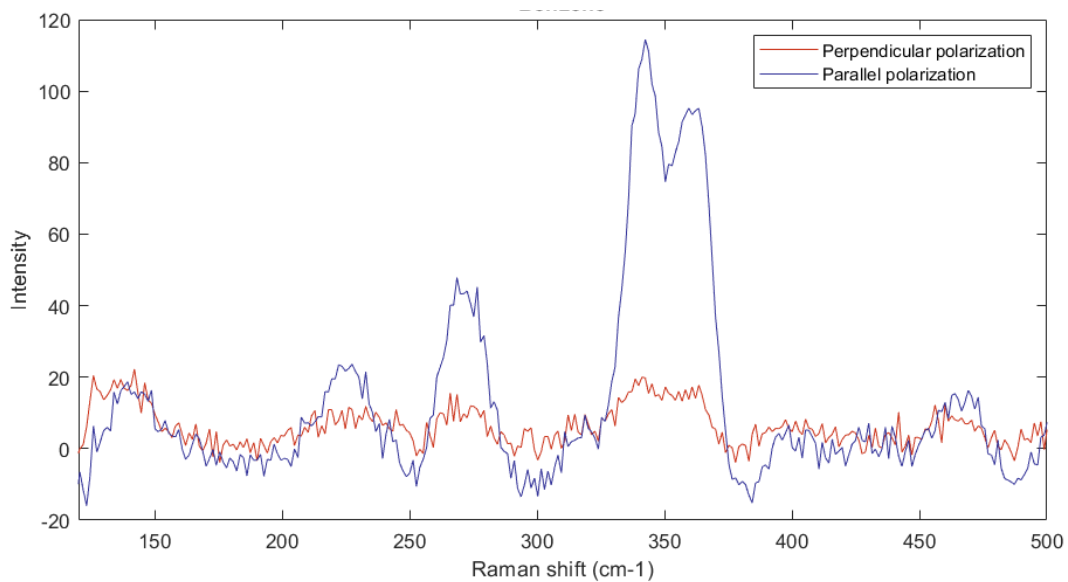


**Figure S22.** Polarized Raman spectra of 2 mM CuOEP in CS<sub>2</sub>. All sample bands are strongly polarized.

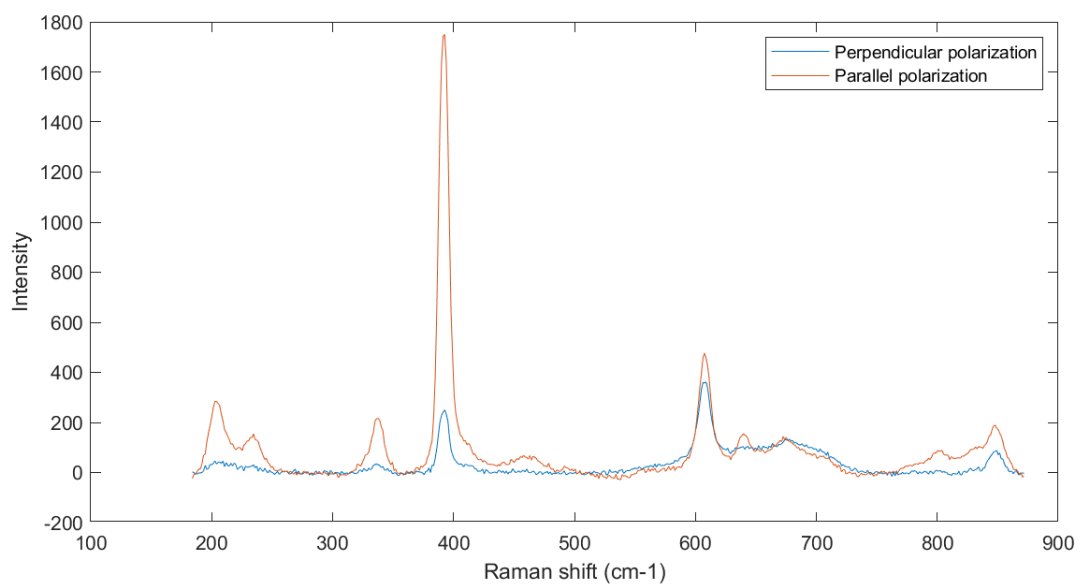


**Figure S23.** Polarized Raman spectra of 2 mM CuTPP in C<sub>6</sub>H<sub>6</sub>. The depolarized 605 cm<sup>-1</sup> arises from the solvent; sample bands below 430 cm<sup>-1</sup> are strongly polarized.

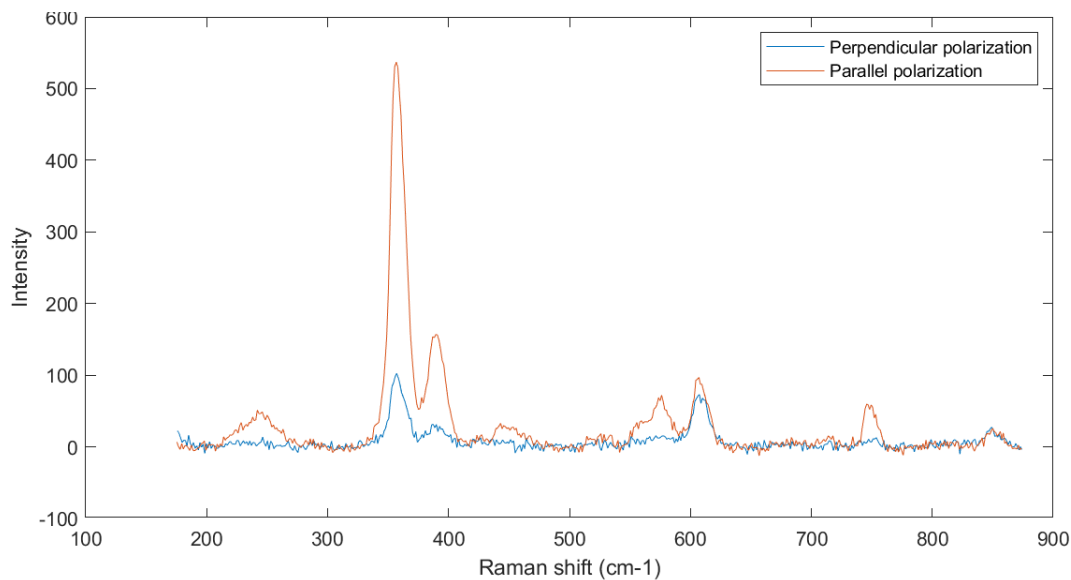


**Figure S24.** Polarized Raman spectra of 2 mM CuTiPP in C<sub>6</sub>H<sub>6</sub>. The depolarized 605 cm<sup>-1</sup> arises from the solvent; sample bands below 430 cm<sup>-1</sup> are strongly polarized.

Solid-state Raman spectra were acquired for CuOEP, CuTPP, and CuTiPP to verify that the vibrational frequencies are directly comparable to the solid-state EPR samples. Note that CuOEP displayed greater propensity to beam damage than CuTPP or CuTiPP, leading to lower signal-to-noise Raman spectra. The feature at 145 cm<sup>-1</sup> is a plasma line from the Ar<sup>+</sup> ion laser for all three spectra, which also arises in the carbon black baseline spectra. The peak positions are extracted and given in **Table S2**, demonstrating that the frequencies match very well between the solid state and solution phase samples. All bands are within 8 cm<sup>-1</sup> for solution vs. solid state spectra, and the key ligand symmetric stretch mode agrees to within 2 cm<sup>-1</sup> for all compounds (CuOEP and CuTiPP: peak 2; CuTPP: peak 1).

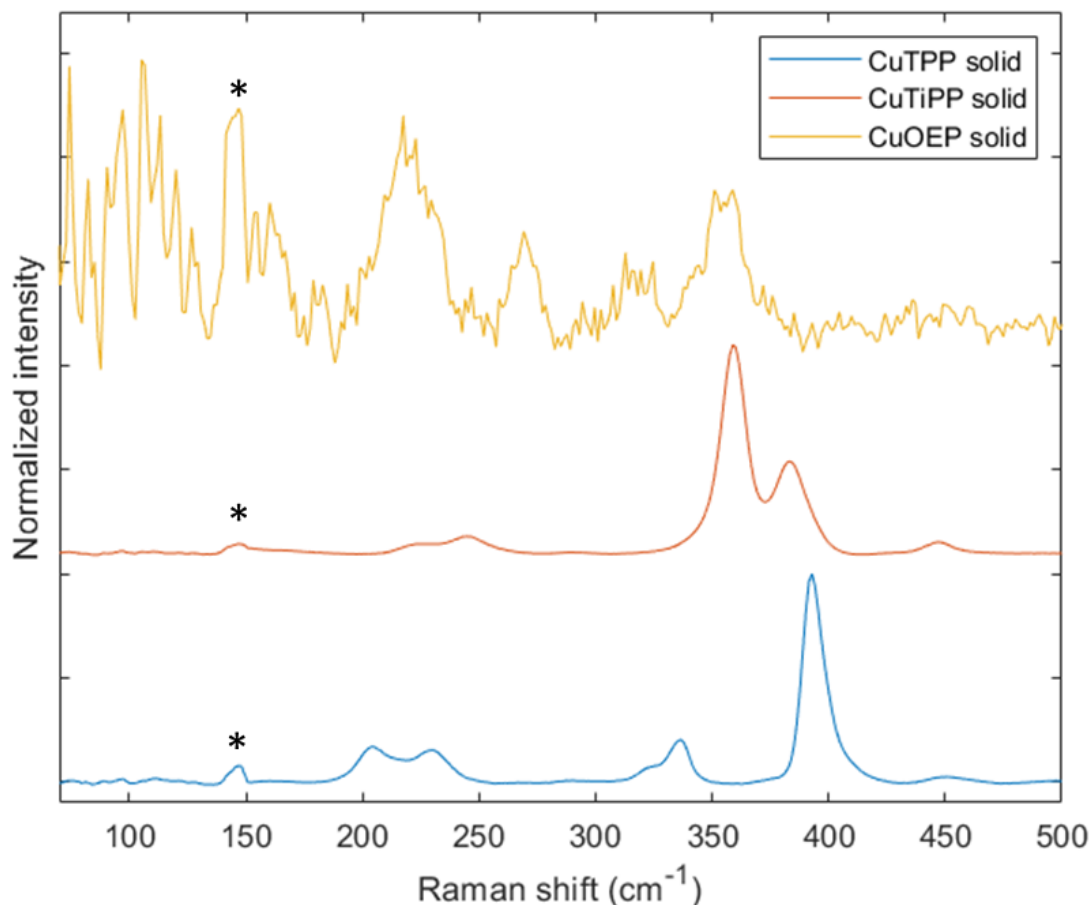


**Figure S25:** Solid state Raman spectra of CuOEP, CuTiPP, and CuTPP. Asterisk denotes plasma line artifact.

**Table S2:** Raman peak positions for four main vibrational modes below 430  $\text{cm}^{-1}$ . All energies in  $\text{cm}^{-1}$ . “sh” denotes shoulder.

Sample	Peak 1	Peak 2	Peak 3	Peak 4
CuOEP ( $\text{CS}_2$ )	224	271	343	361
CuOEP (solid)	220	269	351	359
CuTiPP ( $\text{C}_6\text{H}_6$ )	227	244	357	390
CuTiPP (solid)	224	245	359	383
CuTPP ( $\text{C}_6\text{H}_6$ )	203	233	337	392
CuTPP (solid)	204	230	337 (325 sh.)	393

### E. Continuous Wave Electron Paramagnetic Resonance Spectroscopy

Continuous wave X-band spectra were obtained on a Bruker EMX spectrometer using a liquid nitrogen immersion dewar. X-band CW spectra were fit in EasySpin 5.2.35 to extract the spin-Hamiltonian parameters.<sup>15</sup> All spectra were fit with the pepper function using isotropic line broadening (lwpp parameter). Fit results are tabulated in **Table S3**, and spectra with associated fits are given in **Figures S26-S28**.

**Table S3.** Simulated spin Hamiltonian parameters for CW EPR spectra of 1:100 solid state dilutions in the corresponding diamagnetic matrix (ZnOEP, NiTPP, NiTiPP).

	$g_{\parallel}$	$g_{\perp}$	$A_{Cu,\parallel}$ (MHz)	$A_{Cu,\perp}$ (MHz)	$A_{N,\parallel}$ (MHz)	$A_{N,\perp}$ (MHz)
CuOEP	2.195	2.047	606	79	44	50
CuTPP	2.176	2.043	625	86	46	51
CuTiPP	2.16	2.04	638	92	46	52

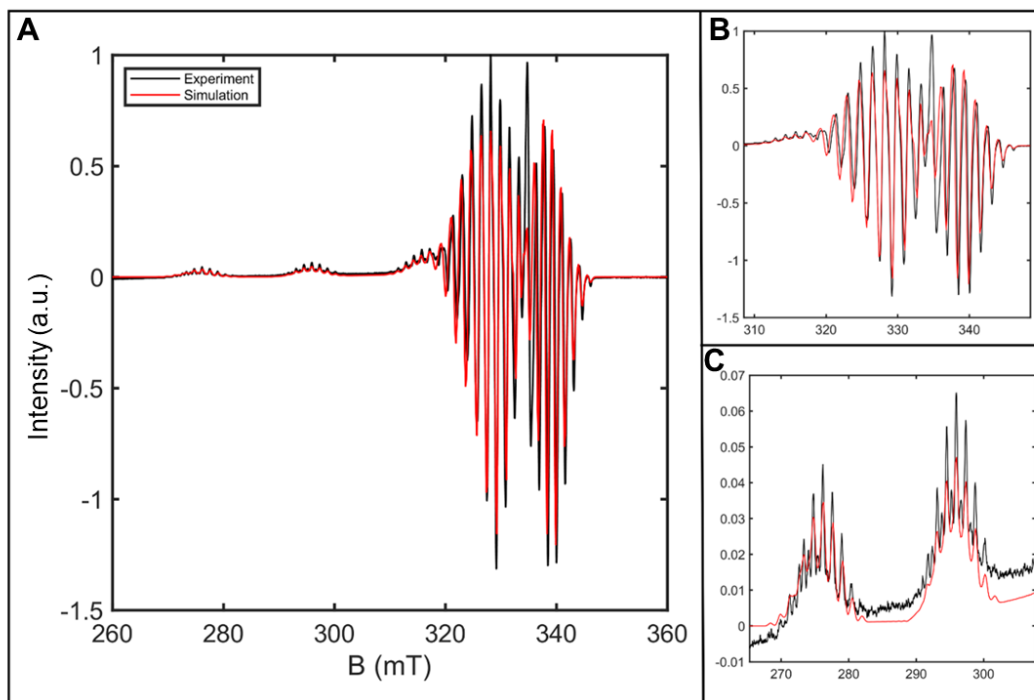


**Figure S26.** CW EPR spectrum of a 100 mg sample of 1% CuOEP in ZnOEP solid-state sample at 77 K. (A) Full data. (B) Perpendicular region zoom. (C) Parallel region zoom.

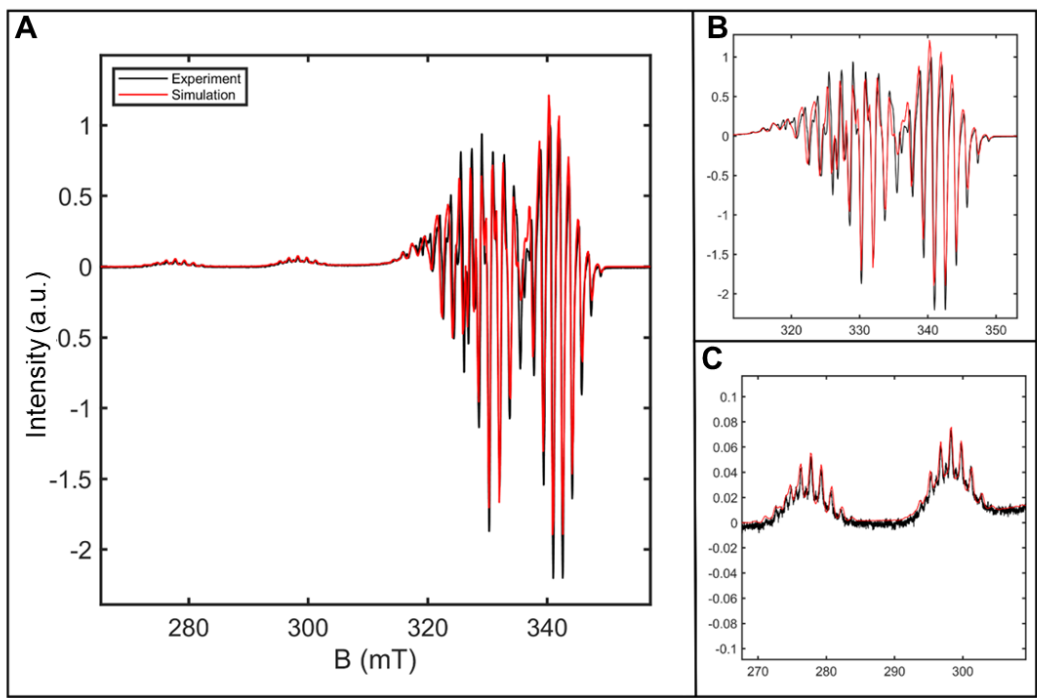


**Figure S27.** CW EPR spectrum of a 100 mg sample of 1% CuTPP in NiTPP solid-state sample at 77 K. (A) Full data. (B) Perpendicular region zoom. (C) Parallel region zoom.

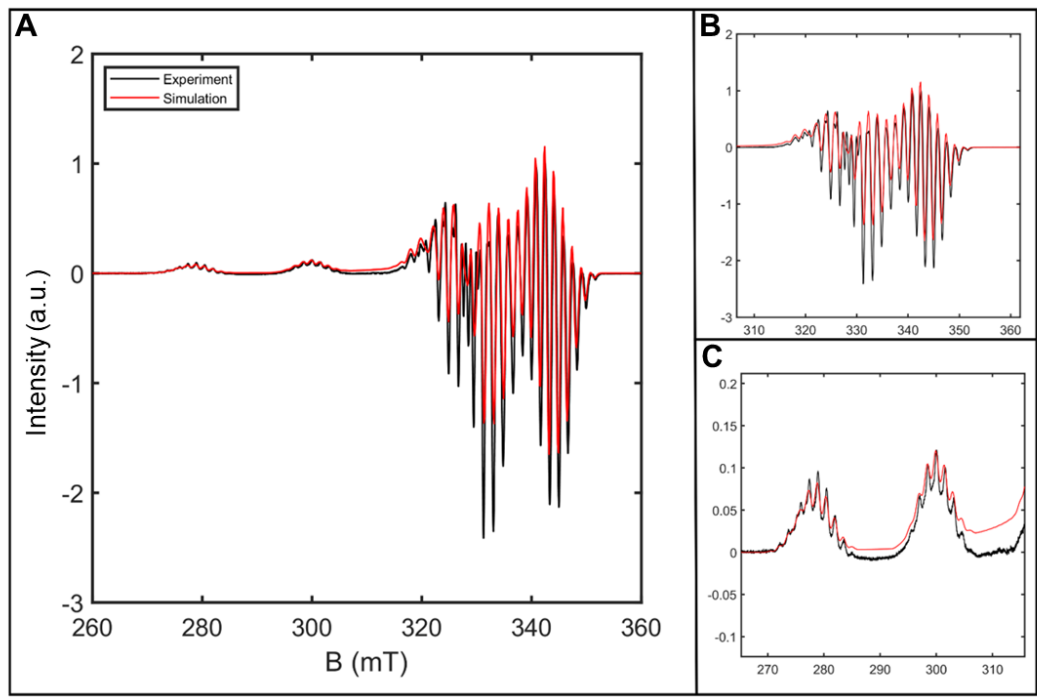


**Figure S28.** CW EPR spectrum of a 100 mg sample of 1% CuTiPP in NiTiPP solid-state sample at 77 K. (A) Full data. (B) Perpendicular region zoom. (C) Parallel region zoom.

## F. Pulse Electron Paramagnetic Resonance Spectroscopy

Pulse X-band EPR experiments were conducted with a Bruker ELEXSYS E580 pulse EPR spectrometer, using a combination of Bruker MS-5 and MD-4 resonators. Temperature control was achieved using an Oxford Instruments CF935 cryogen flow cryostat using liquid helium (5–100 K) or liquid nitrogen (>100 K) and a Mercury iTC temperature controller. Echo-detected field sweep spectra employed a two-pulse Hahn-echo sequence ( $\pi/2$ - $\tau$ - $\pi$ - $\tau$ -echo). Inversion recovery experiments employed the pulse sequence  $\pi$ - $t$ - $\pi/2$ - $\tau$ - $\pi$ - $\tau$ -echo, where  $t$  is the variable time delay and  $\tau$  is a fixed constant. Picket fence saturation recovery experiments employed eight consecutive  $\pi/2$  pulses with a fixed interpulse delay of 1  $\mu$ s. The fixed delay  $\tau$  was optimized independently for each sample to maximize the echo intensity. The video gain was optimized at each field position and temperature. Four-step phase cycling was used on inversion recovery measurements to eliminate influence of secondary echoes and microwave ringdown. The  $\pi/2$  pulses had a duration of 8 ns at X-band, while the  $\pi$  pulses had a duration of 16 ns. Inversion recovery experiments were fit to stretched exponential functions in Matlab R2020b according to Equation S1. Hahn-echo decay experiments to quantify  $T_m$  were fit to Equation S2. Error bars were obtained from the 95% confidence intervals on the fitted  $T_1$  or  $T_m$  parameters.

$$I = Ae^{[-(\frac{t}{T_1})^\beta]} + I_0 \quad (\text{S1})$$

$$I = Ae^{[-(\frac{2t}{T_m})^\beta]} + I_0 \quad (\text{S2})$$

For each compound, inversion recovery measurements from 5 – 100 K were collected in one session, 100 – 240 K in a second session, and room temperature in a third session. In some cases, these measurements could not be performed at the same microwave frequency, owing to the different resonant frequencies of the MS-5 (~9.4 GHz) and MD-4 (~9.7 GHz) resonators. To ensure the  $T_1$  measurements for parallel and perpendicular field positions could be directly compared across these sessions, the echo-detected field sweeps were acquired in each case, and the field was corrected so that the same location on the EDFS was probed at both frequencies. Additionally, we verified that the  $T_1$  values for the positions matched between sessions at a common observer position and temperature.

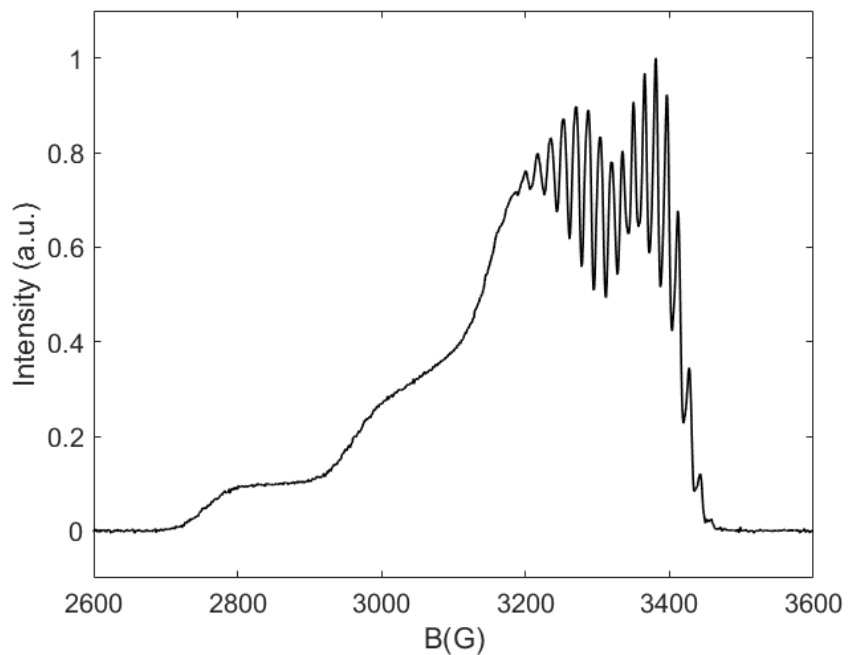


**Figure S29.** 100 K X-band (9.406 GHz) echo-detected field sweep of 1:100 CuOEP in ZnOEP.

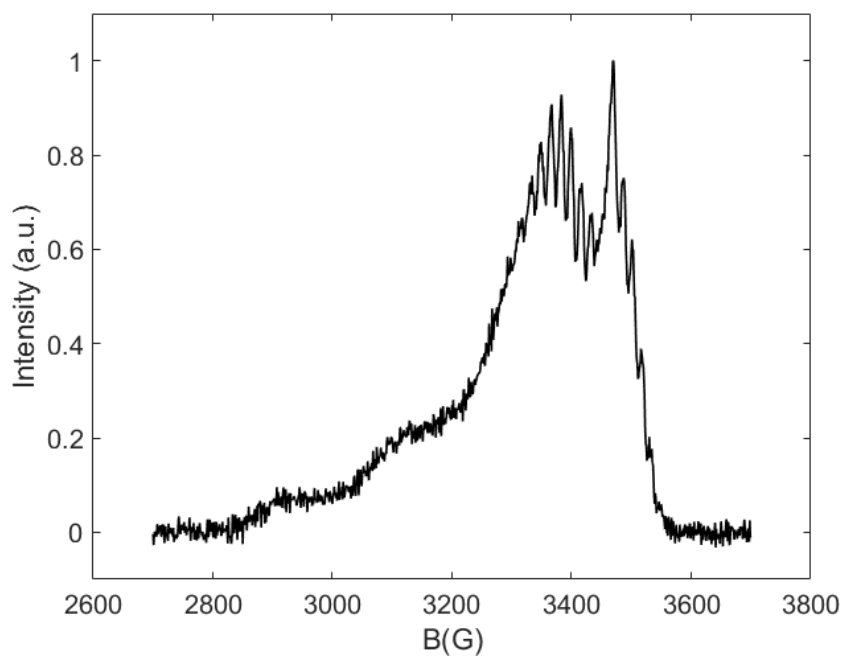


**Figure S30.** Room-temperature X-band (9.733 GHz) echo-detected field sweep of 1:100 CuOEP in ZnOEP.

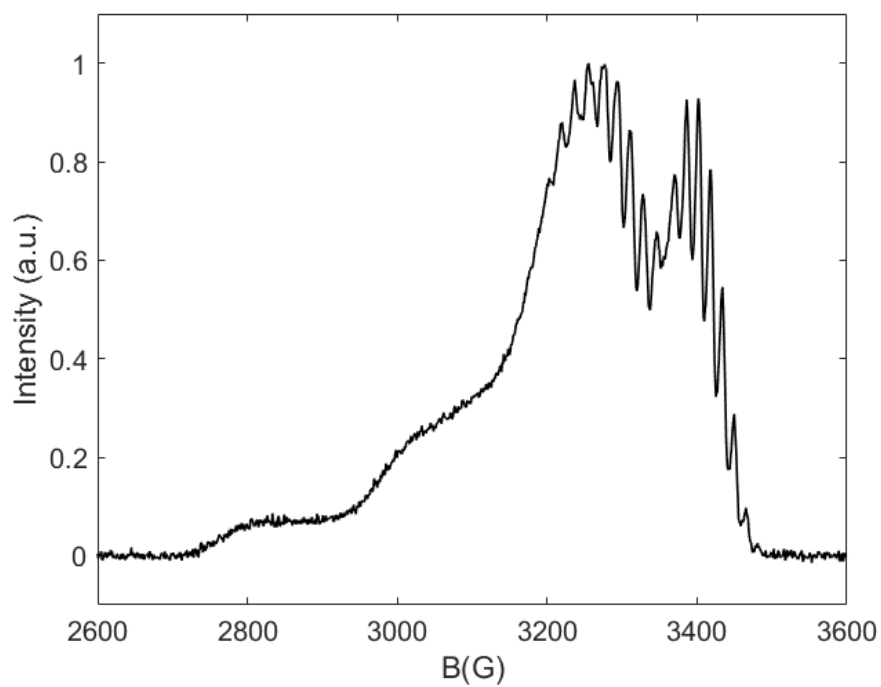


**Figure S31.** 100 K X-band (9.397 GHz) echo-detected field sweep of 1:100 CuTPP in NiTPP.

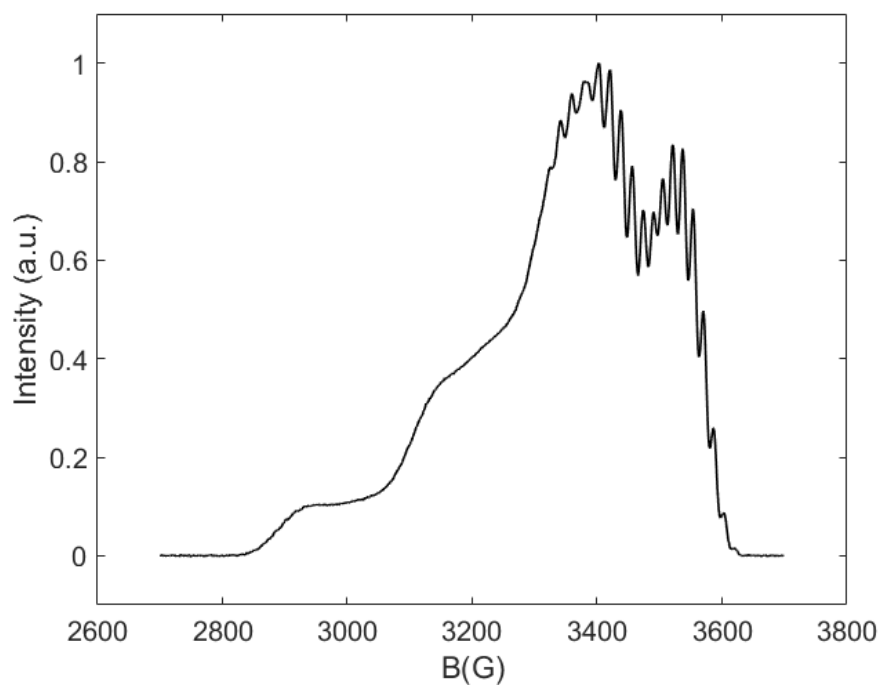


**Figure S32.** 100 K X-band (9.739 GHz) echo-detected field sweep of 1:100 CuTiPP in NiTiPP.

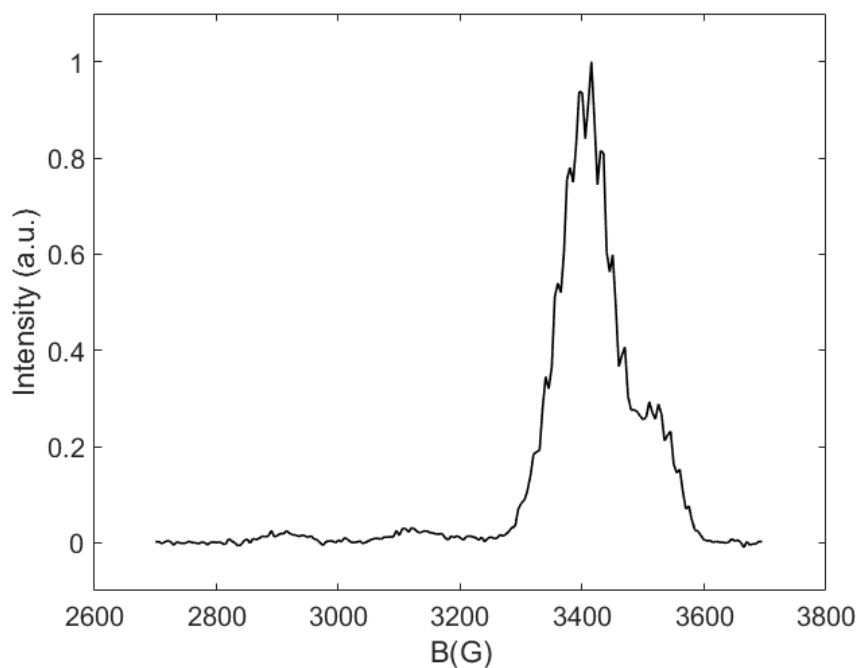


**Figure S33.** Room-temperature X-band (9.740 GHz) echo-detected field sweep of 1:100 CuTiPP in NiTiPP. The change in spectral shape from the 100K EDFS is attributed to  $T_m$  anisotropy and the extremely short  $T_m$  at this temperature.

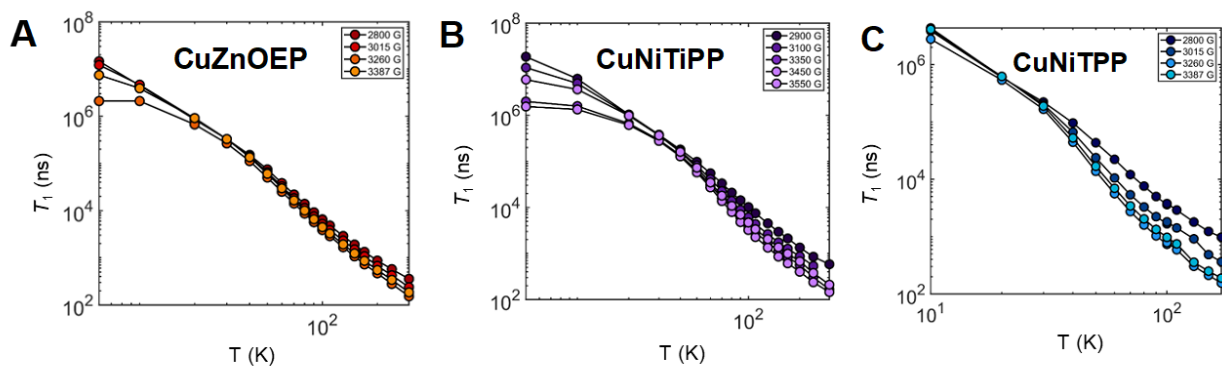


**Figure S34.** Variable-field log-log plots of  $T_1$  vs. temperature for 1% samples of CuZnOEP (A), CuNiTiPP (B), and CuNiTiPP (C) at 100 K. Field positions are given with reference to  $\sim 9.4$  GHz for CuZnOEP and CuNiTiPP, and  $\sim 9.7$  GHz for CuNiTiPP.

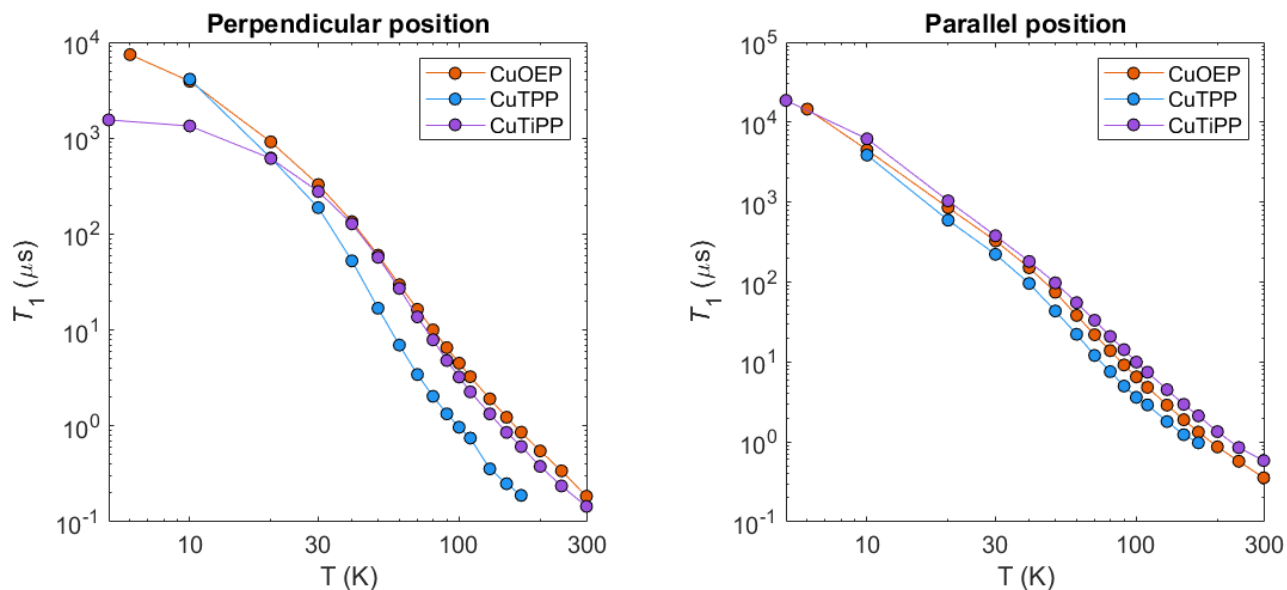


**Figure S35.** Log-log plot of  $T_1$  vs. temperature at perpendicular and parallel field positions for porphyrin solid state diamagnetic dilutions (X-band, inversion recovery).

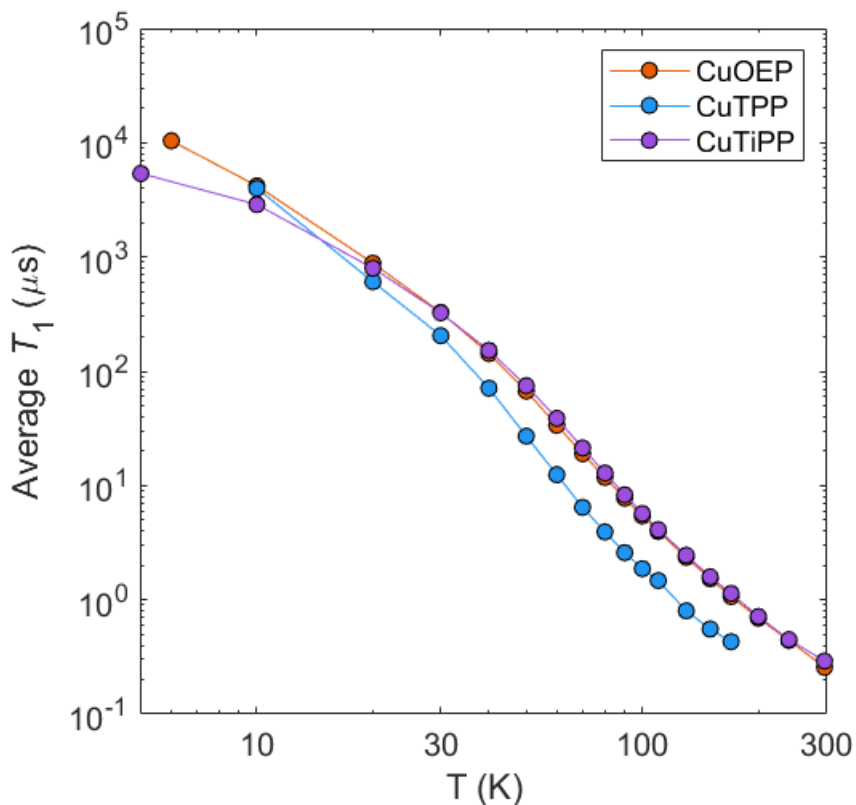


**Figure S36.** Average  $T_1$  vs. temperature across orientations for porphyrin solid state diamagnetic dilutions (X-band, inversion recovery). Average  $T_1$  is computed as the geometric mean of  $T_1$  at the parallel and perpendicular positions to respect the logarithmic scaling of the relaxation rate.

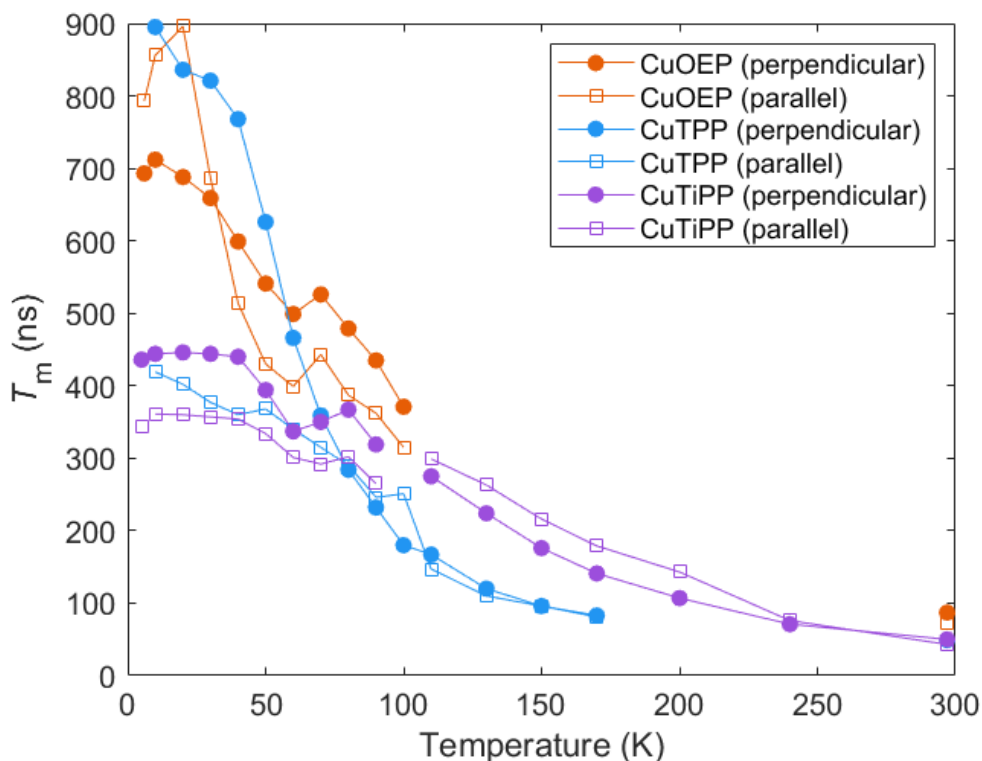


**Figure S37.**  $T_m$  vs. temperature (X-band, Hahn echo decay) for 1:100 solid state dilutions of copper porphyrins.

**Table S4.**  $T_1$  vs. temperature for perpendicular and parallel observer positions, measured via X-band inversion recovery. All samples are 1:100 solid state diamagnetic dilutions.

T(K)	CuOEP		CuTPP		CuTiPP	
	Perpendicular $T_1$ ( $\mu$ s)	Parallel $T_1$ ( $\mu$ s)	Perpendicular $T_1$ ( $\mu$ s)	Parallel $T_1$ ( $\mu$ s)	Perpendicular $T_1$ ( $\mu$ s)	Parallel $T_1$ ( $\mu$ s)
5	---	---	---	---	1.55E+03	1.87E+04
6	7.43E+03	1.46E+04	---	---	---	---
10	3.91E+03	4.50E+03	4.12E+03	3.87E+03	1.34E+03	6.19E+03
20	9.14E+02	8.52E+02	6.21E+02	5.94E+02	6.14E+02	1.04E+03
30	3.28E+02	3.28E+02	1.89E+02	2.22E+02	2.78E+02	3.79E+02
40	1.35E+02	1.51E+02	5.26E+01	9.60E+01	1.28E+02	1.81E+02
50	6.03E+01	7.45E+01	1.69E+01	4.34E+01	5.73E+01	9.76E+01
60	2.97E+01	3.82E+01	6.96E+00	2.22E+01	2.71E+01	5.52E+01
70	1.64E+01	2.19E+01	3.43E+00	1.21E+01	1.37E+01	3.32E+01
80	1.00E+01	1.39E+01	2.04E+00	7.59E+00	7.91E+00	2.09E+01
90	6.55E+00	9.18E+00	1.34E+00	5.00E+00	4.81E+00	1.43E+01
100	4.51E+00	6.52E+00	9.69E-01	3.61E+00	3.24E+00	9.97E+00
110	3.26E+00	4.82E+00	7.47E-01	2.91E+00	2.27E+00	7.46E+00
130	1.92E+00	2.89E+00	3.57E-01	1.80E+00	1.34E+00	4.51E+00
150	1.23E+00	1.90E+00	2.50E-01	1.23E+00	8.56E-01	2.95E+00

170	8.60E-01	1.33E+00	1.89E-01	9.76E-01	6.09E-01	2.12E+00
200	5.49E-01	8.68E-01	---	---	3.79E-01	1.35E+00
240	3.40E-01	5.73E-01	---	---	2.37E-01	8.50E-01
297	1.85E-01	3.56E-01	6E-02	---	1.45E-01	5.84E-01

**Table S5.**  $T_m$  vs. temperature for perpendicular and parallel observer positions, measured via X-band Hahn echo decay. All samples are 1:100 solid state diamagnetic dilutions.

T(K)	CuOEP		CuTPP		CuTiPP	
	Perpendicular $T_m$ (ns)	Parallel $T_m$ (ns)	Perpendicular $T_m$ (ns)	Parallel $T_m$ (ns)	Perpendicular $T_m$ (ns)	Parallel $T_m$ (ns)
5	---	---	---	---	436	344
6	693	793	---	---	---	---
10	712	856	895	419	444	361
20	688	896	836	402	446	360
30	659	687	821	377	444	357
40	599	514	768	360	440	354
50	541	430	626	368	394	334
60	499	399	466	340	337	301
70	526	443	359	315	350	292
80	479	387	284	290	367	302
90	435	362	232	246	319	265
100	371	315	180	251	---	---
110	---	---	167	147	275	299
130	---	---	120	110	224	263
150	---	---	96	96	176	216
170	---	---	83	81	141	179
200	---	---	---	---	107	143
240	---	---	---	---	71	76
297	87	73	49	---	50	43

**Table S6.**  $T_1$  and  $T_m$  at room temperature for parallel and perpendicular orientations. All samples are 1:100 solid state diamagnetic dilutions.

	CuOEP		CuTPP		CuTiPP	
	Perpendicular	Parallel	Perpendicular	Parallel	Perpendicular	Parallel
$T_1$ (ns)	149	356	60	N/A	145	584
$T_m$ (ns)	87	73	49	N/A	50	43

**Table S7** is an expanded form of **Table 2** to show the parallel orientation fitted local mode energy and the average of the two fitted local mode energies. The relative local mode energies for CuOEP vs. CuTiPP change with field position, in accordance with the changing relative ordering of the CuOEP/CuTiPP  $T_1$  values themselves at the different positions (**Figure S35**). However, the

common feature over all orientations is the distinctly lower CuTPP local mode energy as compared to CuOEP and CuTiPP.

**Table S7:** Positions of fitted local mode energies for different  $T_1$  orientations in EPR, and comparison to ligand symmetric mode from experimental Raman spectroscopy.

Compound	Perpendicular local mode (cm <sup>-1</sup> )	Parallel local mode (cm <sup>-1</sup> )	Average local mode (cm <sup>-1</sup> )	Raman mixed LSS mode (cm <sup>-1</sup> )
CuOEP	258	247	253	271
CuTiPP	251	265	258	244
CuTPP	220	206	213	203

**Table S8** tabulates the complete coefficients obtained from the local mode fits via Equation 2. Coefficient  $a$  gives the coupling strength of the power law contribution, while  $n$  gives the temperature scaling of the power law contribution. Coefficient  $b$  gives the coupling strength of the local mode contribution. The  $b$  coefficients are similar between the three compounds at the parallel orientation, but vary by a factor of 3 at the perpendicular orientation. This points to the presence of variable  $T_1$  anisotropy for the different porphyrins, which arises in the local mode fits through the  $b$  coefficient. The  $b$  coefficients themselves are not sufficient to explain the fast spin relaxation in CuTPP vs. CuOEP and CuTiPP at all orientations. CuOEP possesses a larger  $b$  coefficient than CuTPP at the parallel orientation, yet CuOEP undergoes slower relaxation. However,  $E_{loc}$  trends correctly with the experimental  $T_1$  ordering in all cases. This points to the primary role of the molecular vibration energy  $E_{loc}$  in determining the ordering of the  $T_1$  values.

**Table S8:** Prefactor coefficients ( $a$ ,  $b$ ) and power law exponents ( $n$ ) for local mode fits via Equation 2.

Compound	Perpendicular orientation				Parallel orientation			
	$a$ ( $\mu\text{s}^{-1}$ )	$b$ ( $\mu\text{s}^{-1}$ )	$n$	$E_{loc}$ (cm <sup>-1</sup> )	$a$ ( $\mu\text{s}^{-1}$ )	$b$ ( $\mu\text{s}^{-1}$ )	$n$	$E_{loc}$ (cm <sup>-1</sup> )
CuOEP	$9.0 \times 10^{-7}$	6.8	2.4	258	$8.7 \times 10^{-7}$	3.3	2.4	247
CuTiPP	$1.9 \times 10^{-5}$	10.5	1.5	251	$5.2 \times 10^{-7}$	2.0	2.5	265
CuTPP	$4.4 \times 10^{-7}$	21.3	2.7	220	$8.1 \times 10^{-7}$	3.0	2.5	206

To exclude the possibility of spectral diffusion being responsible for the observed changes in  $T_1$ , picket fence saturation recovery measurements were acquired on 1% diamagnetic dilution samples of CuOEP in ZnOEP and CuTPP in NiTPP at 30 K and 100 K. Electron spin-spin couplings arising from the doping concentration were similarly excluded by inversion recovery measurements on 0.1% samples of CuOEP in ZnOEP and CuTPP in NiTPP.  $T_1$  values were compared to inversion recovery measurements on 1% samples acquired on the same day for exact comparability of microwave frequency and cryostat setup. Saturation recovery measurements yield longer  $T_1$  values

by <10%, while 0.1% concentration samples yield shorter or longer  $T_1$  values by ~10% (**Table S9-S12**). Spectral diffusion and sample-to-sample concentration effects therefore set a lower limit of 10% on the relative  $T_1$  difference between two compounds that can be reliably distinguished. However, the relative  $T_1$  differences between the three CuP species are all between 15% - 78%, with an average relative difference of 43% (**Table S13**). Therefore, spectral diffusion and concentration effects are too small to account for the observed differences in the CuP species.

**Table S9:** Comparison of concentration and pulse sequence effects on measured  $T_1$  for CuOEP in ZnOEP at 100 K (9.7332 GHz). Uncertainty estimates are 95% confidence intervals from the stretched exponential fit.

Pulse sequence	Paramagnetic concentration	$T_1$ ( $\mu$ s)		% change over 1 to 100 inversion recovery	
		2910 G ( $\parallel$ )	3491 G ( $\perp$ )	2910 G ( $\parallel$ )	3491 G ( $\perp$ )
Inversion recovery	1 to 100	$6.68 \pm 0.03$	$4.577 \pm 0.009$	N/A	N/A
Inversion recovery	1 to 1000	$6.5 \pm 0.2$	$4.48 \pm 0.04$	-2.7%	-2.1%
Saturation recovery	1 to 100	$6.76 \pm 0.09$	$4.66 \pm 0.04$	1.2%	1.8%

**Table S10:** Comparison of concentration and pulse sequence effects on measured  $T_1$  for CuOEP in ZnOEP at 30 K (9.7332 GHz). Uncertainty estimates are 95% confidence intervals from the stretched exponential fit.

Pulse sequence	Paramagnetic concentration	$T_1$ (ms)		% change over 1 to 100 inversion recovery	
		2910 G ( $\parallel$ )	3491 G ( $\perp$ )	2910 G ( $\parallel$ )	3491 G ( $\perp$ )
Inversion recovery	1 to 100	$3.828 \pm 0.008$	$3.870 \pm 0.004$	N/A	N/A
Inversion recovery	1 to 1000	$3.46 \pm 0.04$	$3.555 \pm 0.017$	-9.6%	-8.1%
Saturation recovery	1 to 100	$3.99 \pm 0.05$	$4.23 \pm 0.04$	4.2%	9.3%

**Table S11:** Comparison of concentration and pulse sequence effects on measured  $T_1$  for CuTPP in NiTPP at 100 K (9.7404 GHz). Uncertainty estimates are 95% confidence intervals from the stretched exponential fit.

Pulse sequence	Paramagnetic concentration	$T_1$ ( $\mu$ s)		% change over 1 to 100 inversion recovery	
		2915 G ( $\parallel$ )	3498 G ( $\perp$ )	2915 G ( $\parallel$ )	3498 G ( $\perp$ )
Inversion recovery	1 to 100	3.80 $\pm$ 0.02	0.980 $\pm$ 0.014	N/A	N/A
Inversion recovery	1 to 1000	3.67 $\pm$ 0.07	1.09 $\pm$ 0.02	-3.4%	11.2%
Saturation recovery	1 to 100	4.14 $\pm$ 0.05	0.96 $\pm$ 0.11	8.9%	-2.0%

**Table S12:** Comparison of concentration and pulse sequence effects on measured  $T_1$  for CuTPP in NiTPP at 30 K (9.7404 GHz). Uncertainty estimates are 95% confidence intervals from the stretched exponential fit.

Pulse sequence	Paramagnetic concentration	$T_1$ (ms)		% change over 1 to 100 inversion recovery	
		2915 G ( $\parallel$ )	3498 G ( $\perp$ )	2915 G ( $\parallel$ )	3498 G ( $\perp$ )
Inversion recovery	1 to 100	2.885 $\pm$ 0.007	2.573 $\pm$ 0.005	N/A	N/A
Inversion recovery	1 to 1000	2.83 $\pm$ 0.02	2.559 $\pm$ 0.008	-1.9%	-0.5%
Saturation recovery	1 to 100	3.07 $\pm$ 0.03	2.76 $\pm$ 0.04	6.4%	7.3%

**Table S13:** Relative change in  $T_1$  between the three CuP compounds measured by inversion recovery at 1 to 100 dilutions (primary data presented in **Table S4**) at parallel and perpendicular orientation field positions. Positive values indicate a longer  $T_1$  for the first compound named.

T (K)	CuOEP vs. CuTPP		CuOEP vs. CuTiPP		CuTiPP vs. CuTPP	
	Parallel	Perpendicular	Parallel	Perpendicular	Parallel	Perpendicular
30	32.1%	42.4%	-15.8%	15.3%	41.3%	32.0%
100	44.6%	78.5%	-52.9%	28.2%	63.8%	70.1%

### 3. Computational Methods

#### A. Computational Parameters

All computations were performed in Orca 5.0.3.<sup>16</sup> Density functional theory (DFT) calculations employed the B3LYP functional modified with 38% exact Hartree-Fock exchange added. This calibrates the calculations to match the experimental g-values, in accordance with an established procedure.<sup>17–19</sup> DFT was employed to calculate g-values, vibrational modes, and spin-phonon coupling constants. Numerical frequency calculations with inclusion of the polarizability tensor were employed to calculate non-resonant Raman spectra. Time-dependent density functional theory (TDDFT) calculations were employed to calculate excited state transition energies. All calculations used the RIJCOSX approximation, TIGHTSCF convergence criteria, and DEFGRID3 grid precision. Calculations in sections 3B-3C used the def2-TZVP basis set and def2/J auxiliary basis set for all atoms, SLOWCONV convergence method, and D3BJ dispersion correction. CPCM with an infinite dielectric was used for the Raman calculations to mimic a solid state crystal environment. Calculations in sections 3D-3E used the ZORA relativistic correction and ZORA-def2-TZVP basis set on all atoms.

#### B. Spin-Phonon Coupling

Spin-phonon coupling calculations were conducted according to previously reported methods based on the spin Hamiltonian.<sup>19</sup> Briefly, a frequency calculation is performed to obtain the dimensionless vibrational normal coordinates. The structure is distorted along each dimensionless mode in steps of 0.1 from  $Q = -0.5$  to  $+0.5$ , and the g-values are recalculated at each single point geometry. The slope of the g-values vs.  $Q$  yields the spin-phonon coupling coefficient,  $dg/dQ$ .

Geometry optimization of CuOEP and CuTiPP yielded structures in close agreement with the crystal geometries validated by PXRD (planar and ruffled, respectively), and thus the optimized geometries were used for the calculations for all-positive vibrational frequencies. For CuTPP, the crystal structure features a ruffled geometry, while geometry optimizations led to a planar structure. Thus, the crystal structure was hydrogen-optimized, and the resulting normal modes were used in the spin-phonon coupling calculation. One negative frequency mode was found at  $-6.44 \text{ cm}^{-1}$ , corresponding principally to phenyl substituent rotations and possessing negligible  $dg/dQ$  values – this mode was therefore neglected in the  $T_1$  calculations to avoid problems with thermal weighting. For spin-phonon coupling calculations, modes up to at least  $400 \text{ cm}^{-1}$  were considered in all cases, and higher modes up to  $450 \text{ cm}^{-1}$  if there existed symmetric stretching vibrational modes in this temperature range.

The calculated spin-phonon coupling for the strongest-coupled modes in each of the copper porphyrins is reported in **Table S14**. The frequency and identity of the coupling vibrational mode is also reported, and pictures of these vibrational modes are given **Figures S38-S50**. Each of these vibrations transforms as the totally symmetric irreducible representation  $a_1$  in the appropriate point group. A complete list of calculated spin-phonon coupling parameters is found in **Tables S15-S17**.

**Table S14.** Calculated spin-phonon coupling coefficients for the most strongly coupled vibrational modes. SPC indicates  $dg/dQ$  values averaged over the three principal  $g$ -values. “SymStr” denotes a symmetric stretching mode, while “Ruff” denotes a ruffling mode.

<b>CuOEP</b>			<b>CuTPP</b>			<b>CuTiPP</b>		
ID	$\nu$ (cm <sup>-1</sup> )	log SPC	ID	$\nu$ (cm <sup>-1</sup> )	log SPC	ID	$\nu$ (cm <sup>-1</sup> )	log SPC
SymStr*	200	1.1E-6	Ruff	23	2.7E-7	Ruff	26	1.2E-6
SymStr	281	6.5E-6	Ruff	113	8.8E-7	Ruff	139	1.0E-6
SymStr	369	8.1E-6	SymStr*	204	1.2E-6	SymStr	244	1.0E-6
			SymStr	356	2.5E-6	SymStr	371	7.4E-6
			SymStr	421	2.1E-5	SymStr	398	1.2E-5

\* = Strong mixing with another mode (rotation, saddling, etc.)

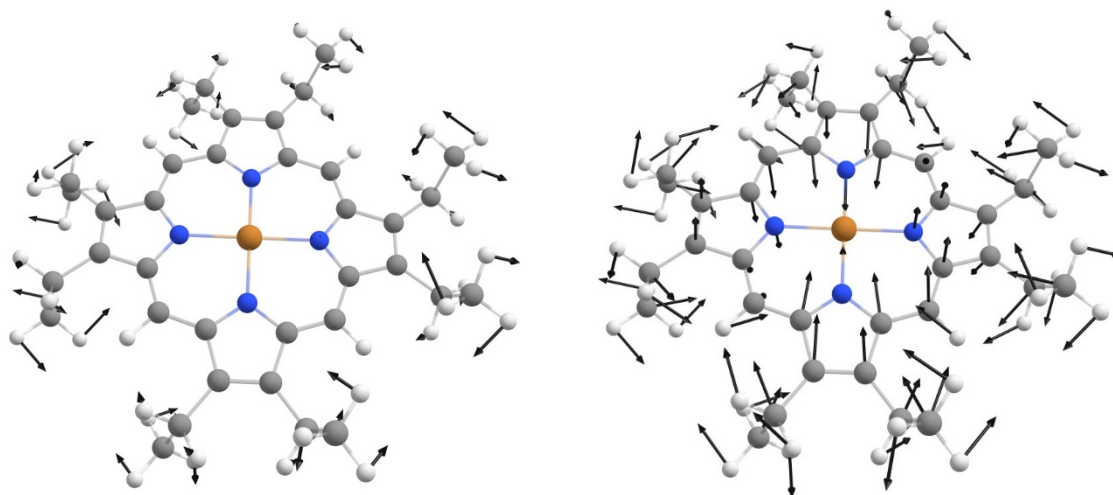


**Figure S38:** 200 cm<sup>-1</sup> mixed symmetric stretching mode for CuOEP. Left: scaled displacement arrows. Right: unscaled displacement arrows.

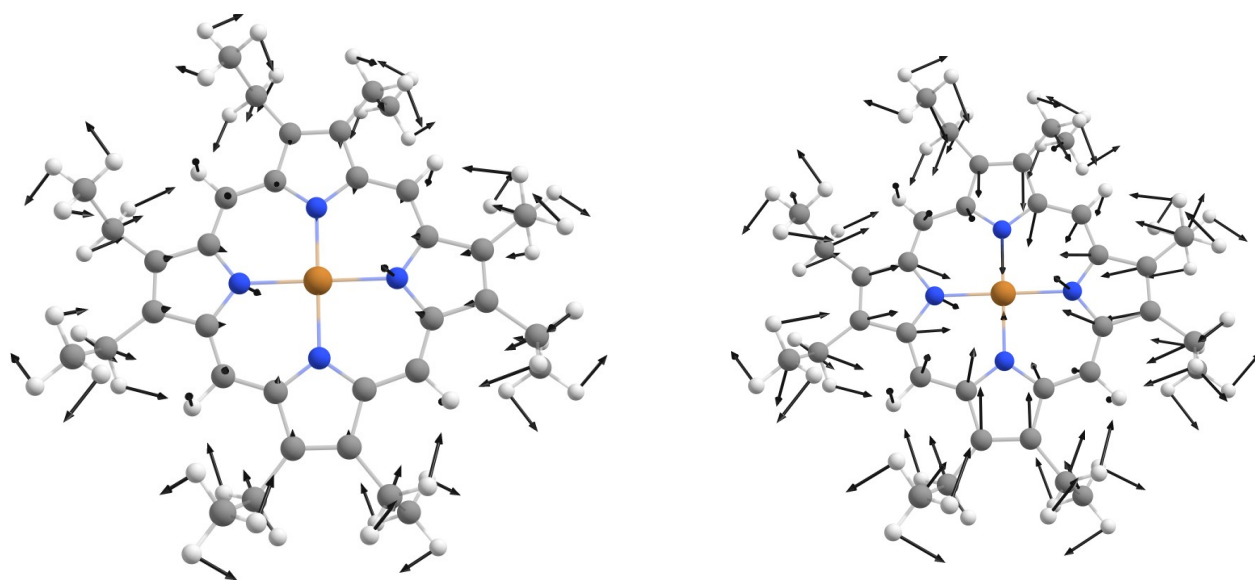


**Figure S39:** 281  $\text{cm}^{-1}$  mixed symmetric stretching mode for CuOEP. Left: scaled displacement arrows. Right: unscaled displacement arrows.

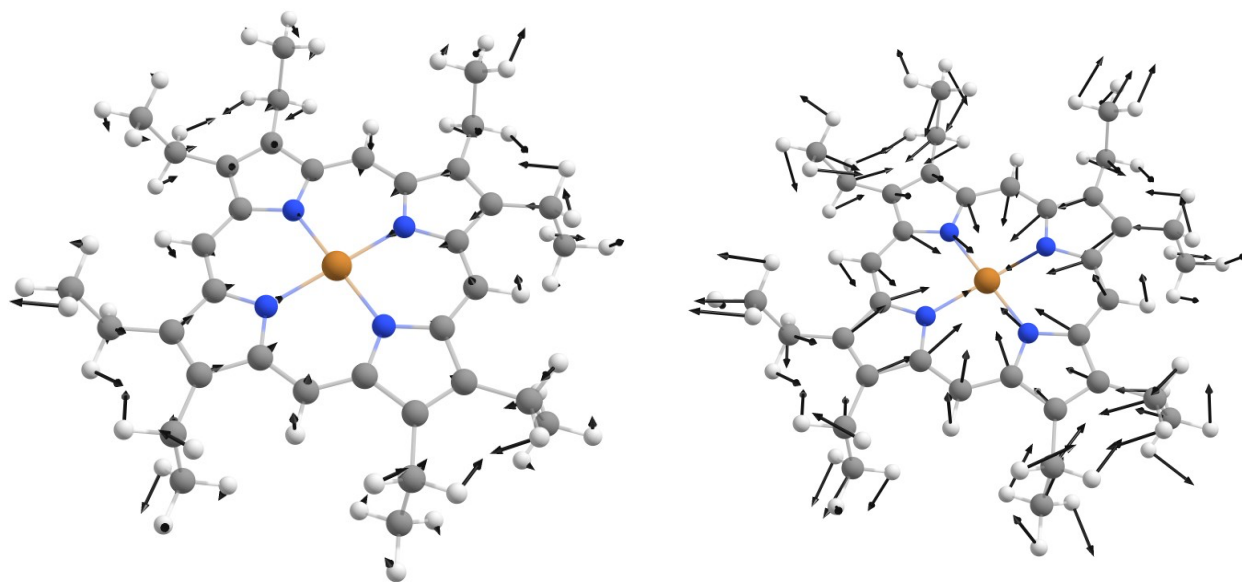


**Figure S40:** 369 cm<sup>-1</sup> symmetric stretching mode for CuOEP. Left: scaled displacement arrows. Right: unscaled displacement arrows.

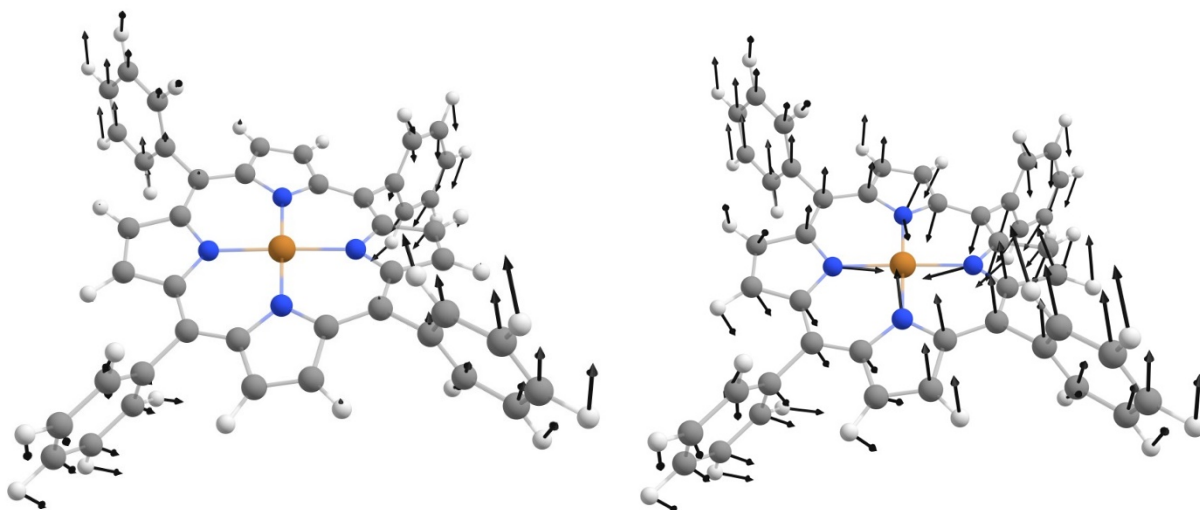


**Figure S41:** 23 cm<sup>-1</sup> ruffling mode for CuTPP. Left: scaled displacement arrows. Right: unscaled displacement arrows.

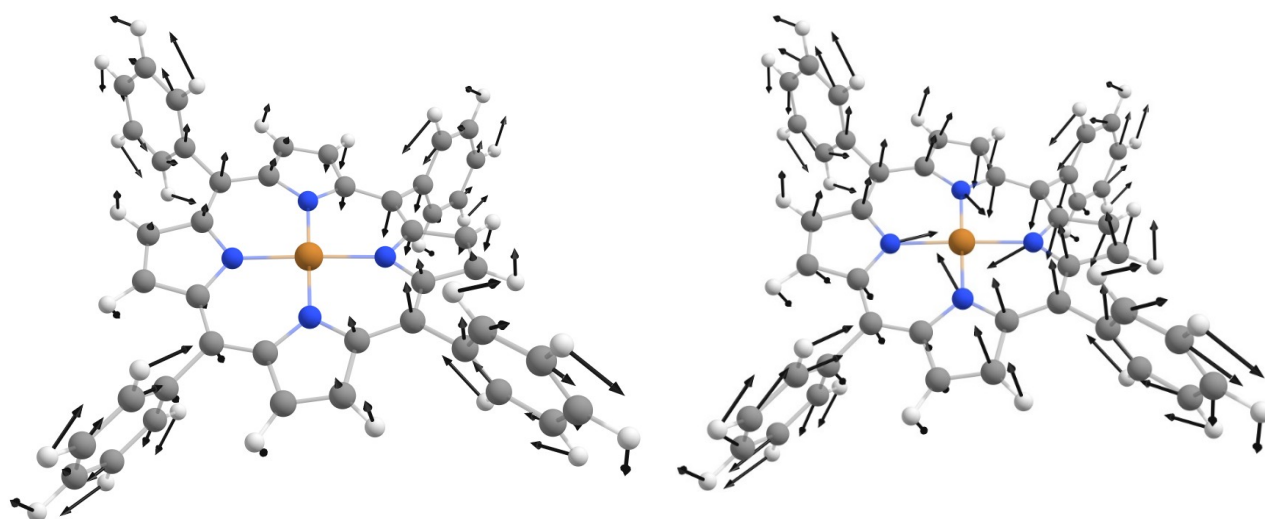


**Figure S42:**  $113\text{ cm}^{-1}$  ruffling mode for CuTPP. Left: scaled displacement arrows. Right: unscaled displacement arrows.

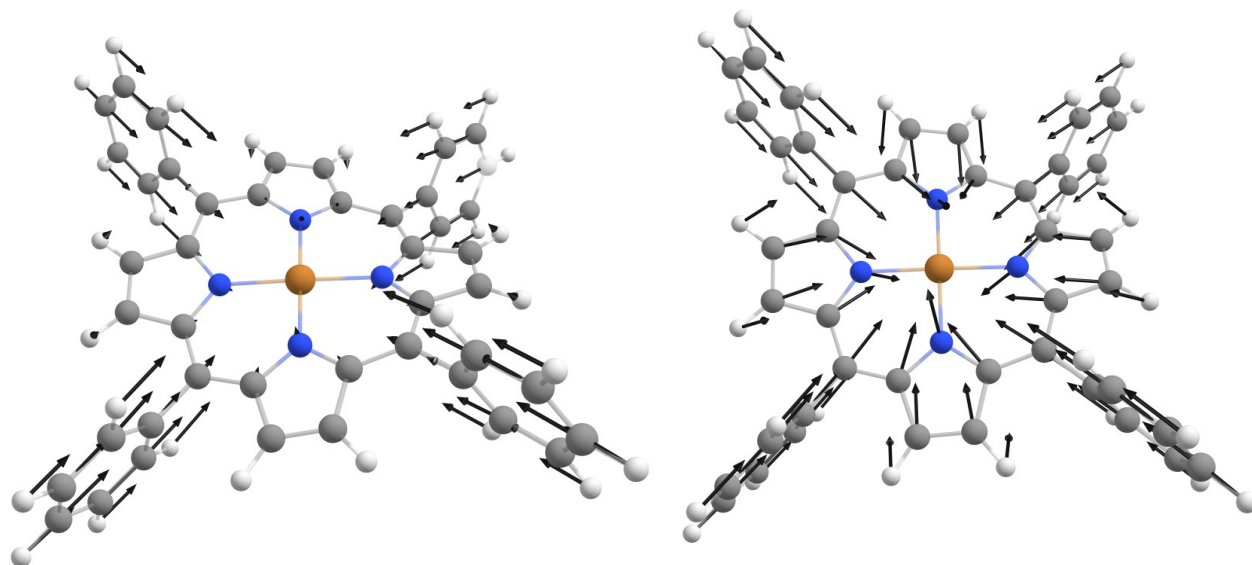


**Figure S43:**  $204\text{ cm}^{-1}$  symmetric stretch mode for CuTPP. Left: scaled displacement arrows. Right: unscaled displacement arrows.

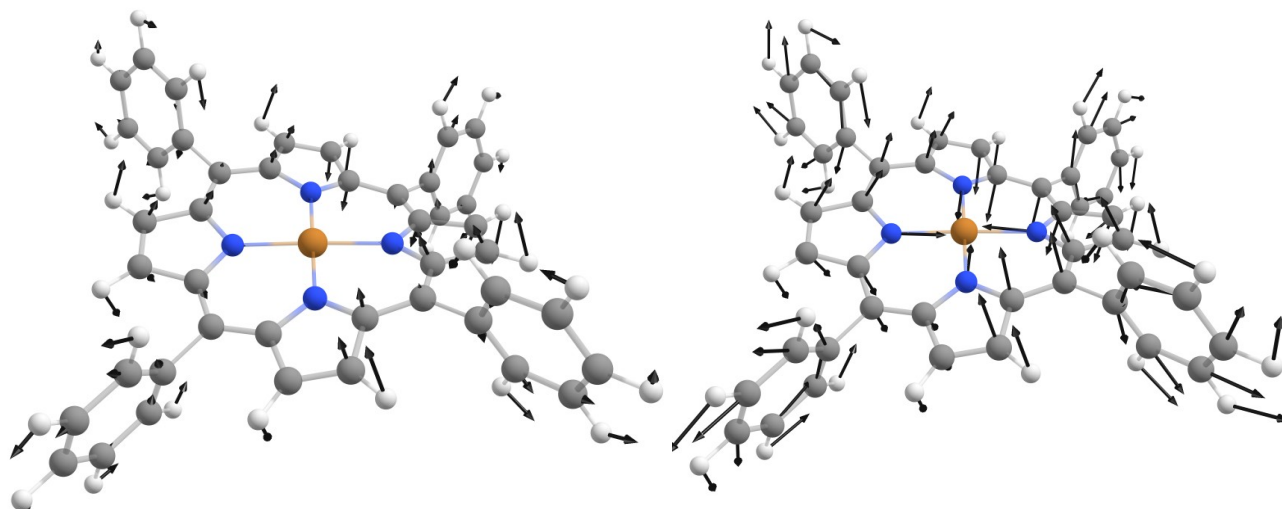


**Figure S44:** 356 cm<sup>-1</sup> symmetric stretch mode for CuTPP. Left: scaled displacement arrows. Right: unscaled displacement arrows.

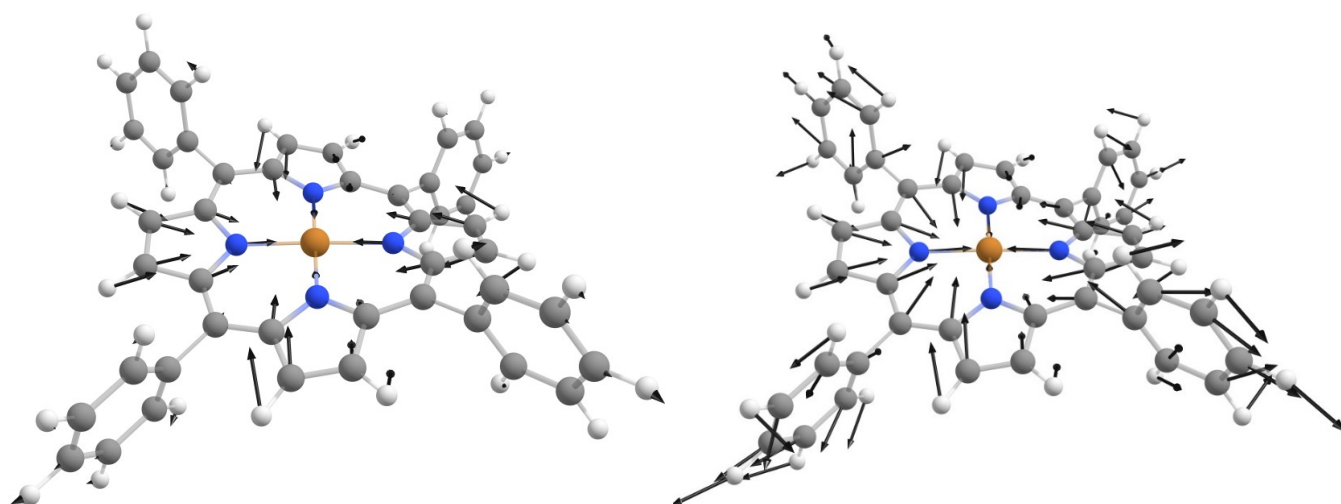


**Figure S45:** 421 cm<sup>-1</sup> symmetric stretch mode for CuTPP. Left: scaled displacement arrows. Right: unscaled displacement arrows.

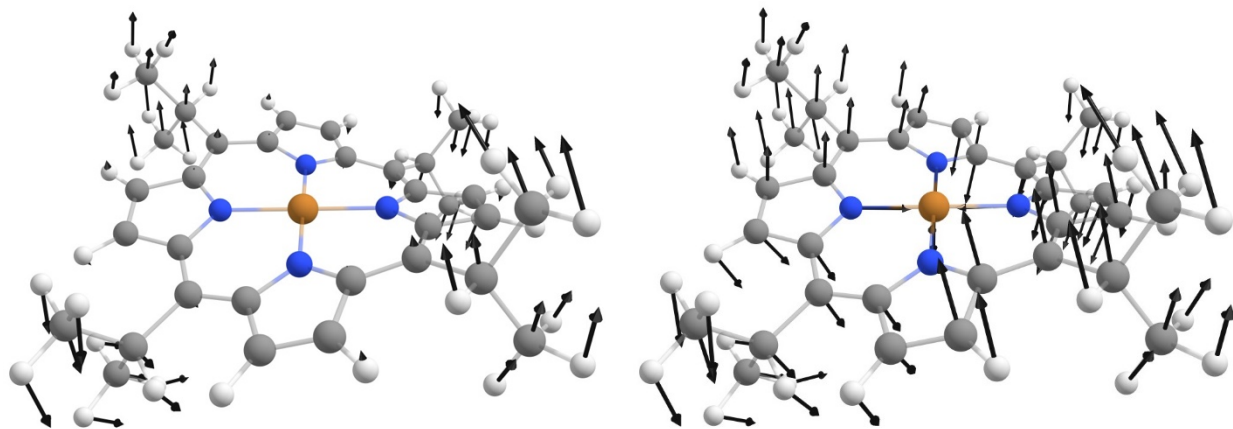


**Figure S46:** 26 cm<sup>-1</sup> ruffling mode for CuTiPP. Left: scaled displacement arrows. Right: unscaled displacement arrows.

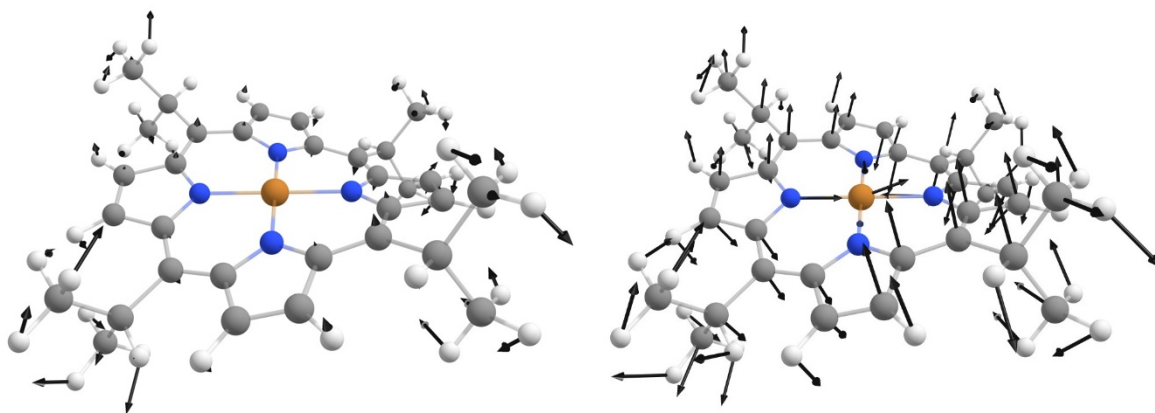


**Figure S47:** 139 cm<sup>-1</sup> ruffling mode for CuTiPP. Left: scaled displacement arrows. Right: unscaled displacement arrows.

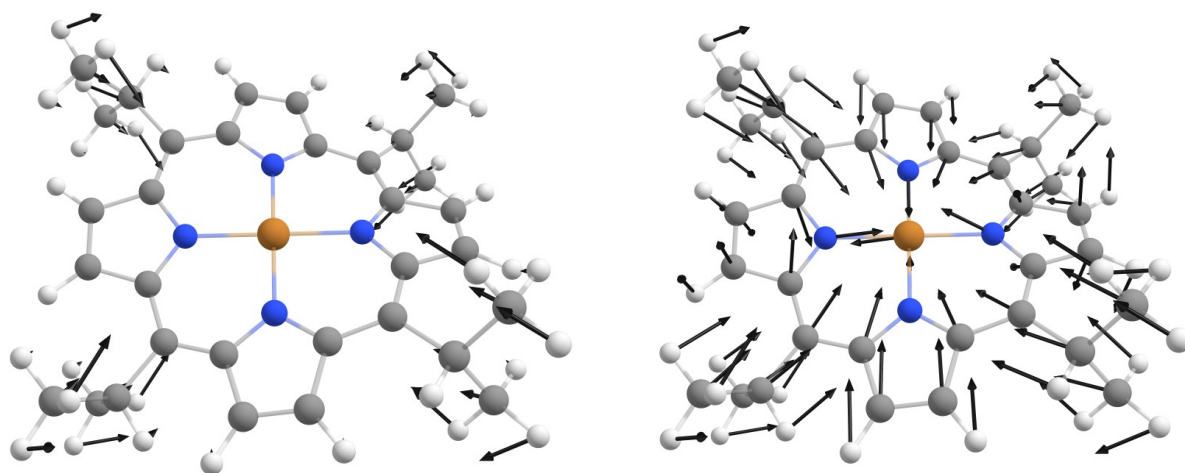


**Figure S48:** 244 cm<sup>-1</sup> symmetric stretch mode for CuTiPP. Left: scaled displacement arrows. Right: unscaled displacement arrows.

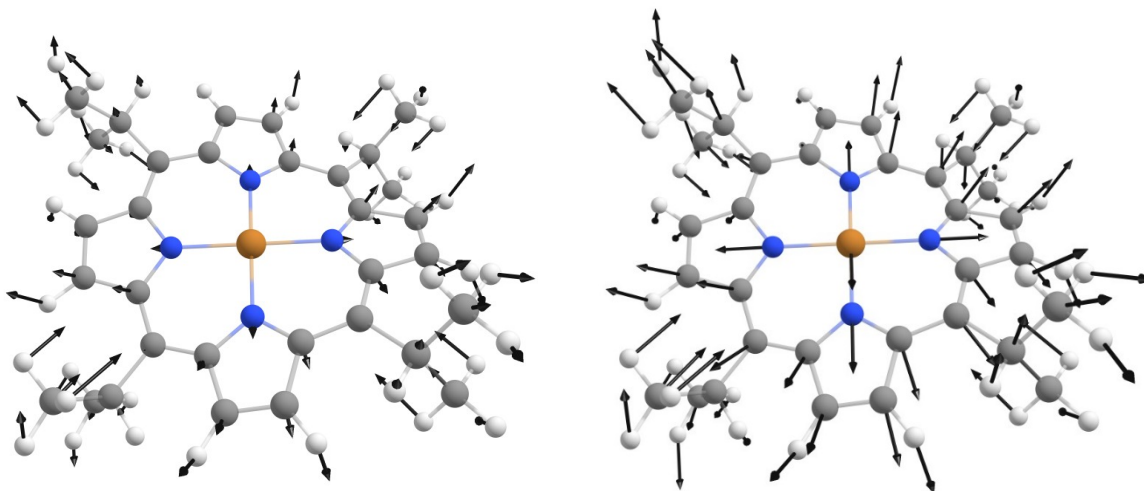


**Figure S49:** 371 cm<sup>-1</sup> symmetric stretch mode for CuTiPP. Left: scaled displacement arrows. Right: unscaled displacement arrows.

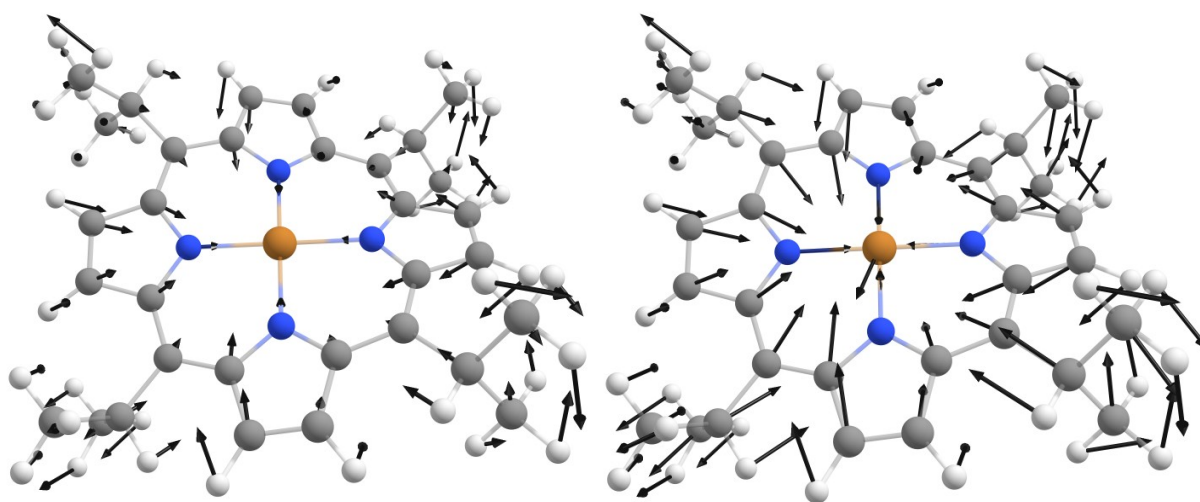


**Figure S50:** 398  $\text{cm}^{-1}$  symmetric stretch mode for CuTiPP. Left: scaled displacement arrows. Right: unscaled displacement arrows.

**Table S15.** Calculated spin-phonon coupling coefficients for all thermally-accessible modes in CuOEP. Character of prominent vibrational modes indicated.

Mode #	Energy ( $\text{cm}^{-1}$ )	dg/dQ	Mode type ( $D_{4h}$ )
1	19.9	0	
2	26.25	4.17E-13	Ruffling ( $b_{1u}$ )
3	39.18	4.17E-13	
4	47.05	3.89E-10	
5	47.31	3.24E-09	Mixed waving + stretching ( $a_{1g}$ )
6	54.59	8.33E-14	
7	56.82	8.33E-14	
8	57.51	1.83E-11	
9	59.33	0	
10	63.77	1.32E-08	Mixed waving + stretching ( $a_{1g}$ )
11	65.03	2.26E-10	
12	67.43	8.33E-14	
13	73.36	3.49E-08	Mixed waving + stretching ( $a_{1g}$ )
14	74.8	4.17E-13	
15	84.88	1.71E-11	
16	87.83	2.40E-08	Mixed waving + stretching ( $a_{1g}$ )
17	110.16	8.33E-14	
18	138.64	1.67E-13	
19	141.87	1.17E-12	
20	152.5	9.96E-07	Antisymmetric stretch ( $b_{1g}$ )
21	153.28	1.74E-09	Scissoring ( $b_{2g}$ )
22	160.19	3.33E-13	
23	164.27	8.33E-13	

24	174.94	2.32E-11	
25	199.64	1.12E-06	Mixed waving + stretching ( $a_{1g}$ )
26	202.58	8.33E-14	
27	203.51	1.13E-07	Mixed waving + stretching ( $a_{1g}$ )
28	204.65	4.17E-13	
29	206.35	9.26E-10	
30	209.95	2.87E-09	
31	210.98	1.20E-06	Antisymmetric stretch ( $b_{1g}$ )
32	218.86	1.32E-06	Mixed stretching + waving ( $a_{1g}$ )
33	219.46	9.17E-13	
34	229.46	3.42E-12	
35	234.5	3.42E-12	
36	235.97	5.17E-12	
37	238.48	8.33E-13	
38	238.62	7.08E-12	
39	256.19	3.12E-11	
40	272.83	1.67E-13	
41	280.67	6.51E-06	Ligand symmetric stretch ( $a_{1g}$ )
42	285.13	5.00E-13	
43	291.78	3.98E-11	
44	308.21	5.00E-13	
45	311.96	3.42E-12	
46	316.7	4.30E-09	
47	323.59	4.17E-13	
48	329.28	1.72E-07	Mixed stretching + waving ( $a_{1g}$ )
49	329.47	2.06E-08	
50	345.98	6.67E-13	
51	349.13	2.50E-12	
52	358.33	0	
53	369.11	8.12E-06	Cu-N <sub>4</sub> symmetric stretch ( $a_{1g}$ )
54	449.24	4.17E-13	
55	459.26	4.17E-13	
56	476.7	1.26E-06	Mixed stretching + waving ( $a_{1g}$ )

**Table S16.** Calculated spin-phonon coupling coefficients for all thermally-accessible modes in CuTPP. Character of prominent vibrational modes indicated.

Mode #	Energy (cm <sup>-1</sup> )	dg/dQ	Mode type ( $D_{2d}$ )
2	6.68	4.17E-13	
3	6.7	0	
4	10.25	5.46E-09	
5	22.57	2.73E-07	Ruffling ( $a_1$ )
6	36.42	1.22E-11	
7	50.75	4.17E-13	
8	50.75	3.33E-13	
9	52.93	6.27E-09	
10	59.12	2.15E-08	
11	59.58	0	

12	59.58	4.17E-13	
13	90.6	5.40E-09	
14	109.45	1.37E-08	
15	112.78	8.81E-07	Ruffling ( $a_1$ )
16	138.04	8.25E-09	
17	145.61	8.33E-14	
18	145.61	8.33E-14	
19	203.91	1.17E-06	Symmetric stretch ( $a_1$ )
20	204.98	1.55E-08	
21	218.64	3.33E-13	
22	218.64	3.33E-13	
23	230.01	1.67E-13	
24	230.01	8.33E-14	
25	230.76	1.69E-07	
26	231.52	3.04E-06	Antisymmetric stretch ( $b_1$ )
27	243.34	1.67E-13	
28	243.34	8.33E-14	
29	249.3	2.26E-08	
30	273.23	1.49E-07	
31	290.76	1.74E-08	
32	308.01	0	
33	308.01	1.67E-13	
34	308.95	3.31E-10	
35	341.14	0	
36	341.14	8.33E-14	
37	355.55	2.46E-06	Ruffling + symmetric stretch ( $a_1$ )
38	421.36	2.07E-05	Cu-N <sub>4</sub> symmetric stretch ( $a_1$ )
39	427.24	6.50E-09	
40	433.29	8.33E-14	
41	433.29	8.33E-14	

**Table S17.** Calculated spin-phonon coupling coefficients for all thermally-accessible modes in CuTiPP. Character of prominent vibrational modes indicated.

Mode #	Energy (cm <sup>-1</sup> )	dg/dQ	Mode type ( $D_{2d}$ )
1	25.18	4.42E-10	
2	26.09	1.16E-06	Ruffling ( $a_1$ )
3	47.2	3.84E-11	
4	53.96	2.42E-12	
5	56.07	6.00E-12	
6	77	0	
7	84.91	2.62E-10	
8	88.45	2.50E-07	Ruffling ( $a_1$ )
9	96.75	1.64E-11	
10	121.61	2.16E-10	
11	135.31	4.30E-10	
12	138.62	1.03E-06	Ruffling ( $a_1$ )
13	163.07	1.82E-08	

14	163.32	1.77E-07	
15	164.08	1.64E-10	
16	167.93	9.11E-11	
17	179.3	2.42E-12	
18	188.88	1.17E-12	
19	202.75	3.83E-12	
20	203.26	4.69E-09	
21	204.16	9.37E-11	
22	206.09	1.77E-11	
23	207.11	1.94E-10	
24	208.36	1.10E-08	
25	222.85	3.82E-10	
26	224.06	3.45E-06	Antisymmetric stretch ( $b_1$ )
27	228.37	1.85E-10	
28	229.35	6.38E-11	
29	239.79	6.15E-11	
30	244.01	1.01E-06	Ligand symmetric stretch ( $a_1$ )
31	251.13	5.49E-11	
32	254.87	8.33E-14	
33	256.17	2.42E-10	
34	272.12	1.82E-11	
35	296.83	6.67E-13	
36	297.21	2.25E-12	
37	302.89	3.82E-11	
38	304.7	1.77E-08	
39	344.32	5.00E-13	
40	347.27	1.67E-13	
41	363.88	9.52E-11	
42	370.89	7.39E-06	Symmetric stretch + ruffling ( $a_1$ )
43	397.96	1.18E-05	Cu-N <sub>4</sub> symmetric stretch ( $a_1$ )
44	400.16	7.60E-10	
45	404.72	2.10E-10	
46	429.42	2.17E-12	

Overlaid plots of the calculated vs. experimental  $T_1$  values are given in **Figure S51**. The thermally-weighted contributions of each vibrational mode to the calculated  $T_1$  were given for CuOEP and CuTiPP in **Figure 4B-C**. The contributions for CuTPP are given in **Figure S52** for completion, and the log-log slope is given in **Figure S53**. The mode contributions and log-log slope follow very similar trends to those of CuTiPP, indicating a single low-energy ruffling mode that dominates the predicted spin relaxation. The % contributions of each mode to  $T_1$  at any given temperature are displayed for all three CuP compounds in **Figure S54**, and the log-log slope plots are overlaid in **Figure S55**.

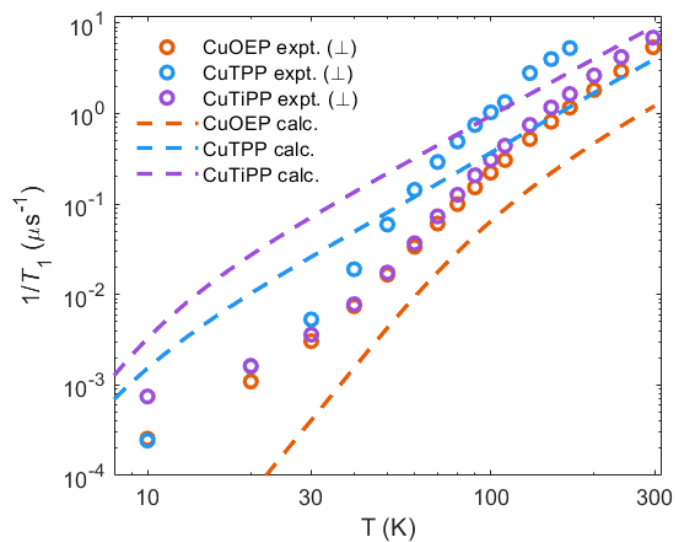


**Figure S51.** Overlay of experimental vs. calculated  $1/T_1$  values as a function of temperature. Data is taken from Figures 3B and 4A in the main text.

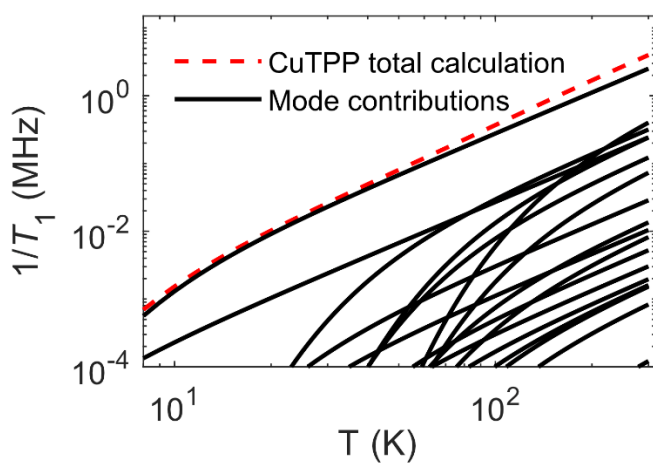


**Figure S52.** Thermally-weighted mode contributions to  $T_1$  for CuTPP according to spin-phonon coupling calculations.

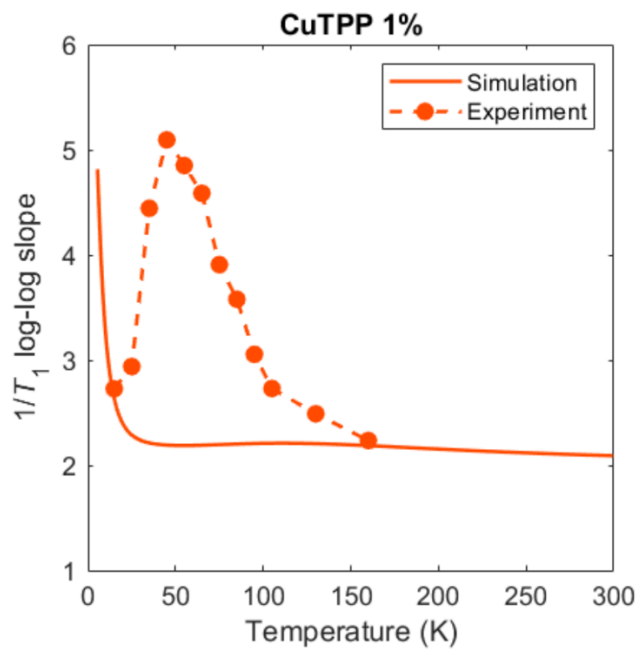


**Figure S53.** Log-log slope of CuTPP  $T_1$  vs. T for spin-phonon coupling calculation vs. experiment.

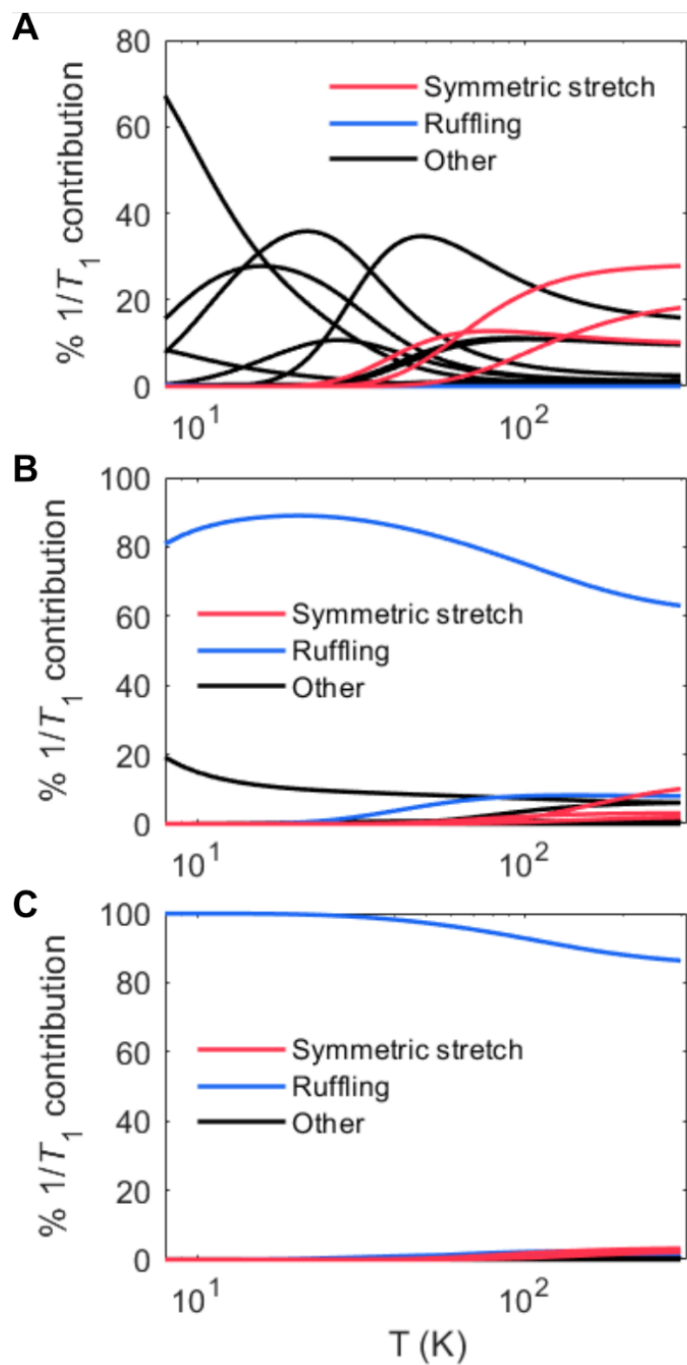


**Figure S54.** Percentage contributions of each vibrational mode to the total  $1/T_1$  at different temperatures, according to spin-phonon coupling calculations. (A) CuOEP, (B) CuTPP, (C) CuTiPP.

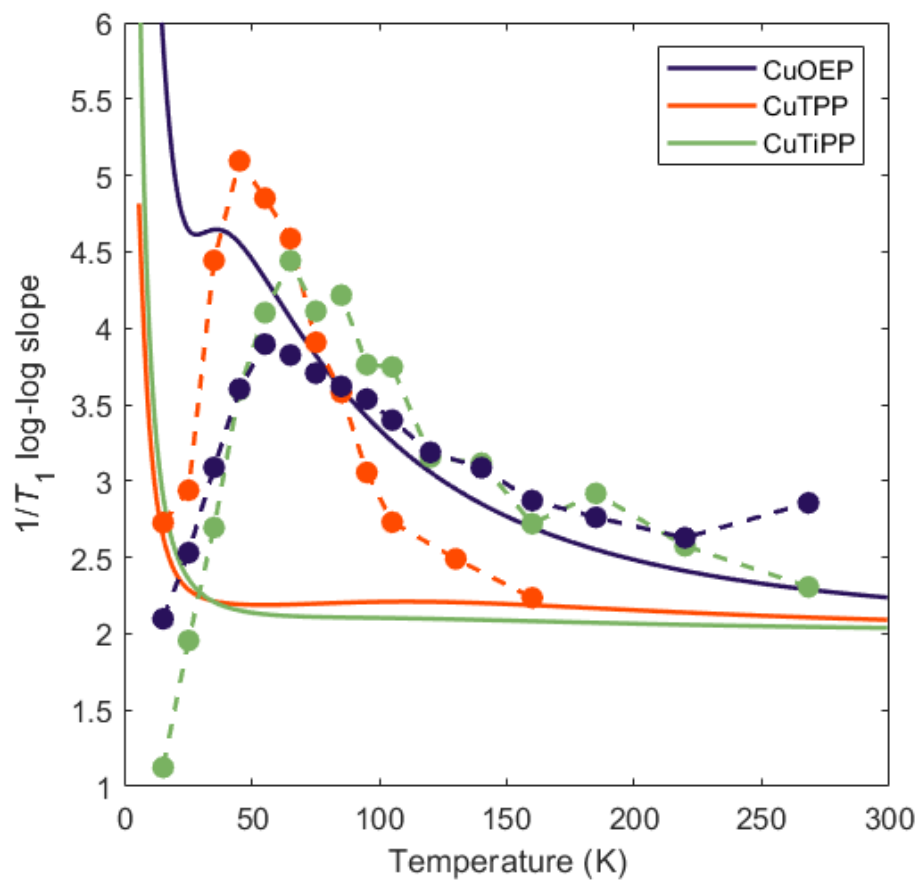


**Figure S55.** Overlay of experimental (dashed lines, markers) and simulated (solid lines) log-log  $1/T_1$  slopes for all three CuP compounds. CuOEP displays qualitative agreement between experiment and simulation, while CuTPP and CuTiPP do not. Good agreement below 20 K is not owing to neglect of the direct process in the simulation.

### C. Raman Spectra Calculations

The calculated Raman spectra are given in **Tables S18 – S21**, together with assignments for the four main Raman peaks observed in the experimental resonance Raman spectra (**Figure 6**). Pictures of the four modes used in the computational assignments are given in **Figures S56-71**. Since the crystal and optimized geometries of CuTPP are different (ruffled and planar, respectively), two Raman calculations were conducted using the H-optimized crystal structure and the fully optimized planar structure. The H-optimized (ruffled) calculation predicts four intense, polarized bands below 450  $\text{cm}^{-1}$ . The fully-optimized (planar) calculation predicts only three such bands, with the 349  $\text{cm}^{-1}$  mode possessing vanishing intensity as the geometry approaches exact planarity. Experimentally, we find four modes below 450  $\text{cm}^{-1}$  in the CuTPP solid-state Raman, agreeing with the crystal structure as expected. However, solution-phase rR spectra also show four modes, indicating that the computationally optimized planar structure may not accurately represent the solution phase geometry. We note that the 337  $\text{cm}^{-1}$  peak has lower intensity in the solution phase experimental rR spectra than in the solid state rR spectra. This suggests that CuTPP tends closer to planarity in solution than in the solid state, but conformational fluctuations or solvation energetics produce on average at least a small degree of ruffling in solution as well.

**Table S18.** Calculated Raman spectrum below 900  $\text{cm}^{-1}$  for the CuOEP optimized geometry. Modes assigned to key vibrations in the experimental resonance Raman spectra are bolded and highlighted.

Mode	freq ( $\text{cm}^{-1}$ )	Activity	Depolarization
6:	20.05	0.000032	0.744725
7:	25.56	0.000078	0.294651
8:	37.88	0.001264	0.716659
9:	46.23	3.863375	0.744919
10:	47.12	3.079327	0.679964
11:	50.67	0.000566	0.737213
12:	51.95	0.172543	0.718700
13:	56.01	0.001134	0.718016
14:	57.62	0.002797	0.745366
15:	62.47	8.515585	0.709833
16:	64.90	0.204946	0.690724
17:	65.63	0.011937	0.664568
18:	80.27	16.327562	0.643549
19:	86.56	26.111809	0.749967
20:	90.47	0.004296	0.716879
21:	98.92	13.909953	0.742695
22:	113.64	0.000533	0.640078

23:	140.24	0.000210	0.740544
24:	142.49	0.000372	0.739545
25:	152.63	17.390857	0.749546
26:	153.85	21.205669	0.749077
27:	159.96	0.002617	0.749439
28:	164.64	0.004028	0.732950
29:	176.63	4.174910	0.749274
30:	203.34	20.969024	0.095241
31:	208.31	4.995895	0.749831
32:	209.18	0.002998	0.618288
33:	210.07	18.449229	0.749588
34:	210.25	0.043434	0.738261
35:	212.56	5.156121	0.746708
36:	214.81	5.394393	0.697175
37:	220.66	0.000526	0.082449
<b>38:</b>	<b>221.55</b>	<b>26.753313</b>	<b>0.139939</b>
39:	229.94	0.008010	0.749343
40:	235.02	0.001788	0.702028
41:	237.56	0.000365	0.355352
42:	242.03	24.555776	0.749840
43:	242.23	0.654846	0.749765
44:	256.34	21.581391	0.749938
45:	271.02	0.000210	0.576098
<b>46:</b>	<b>280.60</b>	<b>97.556178</b>	<b>0.094759</b>
47:	282.64	0.005988	0.056761
48:	293.08	1.499940	0.724337
49:	308.71	0.006823	0.433002
50:	312.03	0.000341	0.667669
51:	317.31	25.985655	0.424222
52:	322.51	0.003439	0.125502
53:	329.98	7.151342	0.608529
<b>54:</b>	<b>331.09</b>	<b>32.901800</b>	<b>0.331444</b>
55:	346.44	0.000169	0.190264
56:	348.83	0.000097	0.420130
57:	358.43	0.000636	0.214317
<b>58:</b>	<b>369.53</b>	<b>181.454995</b>	<b>0.080114</b>
59:	449.49	10.523894	0.749808
60:	459.76	0.000071	0.319846
61:	478.16	11.459696	0.577672
62:	488.56	0.000352	0.369228
63:	492.75	0.000227	0.223688
64:	514.02	4.301608	0.749915
65:	541.53	0.000282	0.652037
66:	554.56	0.000210	0.484970
67:	570.90	0.034659	0.631478
68:	573.76	9.905413	0.608030

69:	594.05	12.521958	0.749698
70:	600.32	0.000534	0.405159
71:	613.04	0.182620	0.734883
72:	629.91	0.000154	0.653827
73:	642.09	0.000191	0.698099
74:	682.83	15.662480	0.749443
75:	696.51	193.796919	0.149790
76:	703.29	38.561115	0.191116
77:	723.04	0.000502	0.258268
78:	725.46	0.000180	0.453337
79:	759.62	0.000085	0.482690
80:	774.27	10.803796	0.743233
81:	774.63	48.279016	0.148865
82:	775.47	0.004784	0.149940
83:	778.33	0.000401	0.143245
84:	784.92	0.001061	0.237838
85:	786.81	185.697990	0.073811
86:	790.58	0.174060	0.576649
87:	791.73	359.670272	0.678667
88:	791.85	9.649457	0.700516
89:	796.62	0.000350	0.663796
90:	801.94	85.779404	0.315266
91:	810.33	0.044457	0.720499
92:	810.53	0.004430	0.686639
93:	812.15	120.697248	0.729210
94:	816.74	1.130754	0.724504
95:	831.92	200.380067	0.063716
96:	848.77	1.005125	0.740420
97:	860.68	0.000128	0.656490
98:	860.79	0.000297	0.258543

**Table S19.** Calculated Raman spectrum below 900  $\text{cm}^{-1}$  for the H-optimized CuTPP crystal geometry. Modes assigned to key vibrations in the experimental resonance Raman spectra are bolded and highlighted.

Mode	freq ( $\text{cm}^{-1}$ )	Activity	Depolarization
10:	20.82	2.243221	0.683623
11:	33.78	1.192430	0.749995
12:	49.83	29.980044	0.750000
13:	49.91	29.905034	0.749998
14:	52.95	27.322976	0.750000
15:	58.76	10.214164	0.189477
16:	59.44	14.714737	0.749867
17:	59.45	14.610520	0.747901

18:	89.61	0.098351	0.664012
19:	106.50	13.773032	0.749999
20:	110.70	11.047586	0.582267
21:	136.47	15.461224	0.749999
22:	143.59	0.439359	0.749999
23:	143.67	0.447465	0.749945
24:	201.26	2.267712	0.749824
<b>25:</b>	<b>203.89</b>	<b>68.967058</b>	<b>0.072262</b>
26:	217.91	0.431442	0.749663
27:	217.96	0.445036	0.749946
28:	228.97	0.078240	0.749783
29:	229.07	0.077565	0.726982
<b>30:</b>	<b>231.27</b>	<b>40.599067</b>	<b>0.087013</b>
31:	231.84	106.024030	0.749341
32:	242.07	1.323861	0.749999
33:	242.09	1.303593	0.749995
34:	248.16	44.722308	0.749999
35:	268.26	5.122585	0.750000
36:	289.75	0.284904	0.630427
37:	307.14	0.299043	0.749924
38:	307.19	0.314943	0.749956
39:	308.79	8.833660	0.749999
40:	340.39	7.167111	0.749996
41:	340.48	7.158863	0.750000
<b>42:</b>	<b>354.61</b>	<b>94.223469</b>	<b>0.185958</b>
<b>43:</b>	<b>420.10</b>	<b>404.582810</b>	<b>0.077728</b>
44:	425.90	17.875836	0.749868
45:	432.39	3.369166	0.749896
46:	432.43	3.470448	0.749810
47:	434.87	24.310742	0.749623
48:	435.13	0.705117	0.695456
49:	435.13	0.722097	0.710758
50:	435.20	13.317819	0.110865
51:	460.46	18.314646	0.749833
52:	465.12	0.145049	0.749768
53:	465.28	0.148080	0.749673
54:	475.84	0.626299	0.009106
55:	530.39	48.467177	0.749999
56:	553.74	1.438662	0.749986
57:	553.78	1.416866	0.750000
58:	582.28	11.569410	0.063290
59:	592.95	5.966154	0.005366
60:	596.56	18.268118	0.749976
61:	596.60	18.328006	0.749994
62:	606.62	3.733946	0.749991
63:	652.72	10.371547	0.497476

64:	653.31	15.852315	0.749969
65:	653.36	15.756422	0.749977
66:	654.63	3.233272	0.749844
67:	668.68	39.954883	0.013700
68:	694.95	0.501165	0.749995
69:	694.99	0.520679	0.749982
70:	696.69	22.956839	0.125087
71:	707.47	16.757055	0.749991
72:	707.50	16.717930	0.750000
73:	713.41	1.324925	0.749884
74:	716.65	87.772291	0.750000
75:	737.75	0.997407	0.749986
76:	738.35	0.022621	0.749992
77:	738.36	0.023295	0.749981
78:	738.63	0.000968	0.212647
79:	763.87	28.928687	0.749978
80:	773.11	7.004371	0.749990
81:	773.16	6.981080	0.749991
82:	780.28	109.120687	0.750000
83:	790.83	6.140426	0.749977
84:	790.87	6.107544	0.749996
85:	794.12	3.616295	0.087378
86:	809.37	2.323780	0.749997
87:	837.17	0.026987	0.745131
88:	849.57	14.183012	0.749998
89:	849.63	14.081794	0.750000
90:	856.98	1.238388	0.749730
91:	869.46	2.785747	0.048546
92:	872.75	9.959744	0.749821
93:	872.88	9.887305	0.749998
94:	889.49	23.448730	0.749703
95:	889.60	43.101767	0.268993
96:	889.63	8.305552	0.697140
97:	889.63	7.887513	0.733002
98:	898.66	3.821831	0.749933

**Table S20.** Calculated Raman spectrum below 900 cm<sup>-1</sup> for the fully-optimized CuTPP geometry. Modes assigned to key vibrations in the experimental resonance Raman spectra are bolded and highlighted.

Mode	freq (cm <sup>**</sup> -1)	Activity	Depolarization
6:	10.78	0.001830	0.088066
7:	26.41	34.616895	0.446555
8:	28.33	0.754151	0.749753
9:	33.37	11.636755	0.749981

10:	34.04	11.342475	0.746201
11:	36.52	12.229656	0.748051
12:	47.17	27.663222	0.750000
13:	48.66	47.788395	0.750000
14:	48.72	48.181743	0.750000
15:	52.80	7.930715	0.749995
16:	52.81	7.866835	0.749992
17:	60.28	46.912770	0.290764
18:	81.61	0.002757	0.135895
19:	98.76	0.001214	0.021931
20:	104.75	2.000113	0.749998
21:	127.31	25.939590	0.749997
22:	140.79	0.082209	0.749936
23:	140.80	0.081588	0.749993
24:	202.81	0.846572	0.748457
<b>25:</b>	<b>204.49</b>	<b>81.408172</b>	<b>0.077895</b>
26:	217.02	111.800338	0.749996
27:	221.65	0.079151	0.749848
28:	221.69	0.080951	0.749994
29:	225.50	0.530195	0.749916
30:	225.54	0.559017	0.749981
<b>31:</b>	<b>230.01</b>	<b>49.542601</b>	<b>0.101372</b>
32:	233.99	2.246311	0.749861
33:	234.28	2.241091	0.749957
34:	247.68	39.876375	0.749999
35:	266.80	6.480008	0.749999
36:	293.65	0.002962	0.261680
37:	294.96	0.457174	0.749979
38:	295.43	0.449621	0.749994
39:	296.57	11.355296	0.749997
40:	332.73	10.910376	0.749999
41:	332.74	10.893042	0.749998
<b>42:</b>	<b>348.74</b>	<b>0.014069</b>	<b>0.322277</b>
<b>43:</b>	<b>401.36</b>	<b>501.376184</b>	<b>0.099385</b>
44:	420.32	0.369077	0.749250
45:	420.40	0.374778	0.749984
46:	426.96	59.270955	0.749550
47:	427.55	4.744851	0.700887
48:	427.70	0.264170	0.379795
49:	427.74	12.464527	0.153262
50:	427.90	16.359088	0.167466
51:	465.64	16.724952	0.750000
52:	465.78	0.010880	0.749295
53:	465.81	0.024355	0.747161
54:	477.16	0.002263	0.322296
55:	531.22	42.584945	0.750000

56:	555.88	0.001301	0.743972
57:	555.95	0.001363	0.691289
58:	578.77	0.000901	0.079166
59:	590.55	21.556072	0.750000
60:	590.56	21.502085	0.750000
61:	590.85	0.003241	0.585669
62:	598.89	1.094175	0.749993
63:	651.59	0.017669	0.735150
64:	652.15	18.076191	0.750000
65:	652.16	18.116726	0.750000
66:	653.07	3.646721	0.749999
67:	670.33	46.998425	0.007790
68:	693.90	63.947868	0.146128
69:	696.71	1.309152	0.749603
70:	696.72	1.309647	0.749829
71:	704.84	13.542800	0.749999
72:	704.85	13.556568	0.749996
73:	714.09	29.912269	0.749999
74:	716.72	98.340447	0.750000
75:	737.68	1.567188	0.749988
76:	738.43	0.112959	0.749999
77:	738.54	0.108776	0.749880
78:	738.90	0.027033	0.746113
79:	763.83	13.446732	0.749998
80:	776.45	3.549330	0.749991
81:	776.48	3.540434	0.749998
82:	783.47	98.302619	0.750000
83:	788.46	0.003860	0.164735
84:	792.80	6.503599	0.750000
85:	792.82	6.509198	0.749998
86:	807.17	0.001281	0.526122
87:	839.45	0.415028	0.014528
88:	850.43	10.174660	0.749998
89:	850.43	10.170233	0.749999
90:	858.18	0.418308	0.749966
91:	873.41	0.007221	0.072860
92:	875.28	0.052847	0.748617
93:	875.32	0.053857	0.739651
94:	892.20	66.480833	0.295712
95:	892.23	34.165668	0.746671
96:	892.25	5.021601	0.637199
97:	892.51	30.428517	0.454153
98:	897.30	0.677658	0.747520

**Table S21.** Calculated Raman spectrum below 900 cm<sup>-1</sup> for the fully-optimized CuTiPP geometry. Modes assigned to key vibrations in the experimental resonance Raman spectra are bolded and highlighted.

Mode	freq (cm <sup>-1</sup> )	Activity	Depolarization
6:	28.12	3.243647	0.736011
7:	30.41	0.004651	0.737687
8:	46.17	1.678658	0.749992
9:	57.74	10.008328	0.749999
10:	58.04	11.410623	0.749997
11:	76.19	17.320705	0.750000
12:	87.41	1.044936	0.474343
13:	88.26	5.280118	0.748330
14:	96.80	3.866685	0.749968
15:	117.46	8.400529	0.749966
16:	134.81	4.129842	0.740563
17:	139.42	22.092410	0.454684
18:	162.12	6.791170	0.397775
19:	162.45	6.473260	0.605876
20:	164.79	31.832676	0.749934
21:	166.01	1.385878	0.746825
22:	181.21	10.119307	0.749978
23:	191.49	0.534965	0.749487
24:	207.39	1.208951	0.268027
25:	208.09	2.568481	0.252736
26:	209.67	4.246451	0.660774
27:	210.58	8.203097	0.731253
28:	213.08	0.620791	0.749953
29:	214.44	3.148848	0.737731
30:	222.05	0.018357	0.747576
<b>31:</b>	<b>225.53</b>	<b>87.898376</b>	<b>0.738883</b>
32:	227.19	0.091363	0.633205
33:	228.04	0.012313	0.563204
34:	240.80	0.586049	0.747906
<b>35:</b>	<b>243.45</b>	<b>105.858572</b>	<b>0.071894</b>
36:	249.74	0.111567	0.241434
37:	250.38	1.419047	0.746177
38:	253.79	0.687015	0.749805
39:	270.05	0.886168	0.749009
40:	295.25	4.392687	0.749978
41:	297.56	0.031562	0.743996

42:	303.11	0.521134	0.744372
43:	307.43	2.158839	0.371588
44:	343.09	2.777016	0.749868
45:	348.00	3.510900	0.749998
46:	363.58	1.647555	0.646816
<b>47:</b>	<b>369.40</b>	<b>229.087515</b>	<b>0.113409</b>
48:	399.05	0.136751	0.408541
<b>49:</b>	<b>399.74</b>	<b>206.099535</b>	<b>0.044498</b>
50:	404.61	1.702973	0.746464
51:	429.48	25.496664	0.749981
52:	436.11	3.661245	0.748633
53:	440.09	1.574898	0.749978
54:	454.19	2.402529	0.749964
55:	459.68	13.248315	0.372694
56:	481.51	22.895008	0.749997
57:	520.40	0.028818	0.689624
58:	541.50	8.202397	0.146878
59:	546.25	1.534270	0.749994
60:	570.03	1.244784	0.749394
61:	592.45	11.926810	0.750000
62:	597.95	28.487786	0.068688
63:	603.73	0.532678	0.749265
64:	616.74	6.086593	0.749968
65:	648.77	0.562881	0.749918
66:	660.38	2.288795	0.749905
67:	696.71	0.080648	0.749896
68:	706.31	10.308916	0.749966
69:	711.49	3.576237	0.749996
70:	719.97	6.106574	0.736972
71:	766.09	20.258916	0.749994
72:	777.64	5.286523	0.749988
73:	782.92	8.914130	0.749974
74:	805.10	3.688680	0.160249
75:	828.53	7.094884	0.749994
76:	834.83	20.052494	0.749958
77:	842.86	22.658570	0.749985
78:	845.69	8.012477	0.749957
79:	848.25	29.809531	0.749991
80:	850.57	11.939641	0.749996
81:	855.32	63.527212	0.307757
82:	863.50	0.062858	0.749516
83:	880.99	5.221013	0.749778
84:	889.51	21.338063	0.115575

85:	889.54	8.218646	0.197084
86:	890.74	32.043289	0.749977

The peaks in the experimental rR spectra were assigned to modes in the computation by a combined examination of the calculated Raman intensity, polarization, and mode energy. The character of the mode was assigned by examination of the pictures in **Figures S56-S71**. A tabulation of all assignments to computation is given in **Table S22**.

**CuOEP:**

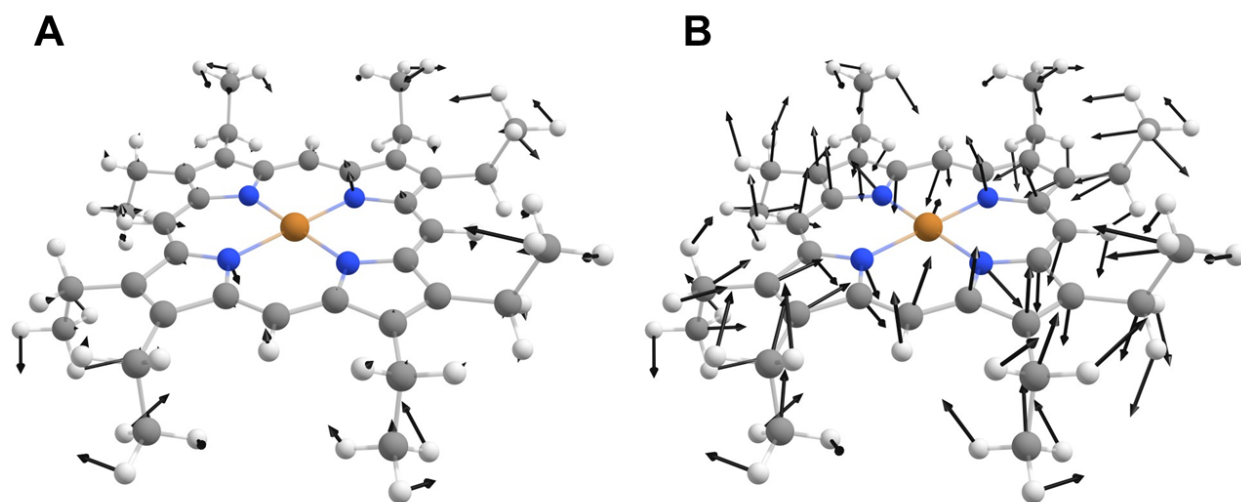


**Figure S56.** Calculated CuOEP vibration at 221.6 cm<sup>-1</sup>. (A) scaled displacement arrows, (B) unscaled displacement arrows.

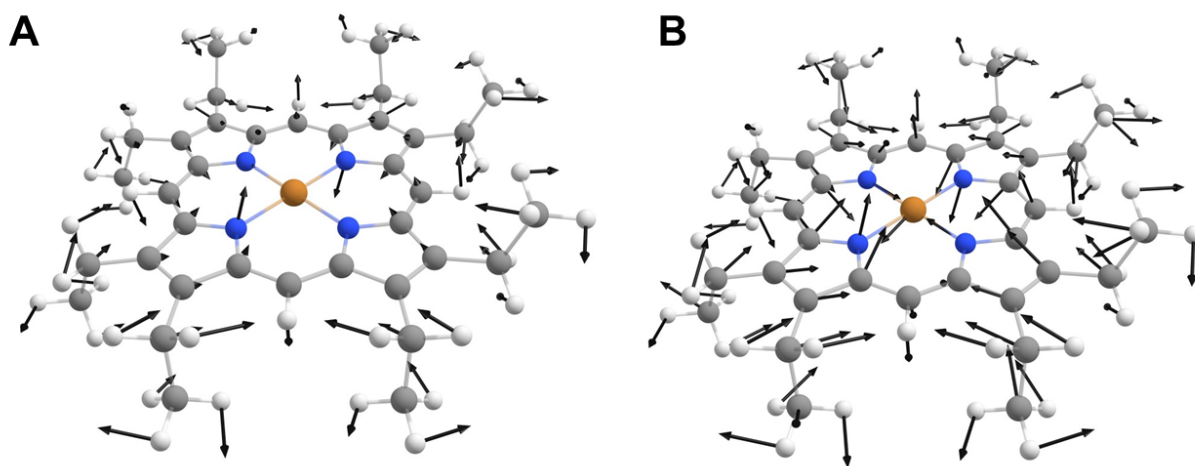


**Figure S57.** Calculated CuOEP vibration at 280.6 cm<sup>-1</sup>, assigned as the ligand symmetric stretch. (A) scaled displacement arrows, (B) unscaled displacement arrows.

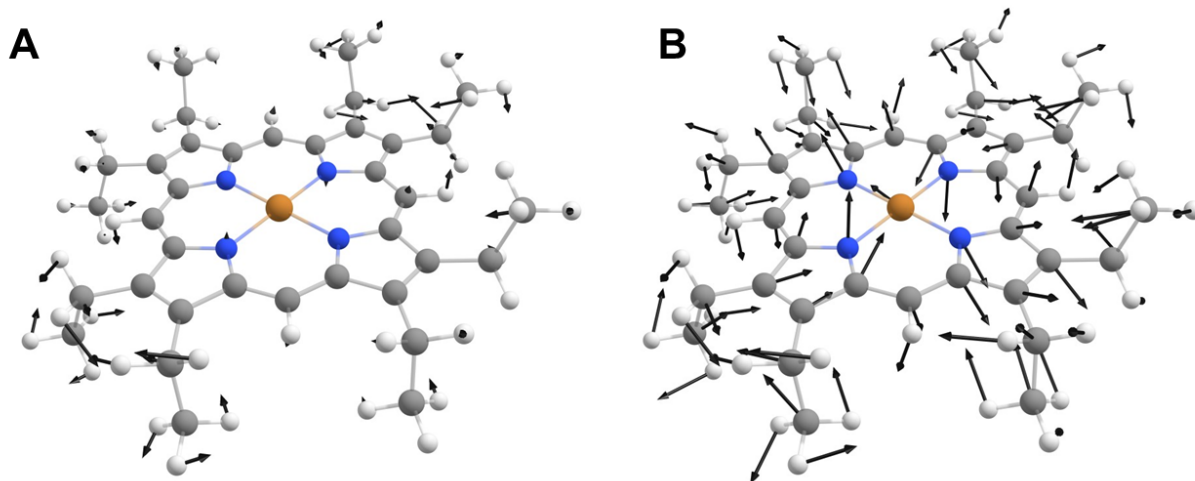


**Figure S58.** Calculated CuOEP vibration at 331.1 cm<sup>-1</sup>. (A) scaled displacement arrows, (B) unscaled displacement arrows.

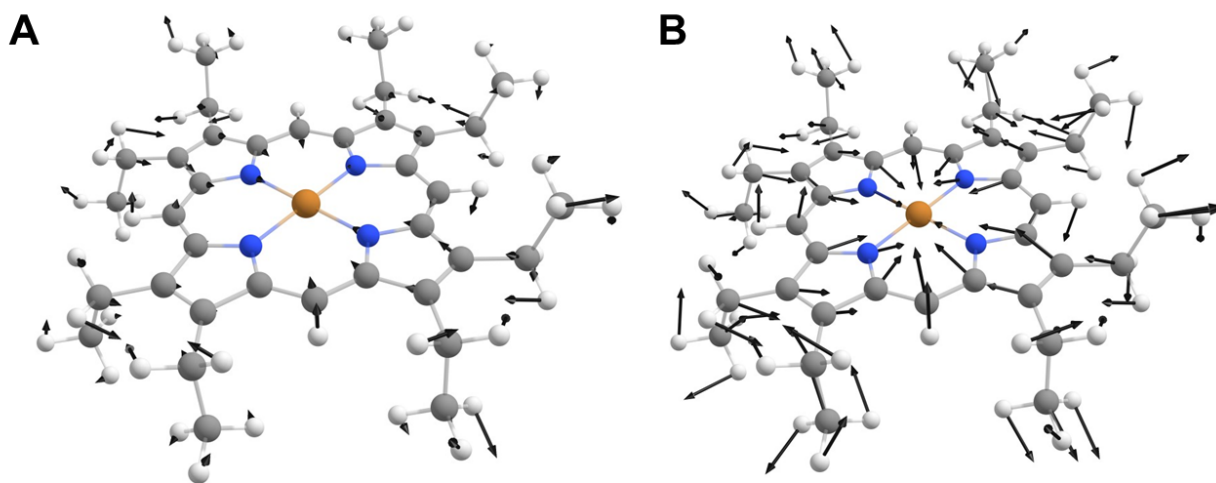


**Figure S59.** Calculated CuOEP vibration at 369.5 cm<sup>-1</sup>. (A) scaled displacement arrows, (B) unscaled displacement arrows.

**CuTPP (H-optimized crystal structure):**

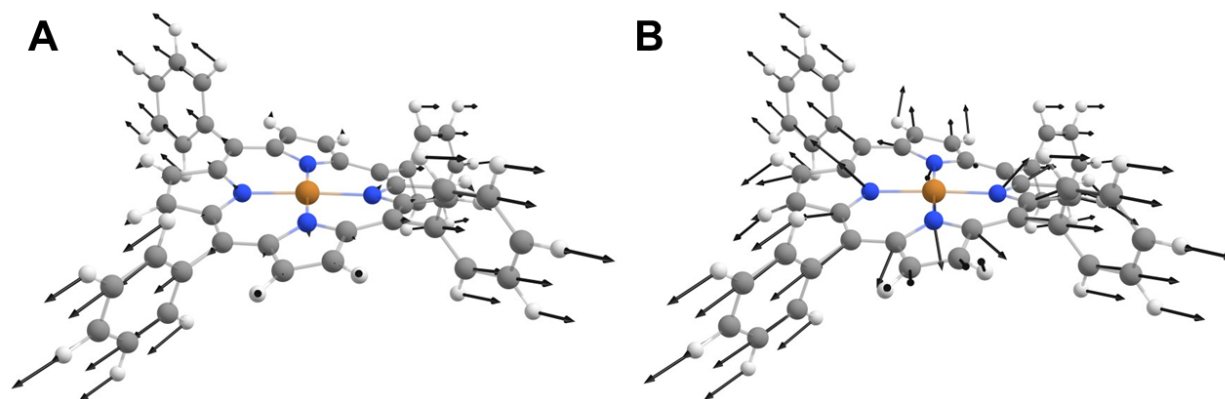


**Figure S60.** Calculated CuTPP vibration (H-optimized crystal structure) at 203.9 cm<sup>-1</sup>, assigned as the ligand symmetric stretch. (A) scaled displacement arrows, (B) unscaled displacement arrows.

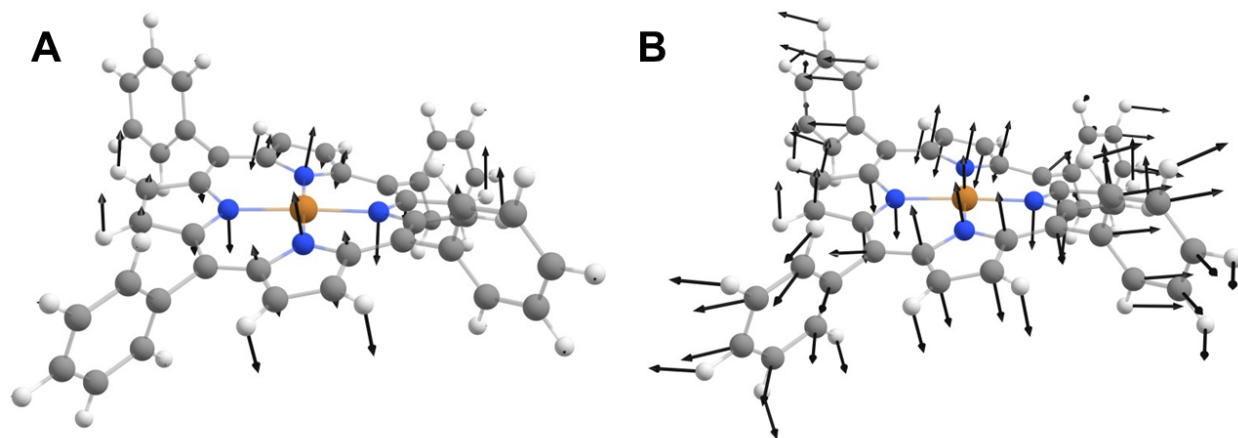


**Figure S61.** Calculated CuTPP vibration (H-optimized crystal structure) at 231.3 cm<sup>-1</sup>. (A) scaled displacement arrows, (B) unscaled displacement arrows.

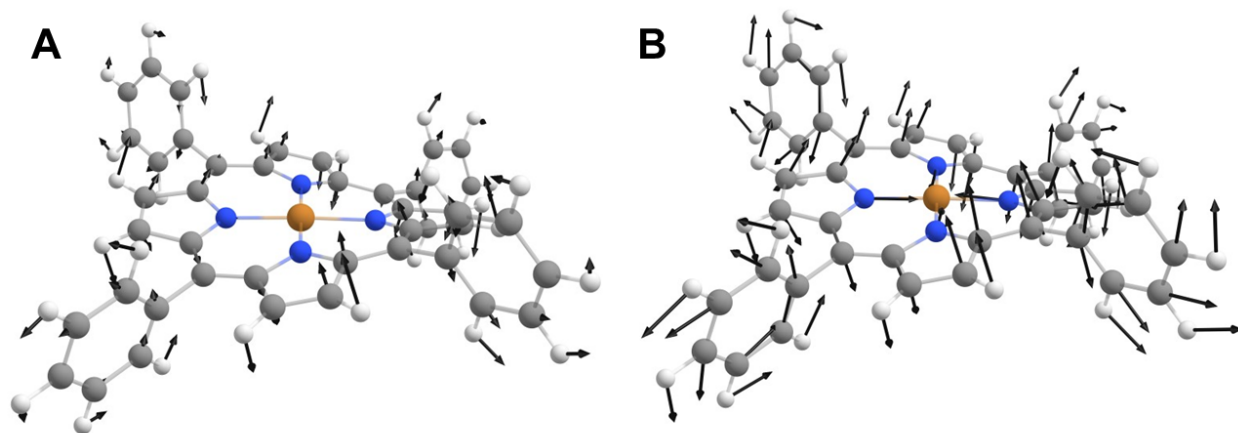


**Figure S62.** Calculated CuTPP vibration (H-optimized crystal structure) at 354.6 cm<sup>-1</sup>. (A) scaled displacement arrows, (B) unscaled displacement arrows.

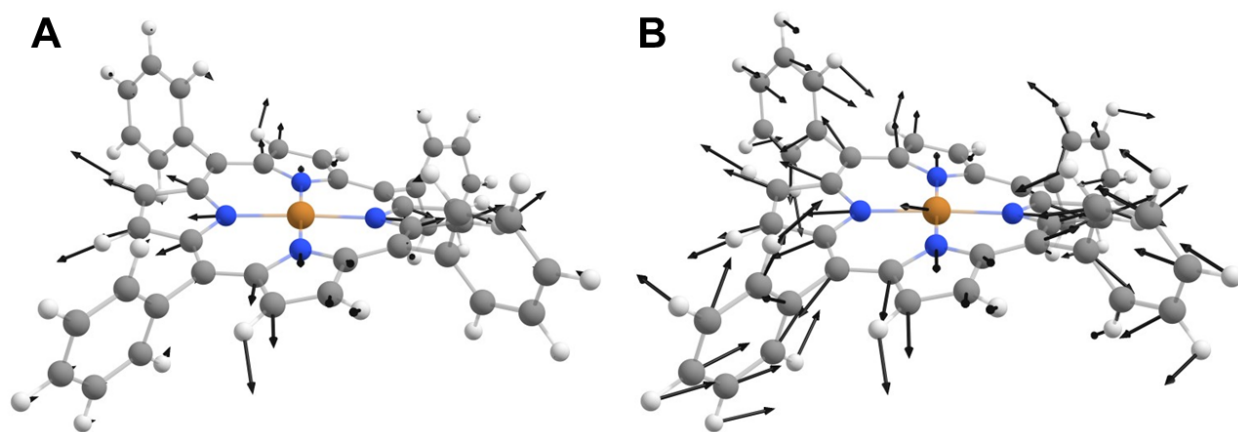


**Figure S63.** Calculated CuTPP vibration (H-optimized crystal structure) at 420.1 cm<sup>-1</sup>. (A) scaled displacement arrows, (B) unscaled displacement arrows.

**CuTPP (fully optimized):**

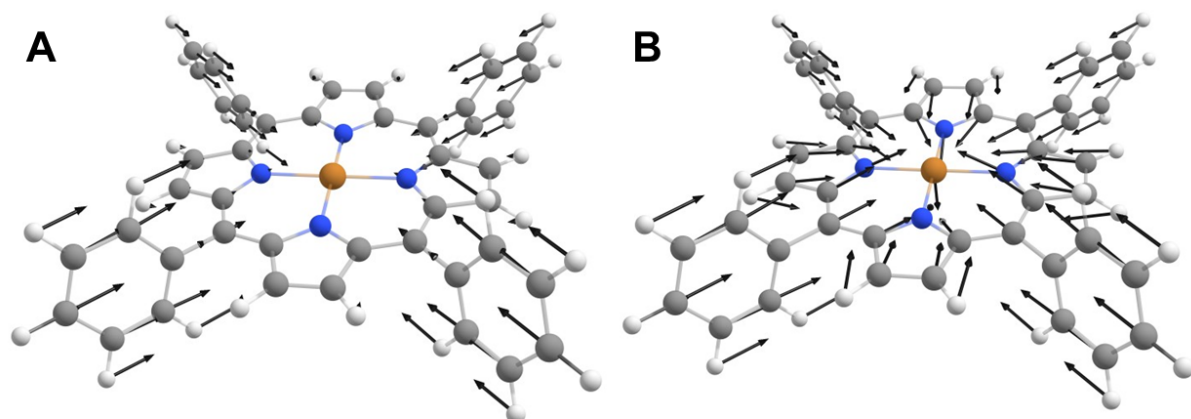


**Figure S64.** Calculated CuTPP vibration (fully optimized geometry) at  $204.5 \text{ cm}^{-1}$ , corresponding to the ligand symmetric stretch. (A) scaled displacement arrows, (B) unscaled displacement arrows.

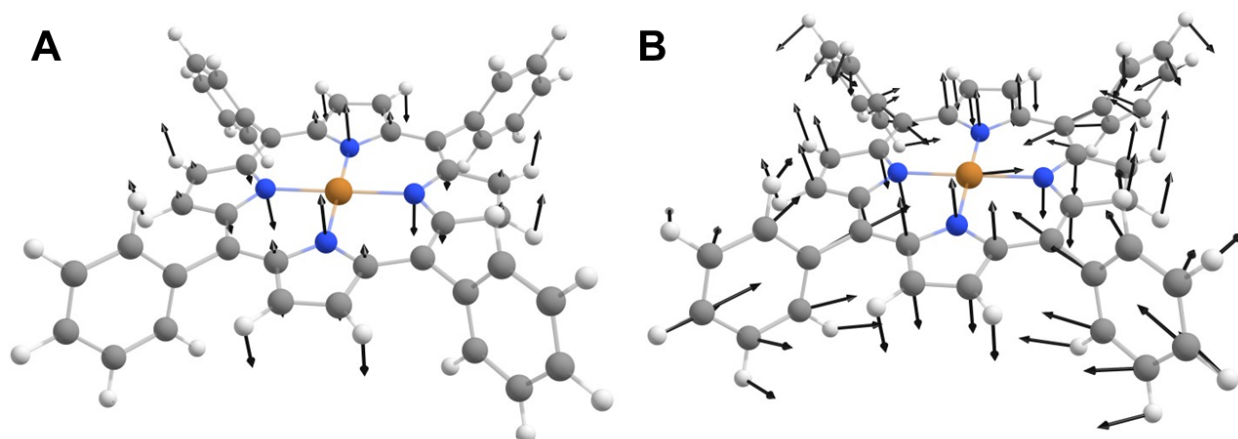


**Figure S65.** Calculated CuTPP vibration (fully optimized geometry) at  $230.0 \text{ cm}^{-1}$ . (A) scaled displacement arrows, (B) unscaled displacement arrows.

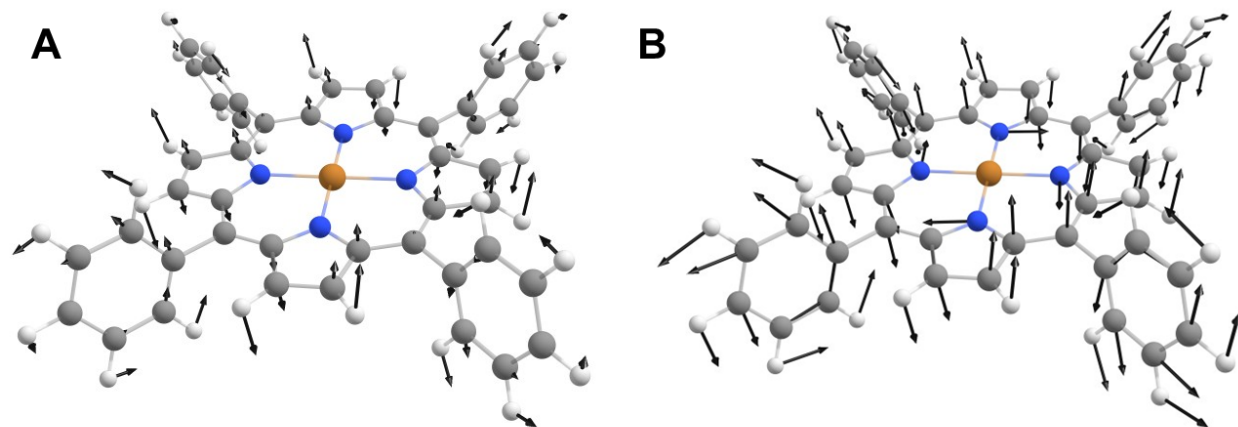


**Figure S66.** Calculated CuTPP vibration (fully optimized geometry) at  $348.7\text{ cm}^{-1}$ . (A) scaled displacement arrows, (B) unscaled displacement arrows.

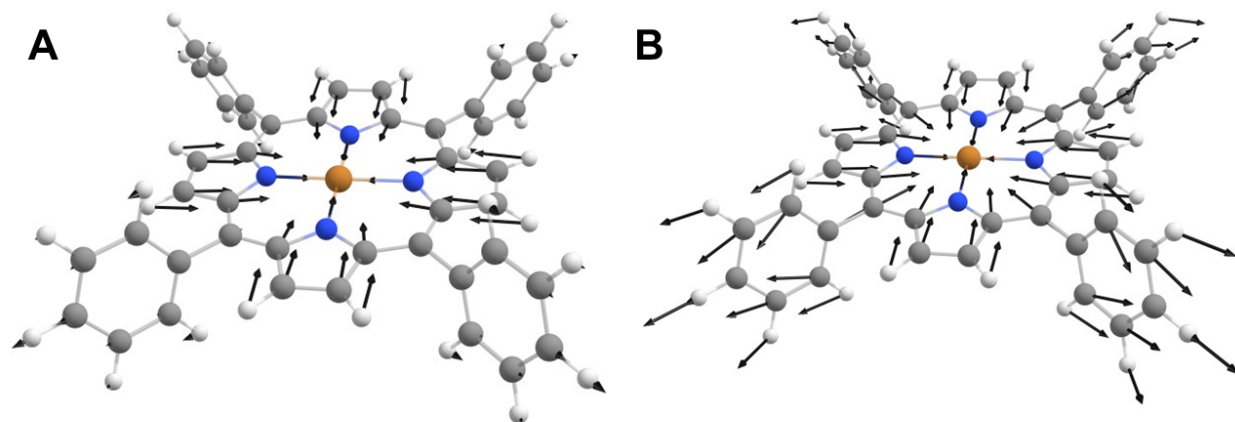


**Figure S67.** Calculated CuTPP vibration (fully optimized geometry) at  $401.4\text{ cm}^{-1}$ . (A) scaled displacement arrows, (B) unscaled displacement arrows.

**CuTiPP:**

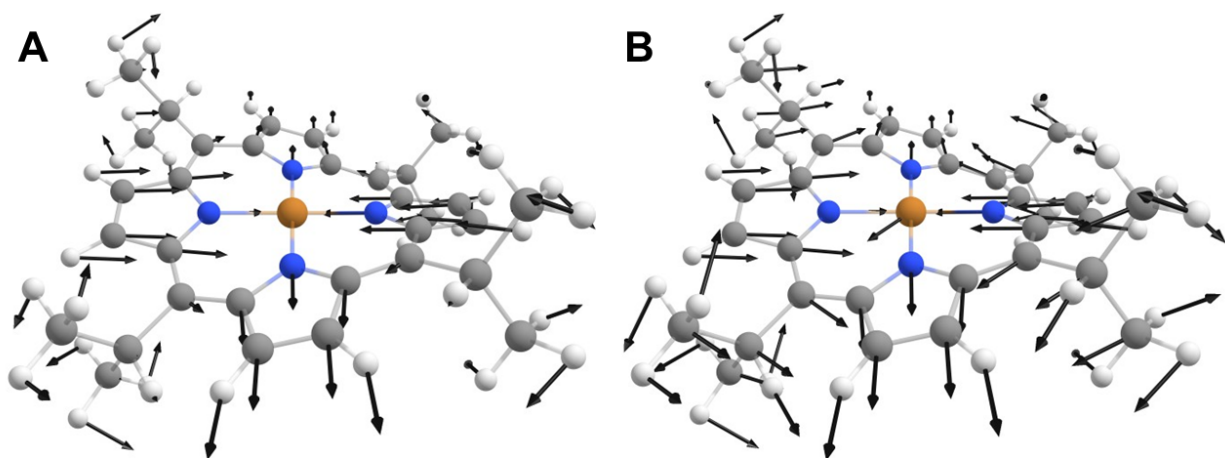


**Figure S68.** Calculated CuTiPP vibration at 225.53 cm<sup>-1</sup>. (A) scaled displacement arrows, (B) unscaled displacement arrows.

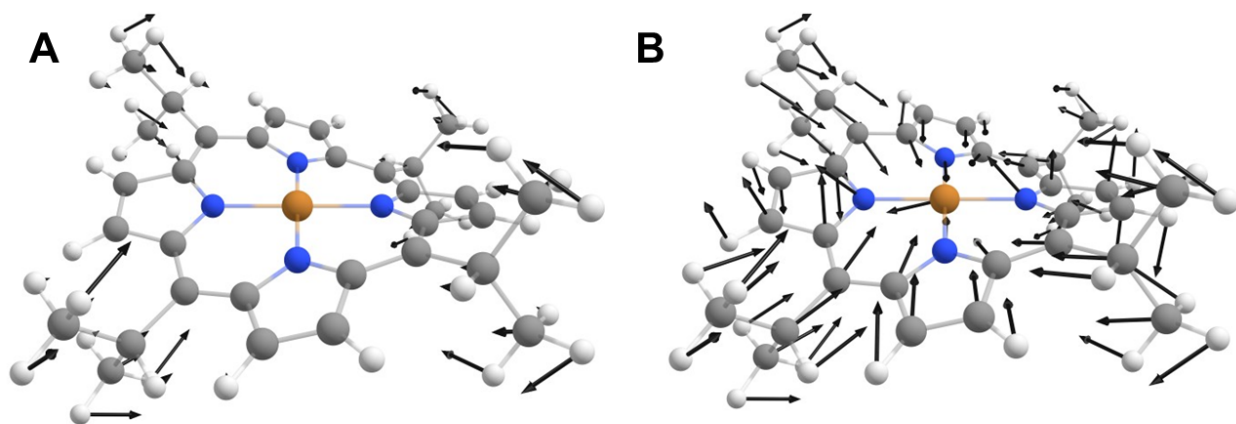


**Figure S69.** Calculated CuTiPP vibration at 243.5 cm<sup>-1</sup>, corresponding to the ligand symmetric stretch. (A) scaled displacement arrows, (B) unscaled displacement arrows.

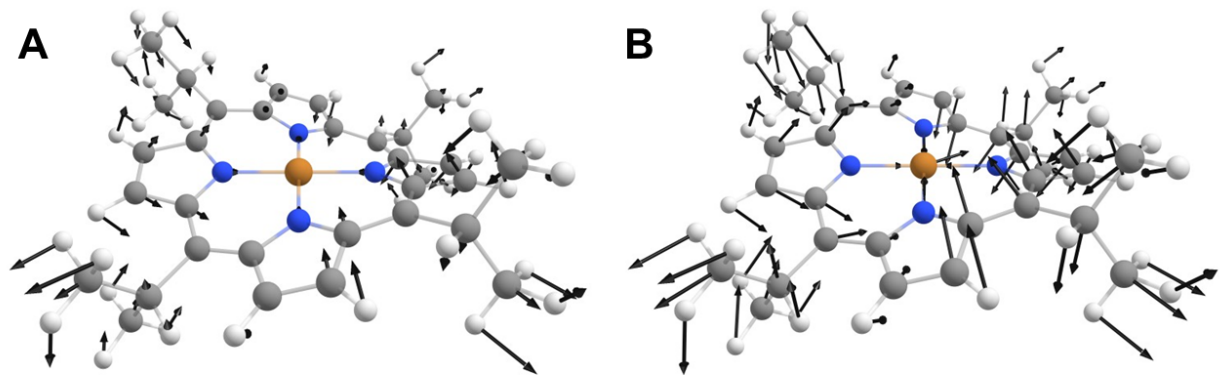


**Figure S70.** Calculated CuTiPP vibration at 369.4 cm<sup>-1</sup>. (A) scaled displacement arrows, (B) unscaled displacement arrows.

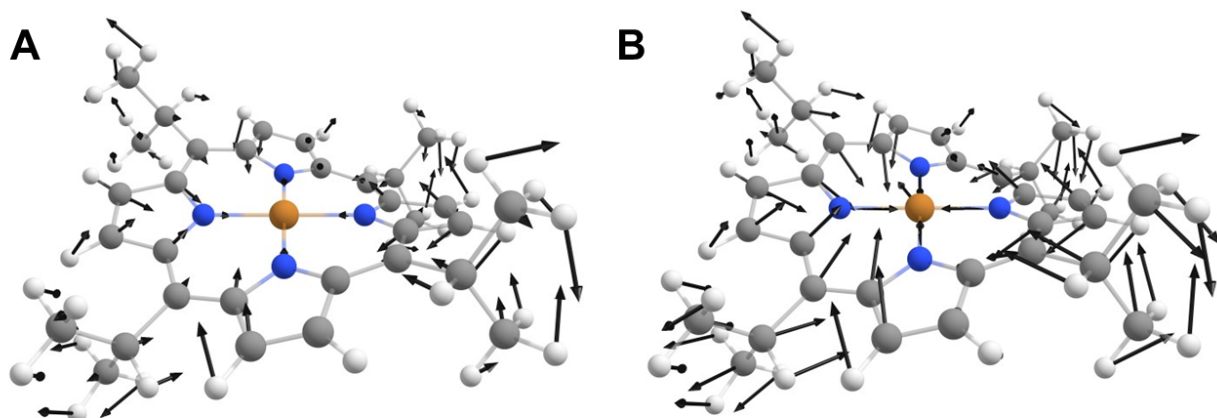


**Figure S71.** Calculated CuTiPP vibration at 399.7 cm<sup>-1</sup>. (A) scaled displacement arrows, (B) unscaled displacement arrows.

**Table S22:** Calculated four main Raman bands below 430 cm<sup>-1</sup> and assignments to experimental rR peaks. \* denotes ligand symmetric stretch (LSS), † denotes mixed metal-ligand gerade mode of variable character for each porphyrin, and ‡ denotes the main metal-ligand bond symmetric stretches.

Sample	Peak 1	Peak 2	Peak 3	Peak 4
<b>CuOEP (calc., opt.)</b>	<b>221.6<sup>†</sup></b>	<b>280.6<sup>*</sup></b>	<b>331.1<sup>‡</sup></b>	<b>369.5<sup>‡</sup></b>
CuOEP (CS <sub>2</sub> )	224	271	343	361
CuOEP (solid)	220	269	351	359
<b>CuTPP (calc., H-opt xtal)</b>	<b>203.9<sup>*</sup></b>	<b>231.3<sup>†</sup></b>	<b>354.6<sup>‡</sup></b>	<b>420.1<sup>‡</sup></b>
<b>CuTPP (calc., opt.)</b>	<b>204.5<sup>*</sup></b>	<b>230.0<sup>†</sup></b>	<b>348.7<sup>‡</sup></b>	<b>401.4<sup>‡</sup></b>
CuTPP (C <sub>6</sub> H <sub>6</sub> )	203	233	337	392
CuTPP (solid)	204	230	337 (325 sh.)	393
<b>CuTiPP (calc., opt.)</b>	<b>225.5<sup>†</sup></b>	<b>243.5<sup>*</sup></b>	<b>369.4<sup>‡</sup></b>	<b>399.7<sup>‡</sup></b>
CuTiPP (C <sub>6</sub> H <sub>6</sub> )	227	244	357	390
CuTiPP (solid)	224	245	359	383

#### D. Analysis of Excited State Transition Energies

The calculated ligand field excited state energies for unsubstituted CuP in various ruffled conformations are summarized in **Table S23**. Ruffled geometries of CuP were generated by performing a frequency calculation on CuP and iteratively displacing the coordinates along the ruffling mode. The excited state energies of the substituted copper porphyrins examined experimentally in this study are found in **Table S24**. The principal g-values for the ideal ruffled CuP and real copper porphyrins are summarized in **Tables S25-S26**.

**Table S23.** Calculated ligand field transition energies ( $\text{cm}^{-1}$ ) for unsubstituted CuP as a function of degree of ruffling.

$B_{1u}$	$xy \rightarrow x^2-y^2$	$xz \rightarrow x^2-y^2$	$yz \rightarrow x^2-y^2$	$z^2 \rightarrow x^2-y^2$
0.0	19371	18009	17996	17821
0.3	19341	18017	18005	17818
0.6	19295	18021	18033	17843
0.9	19228	18047	18059	17885
1.2	19150	18082	18094	17941
1.5	19068	18124	18137	18011
1.8	18987	18172	18185	18091
2.1	18908	18219	18234	18177
2.4	18831	18271	18294	18259

**Table S24.** Calculated ligand field transition energies ( $\text{cm}^{-1}$ ) for substituted CuP compounds in this study.

Porphyrin	$B_{1u}$	$xy \rightarrow x^2-y^2$	$xz \rightarrow x^2-y^2$	$yz \rightarrow x^2-y^2$	$z^2 \rightarrow x^2-y^2$
CuOEP	0.00	20759	19438	19323	19383
CuTPP	1.12	21311	20114	20124	20059
CuTiPP	1.35	21559	20499	20544	20475

**Table S25.** Calculated g values for unsubstituted CuP as a function of degree of ruffling.

$B_{1u}$	$g_x$	$g_y$	$g_z$
0.00	2.06117	2.06121	2.19586
0.03	2.06123	2.06127	2.19607
0.06	2.06123	2.06127	2.19607
0.15	2.06122	2.06126	2.19607
0.31	2.06119	2.06123	2.19607
0.46	2.06114	2.06118	2.19607
0.61	2.06107	2.06111	2.19606
0.76	2.06098	2.06103	2.19606
0.92	2.06088	2.06092	2.19606
1.22	2.06063	2.06067	2.19606
1.53	2.06032	2.06037	2.19609

**Table S26.** Calculated g values for substituted CuP compounds in this study.

Porphyrin	$B_{1u}$	$g_x$	$g_y$	$g_z$
CuOEP	0.00	2.05527	2.05527	2.17116
CuTPP	1.12	2.05267	2.05266	2.16468
CuTiPP	1.35	2.05116	2.05185	2.16139

### E. Excited State Transition Energies and Principal g values of Idealized CuP

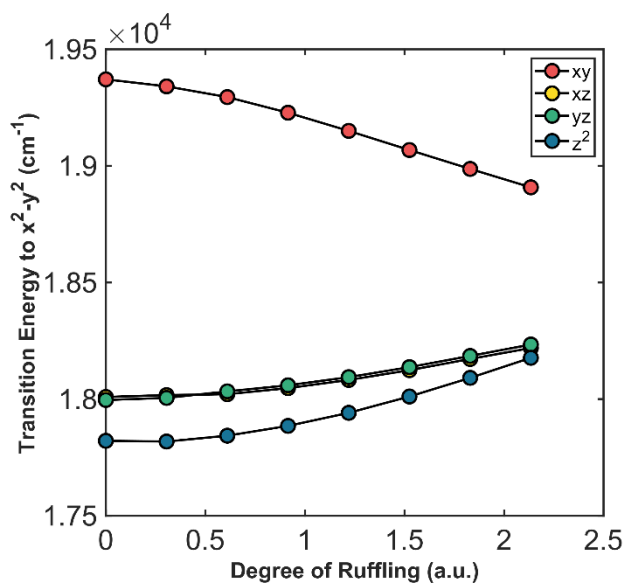


**Figure S72.** Excited state transition energies calculated for an idealized CuP with varying degrees of ruffling.

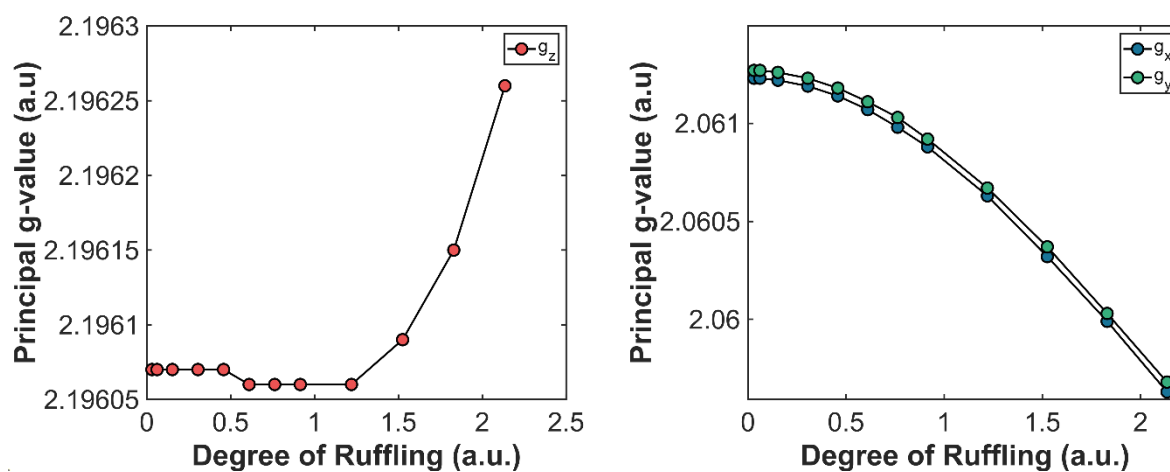


**Figure S73.** Principal g values calculated for an idealized CuP with varying degrees of ruffling.

## 4. Supplemental Discussion

### A. Quantification of Macrocycle Distortion

We utilized the Normal-coordinate Structural Decomposition (NSD) program developed by Kingsbury and Senge based on the original program written by Shelnut. <sup>20-23</sup> This program uses a least-squares matrix reduction algorithm on the position of atoms in the porphyrin macrocycle, with all rotational and translational elements removed, to quantify the degree of distortion along the symmetry-banded normal coordinate modes. Based on the x, y coordinates and z coordinates of the atoms, a matrix can be generated and fit to a linear combination of the optimized vibrational modes:  $a_{1g}$ ,  $a_{2u}$ ,  $b_{1u}$ ,  $b_{2u}$ ,  $e_g$ . The resulting matrix represents the calculated distortion of a crystal structure with respect to an idealized porphyrin macrocycle along these idealized normal coordinates. From this, in-plane and out-of-plane distortion can be quantified and assigned to these symmetries.

Thus, we can use the NSD program and crystal structures of our porphyrins (CuOEP,<sup>9</sup> CuTPP,<sup>7</sup> CuTiPP,<sup>2</sup> ZnOEP,<sup>10</sup> NiTPP,<sup>8</sup> and NiTiPP<sup>11</sup>) to decompose the total deviation from the idealized macrocycle into contributions from each of the idealized normal-coordinates, namely  $a_{2u}$ ,  $b_{1u}$ ,  $b_{2u}$ ,  $e_g$ . For this study, we focused on copper porphyrins possessing nearly pure  $b_{1u}$  (*ruffled*) distortions. Note, in the NSD report for each copper porphyrin, any composite distortion value at or below 0.10 is deemed undistorted.<sup>20</sup> The value of distortion along each idealized normal-coordinate is taken from the bottom composite (comp.) line in the NSD report.

**Table S27.** Contributions of each ideal normal mode to overall distortion of each copper porphyrin.

Porphyrin	$\Delta_{oop}$	$B_{2u}$	$B_{1u}$	$A_{2u}$	$E_g(x)$	$E_g(y)$	$A_{1u}$
CuOEP	0.12	0.00	0.00	0.00	0.11	0.05	0.00
ZnOEP	0.17	0.00	0.00	0.00	0.16	0.06	0.00
CuTPP	1.14	0.21	1.12	0.00	0.00	0.00	0.00
NiTPP	1.29	0.27	1.27	0.00	0.00	0.00	0.00
CuTiPP	1.35	0.00	1.35	0.00	0.00	0.11	0.03
NiTiPP	2.08	0.46	2.03	0.03	0.09	0.10	0.03

### B. Implications of CuTiPP Crystal Phases for Distortion Quantification

As indicated in **Supporting Information Section 2B-2C**, CuTiPP as prepared was found to crystallize in two distinct phases; an unsolvated structure with space group  $Fdd2$  and a dichloromethane solvate structure with space group  $I4_1$ . Both structures display ruffled CuTiPP molecules, but the degree of ruffling quantified by NSD analysis is different (**Table S28**). Note that the  $I4_1$  structure contains two inequivalent CuTiPP molecules in the asymmetric unit; we

therefore applied the NSD analysis separately to each CuTiPP site. The  $I4_1$  structure has less ruffled CuTiPP molecules (1.09 average) than the  $Fdd2$  structure (1.35).

**Table S28:** Normal coordinate structure decomposition analysis of CuTiPP crystal phases.

Distortion mode	Ruffling ( $b_{1u}$ )	Saddling ( $b_{2u}$ )	Doming ( $a_{2u}$ )	Waving ( $e_g(x)$ )	Waving ( $e_g(y)$ )
CuTiPP ( $Fdd2$ )	<b>1.35</b>	0.00	0.00	0.00	0.11
CuTiPP ( $I4_1$ site 1)	<b>1.10</b>	0.20	0.07	0.08	0.17
CuTiPP ( $I4_1$ site 2)	<b>1.08</b>	0.19	0.06	0.20	0.13

These observations raise the question of whether CuTiPP is more or less ruffled than CuTPP, which displays an NSD ruffling of 1.14, in between the two CuTiPP crystal phases. We argue that under the conditions probed by EPR spectroscopy, CuTiPP is more ruffled than CuTPP. (1) The  $I4_1$  CuTiPP structure contains a solvent molecule, but the NiTiPP structure does not. PXRD reveals that the co-crystallized EPR sample adopts the bulk phase of the NiTiPP (**Supporting Information Section 2B**). It is therefore unlikely that the solvated  $I4_1$  CuTiPP structure is relevant to the CuTiPP molecular geometry in the EPR sample, so the unsolvated  $Fdd2$  CuTiPP structure should be analyzed instead. (2) The NiTiPP diamagnetic matrix is more ruffled (2.08) than the CuTiPP paramagnetic dopant (1.35,  $Fdd2$  structure). In the cocrystallization, it is likely that the CuTiPP molecule adopts a geometry somewhere in-between the 1.35 and 2.08 ruffling parameters, so co-crystallization tends to increase the degree of CuTiPP ruffling. By contrast, CuTPP and NiTPP have more similar degrees of ruffling (1.14 and 1.29, respectively), both of which are lower than the CuTiPP  $Fdd2$  structure ruffling. Therefore, CuTiPP is more ruffled than CuTPP in the cocrystallized samples used for pulse EPR analysis of spin relaxation.

### C. Transformation of Vibrational Mode Symmetries from $D_{4h}$ to $D_{2d}$

**Table S29.** Character table for the  $D_{4h}$  point group.

$D_{4h}$	E	$2C_4(z)$	$C_2$	$2C'_2$	$2C''_2$	i	$2S_4$	$\sigma_h$	$2\sigma_v$	$2\sigma_d$
$A_{1g}$	+1	+1	+1	+1	+1	+1	+1	+1	+1	+1
$A_{2g}$	+1	+1	+1	-1	-1	+1	+1	+1	-1	-1
$B_{1g}$	+1	-1	+1	+1	-1	+1	-1	+1	+1	-1
$B_{2g}$	+1	-1	+1	-1	+1	+1	-1	+1	-1	+1
$E_g$	+2	0	-2	0	0	+2	0	-2	0	0
$A_{1u}$	+1	+1	+1	+1	+1	-1	-1	-1	-1	-1
$A_{2u}$	+1	+1	+1	-1	-1	-1	-1	-1	+1	+1
$B_{1u}$	+1	-1	+1	+1	-1	-1	+1	-1	-1	+1
$B_{2u}$	+1	-1	+1	-1	+1	-1	+1	-1	+1	-1
$E_u$	+2	0	-2	0	0	-2	0	+2	0	0

$D_{2d}$	E	$2S_4$	$C_2(z)$	$2C'_2$	$2\sigma_d$
$A_1$	+1	+1	+1	+1	+1
$A_2$	+1	+1	+1	-1	-1
$B_1$	+1	-1	+1	+1	-1
$B_2$	+1	-1	+1	-1	+1
E	+2	0	-2	0	0

A reduction of symmetry from  $D_{4h}$  to  $D_{2d}$  which physically arises when we structurally ruffle a copper porphyrin from the idealized, planar geometry. Here, we show that, once a porphyrin is ruffled and belongs to the  $D_{2d}$  point group, the ruffling vibrational mode (transforming as  $B_{1u}$  in the  $D_{4h}$  point group) now transforms as the totally symmetric  $A_1$  irreducible representation. The consequences of this lies in the activation of the low energy ruffling vibrational modes to couple to electronic spins via spin-phonon coupling.<sup>24</sup>

Consider the  $D_{4h}$  character table whose  $B_{1u}$  irreducible representation is highlighted in red. Upon lowering in symmetry, several symmetry operations are not present in the  $D_{2d}$  character table. However, of the symmetry operations that are preserved, we reduce the  $D_{4h}$  point group into the following:

$D_{4h}$	E	$2C_4(z)$	$C_2$	$2C'_2$	$2C''_2$	i	$2S_4$	$\sigma_h$	$2\sigma_v$	$2_d$
$A_{1g}$	+1	+1	+1	+1	+1	+1	+1	+1	+1	+1
$A_{2g}$	+1	+1	+1	-1	-1	+1	+1	+1	-1	-1
$B_{1g}$	+1	-1	+1	+1	-1	+1	-1	+1	+1	-1
$B_{2g}$	+1	-1	+1	-1	+1	+1	-1	+1	-1	+1
$E_g$	+2	0	-2	0	0	+2	0	-2	0	0
$A_{1u}$	+1	+1	+1	+1	+1	-1	-1	-1	-1	-1
$A_{2u}$	+1	+1	+1	-1	-1	-1	-1	-1	+1	+1
$B_{1u}$	+1	-1	+1	+1	-1	-1	+1	-1	-1	+1
$B_{2u}$	+1	-1	+1	-1	+1	-1	+1	-1	+1	-1
$E_u$	+2	0	-2	0	0	-2	0	+2	0	0



$D_{4h}$ (reduced)	E	$C_2$	$2C'_2$	$2S_4$	$2\sigma_d$
--------------------	---	-------	---------	--------	-------------

$A_{1g}$	+1	+1	+1	+1	+1
$A_{2g}$	+1	+1	-1	+1	-1
$B_{1g}$	+1	+1	+1	-1	-1
$B_{2g}$	+1	+1	-1	-1	+1
$E_g$	+2	-2	0	0	0
$A_{1u}$	+1	+1	+1	-1	-1
$A_{2u}$	+1	+1	-1	-1	+1
$B_{1u}$	+1	+1	+1	+1	+1
$B_{2u}$	+1	+1	-1	+1	-1
$E_u$	+2	-2	0	0	0

In this reduced character table, the representation originating from the  $B_{1u}$  irreducible representation is exactly that of the  $A_1$  irreducible representation in the  $D_{2d}$  character table. Thus, upon reducing the symmetry from  $D_{4h}$  to  $D_{2d}$ , the vibrational modes transforming as  $B_{1u}$  in  $D_{4h}$  now transform as  $A_1$  in  $D_{2d}$ .

## 5. References

- (1) Lindsey, J. S.; Schreiman, I. C.; Hsu, H. C.; Kearney, P. C.; Marguerettaz, A. M. Rothmund and Adler-Longo Reactions Revisited: Synthesis of Tetraphenylporphyrins under Equilibrium Conditions. *J. Org. Chem.* **1987**, *52* (5), 827–836. <https://doi.org/10.1021/jo00381a022>.
- (2) Senge, M. O.; Bischoff, I.; Nelson, N. Y.; Smith, K. M. Synthesis, Reactivity and Structural Chemistry of 5,10,15,20-Tetraalkylporphyrins. *J. Porphyrins Phthalocyanines* **1999**, *03* (02), 99–116. [https://doi.org/10.1002/\(SICI\)1099-1409\(199902\)3:2<99::AID-JPP109>3.0.CO;2-6](https://doi.org/10.1002/(SICI)1099-1409(199902)3:2<99::AID-JPP109>3.0.CO;2-6).
- (3) K.M.Smith(Ed.), *Porphyrins and Metalloporphyrins*, Elsevier, Amsterdam(1975).
- (4) Toby, B. H. EXPGUI, a Graphical User Interface for GSAS. *J Appl Cryst* **2001**, *34* (2), 210–213. <https://doi.org/10.1107/S0021889801002242>.
- (5) Toby, B. H.; Von Dreele, R. B. GSAS-II: The Genesis of a Modern Open-Source All Purpose Crystallography Software Package. *J Appl Cryst* **2013**, *46* (2), 544–549. <https://doi.org/10.1107/S0021889813003531>.
- (6) Momma, K.; Izumi, F. VESTA 3 for Three-Dimensional Visualization of Crystal, Volumetric and Morphology Data. *J Appl Cryst* **2011**, *44* (6), 1272–1276. <https://doi.org/10.1107/S0021889811038970>.
- (7) Fleischer, E. B.; Miller, C. K.; Webb, L. E. Crystal and Molecular Structures of Some Metal Tetraphenylporphines. *J. Am. Chem. Soc.* **1964**, *86* (12), 2342–2347. <https://doi.org/10.1021/ja01066a009>.
- (8) Maclean, A. L.; Foran, G. J.; Kennedy, B. J.; Turner, P.; Hambley, T. W. Structural Characterization of Nickel(II) Tetraphenylporphyrin. *Aust. J. Chem.* **1996**, *49* (12), 1273–1278. <https://doi.org/10.1071/ch9961273>.

- (9) Pak, R.; Scheidt, W. R. Structure of (2,3,7,8,12,13,17,18-Octaethylporphinato)Copper(II). *Acta Cryst C* **1991**, *47* (2), 431–433. <https://doi.org/10.1107/S0108270190008010>.
- (10) Ozarowski, A.; Lee, H. M.; Balch, A. L. Crystal Environments Probed by EPR Spectroscopy. Variations in the EPR Spectra of CoII(Octaethylporphyrin) Doped in Crystalline Diamagnetic Hosts and a Reassessment of the Electronic Structure of Four-Coordinate Cobalt(II). *J. Am. Chem. Soc.* **2003**, *125* (41), 12606–12614. <https://doi.org/10.1021/ja030221f>.
- (11) Ema, T.; Senge, M. O.; Nelson, N. Y.; Ogoshi, H.; Smith, K. M. 5,10,15,20-Tetra-Tert-Butylporphyrin and Its Remarkable Reactivity in the 5- and 15-Positions. *Angewandte Chemie International Edition in English* **1994**, *33* (18), 1879–1881. <https://doi.org/10.1002/anie.199418791>.
- (12) Sheldrick, G. M. Phase Annealing in SHELX-90: Direct Methods for Larger Structures. *Acta Cryst A* **1990**, *46* (6), 467–473. <https://doi.org/10.1107/S0108767390000277>.
- (13) Sheldrick, G. M. Crystal Structure Refinement with SHELXL. *Acta Cryst C* **2015**, *71* (1), 3–8. <https://doi.org/10.1107/S2053229614024218>.
- (14) Müller, P. Practical Suggestions for Better Crystal Structures. *Crystallography Reviews* **2009**, *15* (1), 57–83. <https://doi.org/10.1080/08893110802547240>.
- (15) Stoll, S.; Schweiger, A. EasySpin, a Comprehensive Software Package for Spectral Simulation and Analysis in EPR. *Journal of Magnetic Resonance* **2006**, *178* (1), 42–55. <https://doi.org/10.1016/j.jmr.2005.08.013>.
- (16) Neese, F. Software Update: The ORCA Program System—Version 5.0. *WIREs Computational Molecular Science* **2022**, *12* (5), e1606. <https://doi.org/10.1002/wcms.1606>.
- (17) Szilagy, R. K.; Metz, M.; Solomon, E. I. Spectroscopic Calibration of Modern Density Functional Methods Using [CuCl<sub>4</sub>]<sup>2-</sup>. *J. Phys. Chem. A* **2002**, *106* (12), 2994–3007. <https://doi.org/10.1021/jp014121c>.
- (18) Mirzoyan, R.; Hadt, R. G. The Dynamic Ligand Field of a Molecular Qubit: Decoherence through Spin–Phonon Coupling. *Phys. Chem. Chem. Phys.* **2020**, *22* (20), 11249–11265. <https://doi.org/10.1039/D0CP00852D>.
- (19) Kazmierczak, N. P.; Mirzoyan, R.; Hadt, R. G. The Impact of Ligand Field Symmetry on Molecular Qubit Coherence. *J. Am. Chem. Soc.* **2021**, *143* (42), 17305–17315. <https://doi.org/10.1021/jacs.1c04605>.
- (20) Kingsbury, C. J.; Senge, M. O. The Shape of Porphyrins. *Coordination Chemistry Reviews* **2021**, *431*, 213760. <https://doi.org/10.1016/j.ccr.2020.213760>.
- (21) Shelnut, J. A. Normal-Coordinate Structural Decomposition and the Vibronic Spectra of Porphyrins. *Journal of Porphyrins and Phthalocyanines* **2012**. <https://doi.org/10.1002/jpp.320>.
- (22) *Conservation of the Conformation of the Porphyrin Macrocycle in Hemoproteins | Elsevier Enhanced Reader*. [https://doi.org/10.1016/S0006-3495\(98\)74000-7](https://doi.org/10.1016/S0006-3495(98)74000-7).
- (23) Jentzen, W.; Song, X.-Z.; Shelnut, J. A. Structural Characterization of Synthetic and Protein-Bound Porphyrins in Terms of the Lowest-Frequency Normal Coordinates of the Macrocycle. *J. Phys. Chem. B* **1997**, *101* (9), 1684–1699. <https://doi.org/10.1021/jp963142h>.
- (24) Mirzoyan, R.; Kazmierczak, N. P.; Hadt, R. G. Deconvolving Contributions to Decoherence in Molecular Electron Spin Qubits: A Dynamic Ligand Field Approach. *Chemistry – A European Journal* **2021**, *27* (37), 9482–9494. <https://doi.org/10.1002/chem.202100845>.